POINT CONTACT SPECTROSCOPY STUDIES OF THE IRON BASED SUPERCONDUCTORS

BY

HAMOOD ZAFIR ARHAM

DISSERTATION

Submitted in partial fulfillment of the requirements
for the degree of Doctor of Philosophy in Physics
in the Graduate College of the
University of Illinois at Urbana-Champaign, 2014

Urbana, Illinois

Doctoral Committee:

Associate Professor Nadya Mason, Chair
Professor Laura H. Greene, Director of Research
Associate Professor Karin A. Dahmen
Associate Professor Brian L. DeMarco

ABSTRACT

Point contact spectroscopy (PCS) is used to probe both the normal and superconducting phases of the iron based superconductors. It is shown that apart from probing superconductors by Andreev reflection, PCS is also a useful technique to study exotic electron matter in correlated materials. The point contact junctions are made by two separate techniques: needle-anvil PCS and soft PCS.

dI/dV measured in the superconducting phase is sensitive to the magnitude and symmetry of the superconducting order parameter. Andreev reflection spectra for the 122 and 111 families of the iron based superconductors is presented. The 122 crystals probed include electron doped $Ba(Fe_{1-x}Co_x)_2As_2$ $(x = 0.05, 0.055, 0.07, 0.08)$, hole doped $Ba_{0.8}K_{0.2}Fe_2As_2$, and isoelectronic doped $BaFe_2(As_{1-x}P_x)_2$ $(x = 0.24, 0.43)$. The 111 crystals studied are electron doped $NaFe_{1-x}Co_xAs$ $(x = 0.02, 0.06)$. The Andreev spectra show clear features corresponding to multiple, nodeless superconducting gaps. The dI/dV curves are fit to the independent two band BTK model assuming isotropic s-wave order parameters.

The normal state spectra of certain iron based superconductors shows a conductance enhancement around zero bias above the structural transition temperature, T_S. Theoretical analysis showing that this enhancement is likely a consequence of orbital fluctuations is discussed. The nonsuperconducting compounds probed are $AEFe_2As_2$ $(AE = Ca, Sr, Ba)$ and $Fe_{1+y}Te$.

For AE = Sr, Ba orbital fluctuations are detected above T_S while for AE = Ca these fluctuations start below T_S. Co doping preserves the orbital fluctuations while K doping suppresses it. The fluctuations are only seen at those dopings and temperatures where for detwinned crystals, an in-plane resistive anisotropy is known to exist. The normal state spectra thus provides evidence that PCS is sensitive to orbital fluctuations in the iron based superconductors. A thorough analysis of $Ba(Fe_{1-x}Co_x)_2As_2$ is performed and a new region on the phase diagram is defined where PCS picks up orbital fluctuations.

Diagnostics performed to ensure the quality of the PCS junctions are discussed in detail. Preliminary data for dI/dV under applied magnetic field and compressive stress is also presented.

To my fellow graduate students, because no road is long with good company.

ACKNOWLEDGMENTS

First of all, I would like to thank my family, Ammi, Abu, Muhammad and Ahmad. Their unwavering support and belief in me as I have charted out my own path has been priceless.

A very special thanks to Dr. Abdullah Sadiq and the staff of the National Physics Talent Contest in Pakistan. They introduced me to the wonders of Physics and set me on the path of research.

I am indebted to my undergraduate research advisor, Prof. Norman Birge for patiently showing me how actual research in a Physics lab is carried out.

I would like to thank my advisor, Prof. Laura Greene, for her enthusiasm, support, end of semester parties, and conference trips. My time in graduate school would have been much duller had I joined a different research group.

I would like to acknowledge Prof. Wan Kyu Park and Dr. Xin Lu for teaching me the ropes of the lab when I first started my research.

Grad school would have been much harder had Cassandra Hunt not been around to help me with MATLAB coding, fitting data, and critiquing my research write-ups. I am forever grateful for her help.

For me, the best aspect of the Illinois Physics program has been the fellow graduate students. I would especially like to acknowledge Cassi, Anusha, Chris, Maks, Adam, Yun, Yewon, Cory, and Braden. I will forever treasure the time that we have spent together.

I want to also acknowledge the support and guidance of the MRL research staff, especially the machine shop guys, Jim and Ernie.

A special thanks to Prof. Philip Phillips and Dr. Weicheng Lee. Without their theoretical work, my thesis would be incomplete.

Finally, I want to thank the most important people on my project − the crystal growers, without whom none of this work could have happened: Dr. Genda Gu, Prof. Paul Canfield, Prof. Suchitra Sebestian, Prof. Duck Young Chung, and Dr. Daniel Bugaris.

This work is supported as part of the Center for Emergent Superconductivity, an Energy Frontier Research Center funded by the US Department of Energy, Office of Science, Office of Basic Energy Sciences under Award No. DE-AC0298CH1088.

TABLE OF CONTENTS

LIST OF TABLES

LIST OF FIGURES

CHAPTER 1

INTRODUCTION

1.1 Discovery of Superconductivity

A superconductor is defined by two fundamental properties that develop as it is cooled below a critical temperature, T_c. The first one is zero resistance to current flow and the second one is perfect diamagnetism.

The zero resistance state was discovered by Heike Kamerlingh Onnes in 1911 when he observed the resistance of mercury suddenly dropping to zero at 4.2 K [1]. Unlike the current in normal metals, a superconducting current is not carried by single electrons but by two electrons, bound together in what is referred to as a Cooper pair, named after Leon Cooper, who postulated their existence in 1956 [2]. The superconducting state gets destroyed if the applied current density (current per unit area) is increased above a critical value, J_c.

A diamagnet expels applied magnetic field from its interior, and this was observed for superconductors in 1933 by Walther Meissner and Robert Ochsenfeld [3]. A superconductor achieves this by inducing surface currents that mirror the applied magnetic field, effectively canceling it out. Perfect diamagnetism in superconductors is also known as the Meissner effect, named after its co-discoverer. Just like with too much current, the superconducting state is destroyed if the applied magnetic field is increased above a critical value, H_c.

Under atmospheric pressure, Nb is the element with the highest T_c at 9.2 K. In the hope of increasing the critical values of the temperature, current density and magnetic field, physicists started to systematically synthesize and test various compounds and alloys. This lead to the discovery of the Nb:Ti alloy that has a critical field as high as 14 T [4]. Superconducting magnets are usually constructed from wires of this alloy.

1.2 Advances in Theoretical Understanding

Theoretical explanation for the Meissner effect was provided in 1935 by the London equations [5]. The London equations provide expressions for the electric field, $\vec{E}$, and the magnetic field, $\vec{B}$, inside a superconductor.

$$\vec{E} = \frac{m}{n_s e^2}\frac{\partial}{\partial t}\vec{j_s}, \vec{B} = -\frac{mc}{n_s e^2}\nabla \times \vec{j_s} \tag{1.1}$$

where m is the mass of an electron, n_s is the superfluid density (here superfluid means the charge carriers of the superconductor, i.e the Cooper pairs), e is the charge of an electron, $\vec{j_s}$ is the superconducting current density, and c is the speed of light.

As mentioned earlier, the Meissner effect is when a superconductor cancels an applied magnetic field by inducing current on its surface. Inside the superconductor, the magnetic field is suppressed exponentially and the penetration depth, λ_L, controls how fast this suppression occurs. The London equations may be modified using Ampere's Law to show that $\mathrm{B(r) = B_0 e^{-(r/\lambda_L)}}$, where $\mathrm{B_0}$ is the applied field, $\mathrm{r = 0}$ at the surface of the superconductor and positive inside it, B(r) is the field inside the superconductor and $\lambda_\mathrm{L} = (\sqrt{\frac{\mathrm{mc^2}}{4\pi \mathrm{n_s e^2}}})$. The

London equations show that the larger the superfluid density, the faster the suppression of the applied magnetic field.

In 1957, Bardeen, Cooper, and Schrieffer proposed a theory for superconductivity, known as the BCS theory [6]. Cooper's paper the previous year had shown that in the presence of an attractive potential, two electrons can bind together to form a pair in momentum space. The BCS theory provides a microscopic model that accounts for such an attractive potential. BCS proposes that the 'glue' for pair formation is the electron-phonon interaction. In momentum space, the electron-phonon interaction provides a region near the Fermi surface where phonon mediated attraction between two electrons outweighs the Coulumb repulsion, providing a net attractive interaction that gives rise to Cooper pairing. The Cooper pairs are formed in the spin singlet configuration. The two electrons have opposite spins and the total momentum of the pair is zero. The wave function of the pair is the order parameter for the superconducting state and is characterized by a length scale known as the coherence length, ξ. The BCS theory also predicts the formation of a symmetric s-wave energy gap, Δ, around the Fermi surface. Δ is given by the real part of the order parameter function. At $T = 0$ and energies less than Δ, there are no single electron states. The only charge carriers in that energy range are the Cooper pairs. Δ may also be considered to be the 'binding energy' of the Cooper pairs. In 1960, Ivan Giaever obtained definitive proof for the existence of Δ by planar tunneling experiments into superconductors [7].

1.3 Unconventional Superconductivity

For some superconductors, BCS theory is extremely adept at accurately predicting amplitudes and temperature dependence of properties such as heat capacity, gap size, the isotope effect, penetration depth etc. Most of these superconductors are elemental transition metals and simple metallic compounds. They are collectively called conventional superconductors.

However, for some superconductors, the BCS theory cannot account for the physical properties. The observed critical temperatures are too high to be explained by the electron-phonon interaction. The three big families of such superconductors are the copper based superconductors, the iron based superconductors and the heavy fermion superconductors. The copper and iron based superconductors are also referred to as 'high temperature superconductors' since their critical temperatures are much higher than the elemental metallic superconductors.

Traditionally superconductors whose order parameter symmetry is lower than the underlying lattice, such as d-wave of the copper based superconductors and even more exotic pairing for some of the heavy fermion superconductors, are classified as 'unconventional'. Many have relaxed that definition to include superconductors with order parameter symmetry that is not simple s-wave (such as s_{+-} discussed later) or just superconductors whose properties cannot be explained by electron-phonon coupled BCS.

Conventional superconductors have metallic ground states, i.e they behave as simple metals for $T > T_c$. On the other hand, unconventional superconductivity often competes with, and appears in close proximity to, strongly correlated electron phases. Doniach phase diagrams [8] are helpful in visualizing the competing phenomena in such a compound. At one end of the

phase diagram, the compound is in a correlated non-Fermi liquid like state. This may be a Mott insulating, orbital ordering, spin density wave, charge density wave, heavy fermion or pseudogap phase. The tuning parameter is generally electron/hole concentration by doping, pressure, or strain. As the tuning parameter is varied, the strongly correlated phase is suppressed and at low temperatures superconductivity emerges. Further variation in the tuning parameter reduces the electron correlations even further giving rise to a strange metallic phase before eventually crossing over into a Fermi liquid like state. For some compounds these phases are mutually exclusive while for others superconductivity may coexist with the preceding strongly correlated phase. Figure 1.1 is a simple picture portraying such a phase diagram and is equally applicable to many families of the unconventional superconductors, including the copper based superconductors, heavy fermion superconductors, and iron based superconductors. An understanding of the correlated state would most certainly shed light on the mechanisms of unconventional superconductivity, and therefore may help in the design of new high-temperature superconductors.

Discovered in 1975, the heavy fermions were the first family of tunable superconductors [9, 10], but it was the discovery of the copper based superconductors (cuprates) in 1986 with their extraordinary high T_c, that truly opened a new era for the field [11]. The parent compounds of the cuprates are antiferromagnetic Mott insulators. Superconductivity emerges when this state is suppressed by various means (doping/pressure/strain). LBCO was shown to superconduct at $\sim$ 35 K while YBCO has a T_c of 90 K, well above the boiling point of liquid nitrogen. The underlying feature of the cuprates are their copper oxide (CuO_2) layers. These layers are weakly coupled to each other resulting in a quasi two dimensional electronic structure. The high T_c's

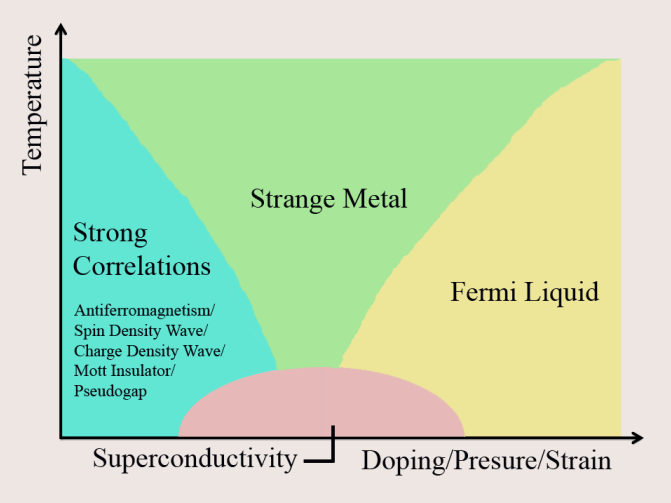

Figure 1.1: A simplified representative phase diagram for unconventional high temperature superconductors. The parent compounds are in a strongly correlated state. When this state is suppressed by various means (doping/pressure/strain) superconductivity emerges. Upon further change in the tuning parameter, the compounds eventually crossover into a Fermi liquid like state. To understand the microscopic mechanism driving the superconducting transition, it is essential to consider its relationship with the correlated state that precedes it.

of the cuprates cannot be accounted for by electron-phonon interaction. In addition, their order parameter symmetry is d-wave, as opposed to s-wave for the conventional superconductors [12]. D-wave symmetry means that the order parameter contains a line node and changes sign after every rotation of $\pi/2$. The origin of the high transition temperatures of the cuprates is still under active debate. A strong candidate for the pairing 'glue' is spin fluctuations, meaning that the electrons attract each other by exchanging collective excitations in the spin channel [13]. Another active topic of research is the mysterious pseudogap region that lies above the superconducting dome for underdoped cuprates [14].

1.4 Iron Based Superconductors

The recent family of tunable superconductors to come along were the iron based superconductors. They were discovered in 2008, causing renewed flurry of activity in the field of high temperature superconductivity [15]. A superconducting family based on Fe came as a surprise, since Fe being a strong ferromagnet was thought to be incompatible with superconductivity. Like the cuprates, the iron based superconductors are also layered materials. Superconductivity takes place in a corrugated layer of Fe and a pnictogen or chalcogen atom. These layers may be separated by rare earth, oxygen, alkaline earth or alkali metals. The critical temperatures vary with the spacer layers being used.

The highest T_c (approaching 60 K) has been observed for the 1111 family (SmFeAsO, GeFeAsO, NdFeAsO, PrFeAsO) [16]. Here the spacer layer is a rare earth element and oxygen and superconductivity is usually induced by substituting O^{2-} with F^{-}.

The most amount of work has been done on the 122 family because large single crystals of this compound can be grown. The spacer layer in their case is an alkaline earth metal. In the case of $BaFe_2As_2$, superconductivity may be induced by electron doping (replacing Fe with Co), hole doping (replacing Ba with K) or isoelectronic doping (replacing As with P) [16]. The maximum T_c for this family is 38 K for $Ba_{0.6}K_{0.4}Fe_2As_2$ [17].

The 111 family has alkali metals as the spacer layers (e.g LiFeAs, NaFeAs) and when doped with Co has a maximum T_c of around 20 K [18]. The 11 family does not have a spacer layer (FeTe, FeSe) and the optimal mix of Te and Se superconducts at $\sim$ 14 K [19].

Figure 1.2 shows the crystal structure for these four families.

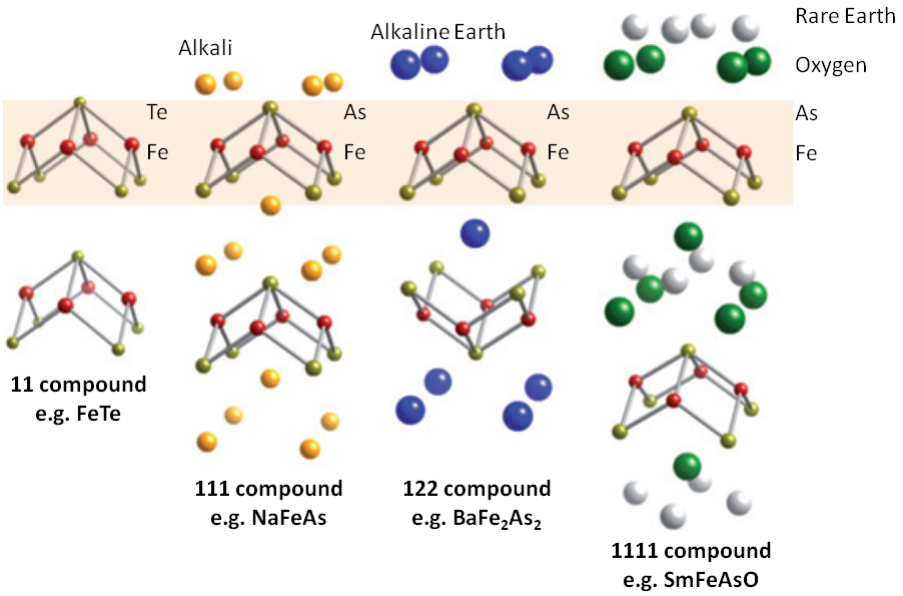

Figure 1.2: The crystal structure for the iron based superconductors. All families have a corrugated layer of Fe and a pnictogen or chalcogen atom. The families are differentiated based upon the spacing layers between the Fe corrugated layers. The maximum T_c for the iron based superconductors is close to 60 K and is obtained for the 1111 family. From [20].

The low temperature ground state of the parent compounds of the iron based superconductors is an antiferromagnetic spin density wave with an orthorhombic or monoclinic crystal lattice. Above the magnetostructural transition (T_N/T_S), they are paramagnets with tetragonal crystal lattice [21, 22]. It is not clear if this transition is driven by magnetic fluctuations [23, 24] or orbital ordering [25, 26, 27, 28, 29]. The suppression of this antiferromagnetic state by various means causes superconductivity to emerge [30]. In certain families of the iron based compounds superconductivity and antiferromagnetism coexist.

Unlike the cuprates, the iron based compounds are not insulating in their normal state, rather they are classified as 'bad metals'. The valence electrons of the Fe atoms occupy the $3d$ orbitals. The valence p orbitals of the pnictogen/chalcogen atoms hybridize with the iron $3d$ orbitals giving

rise to a multicomponent Fermi surface. The electronic band structure has been calculated using the local density approximation [31]. The Fermi surface comprises of multiple quasi-2D sheets. There are two near-circular hole pockets at the Γ point, the center of the Brillouin zone. Two elliptical electron pockets exist at $(0, \pi)$ and $(\pi, 0)$. For some compounds, there is an additional hole pocket at the (π, π) point (e.g. F doped LaFeAsO [32]). Figure 1.3 (a) shows the Fermi surface geometry in the unfolded Brillouin zone [33].

No consensus has been reached so far regarding the order parameter symmetry of the iron based superconductors. The relevant interactions are the inter-pocket electron-hole interaction, U_{eh}, and the intra-pocket electron-electron interaction, U_{ee}. The direct interaction between the electron pockets is weak and is instead dominated by an effective interaction that involves virtual hopping to the hole Fermi surfaces. The two likely pairing symmetries are s_{+-} and s_{++}. s_{+-} means that the order parameter changes sign between electron and hole pockets while s_{++} means that the sign remains the same. s_{+-} symmetry is expected to occur if the effective U_{ee} is attractive and U_{eh} is repulsive. s_{++} symmetry shall occur if both U_{ee} and U_{eh} are attractive. Spin, charge, and orbital fluctuations and even phonons contribute to the interactions between the multiple electron and hole Fermi surfaces. The interactions also depend on the angles between the Fermi surfaces, which is very likely to give a superconducting gap some anisotropy, and maybe even 'accidental' nodes.

Figure 1.3 (b) is a cartoon representation of the superconducting order parameter for various cases [34]. The height of the cylinders represents the magnitudes and signs of the order parameters.

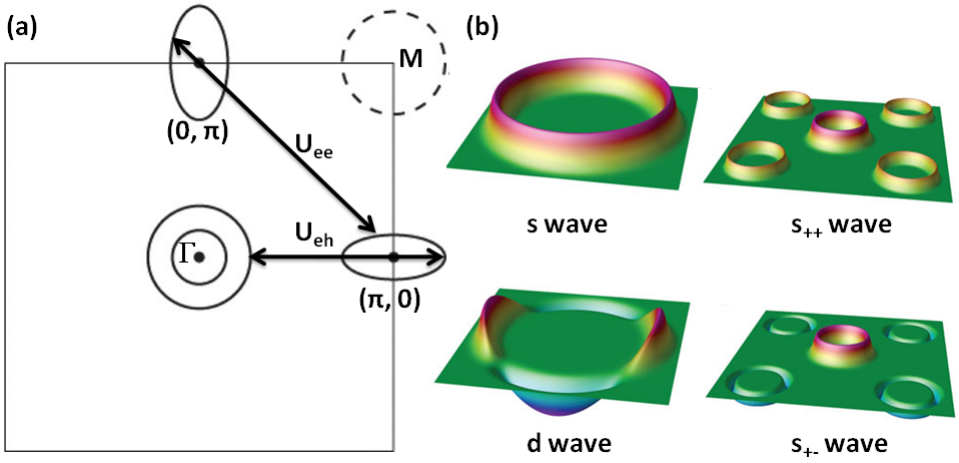

Figure 1.3: (a) The Fermi surface geometry of the iron based superconductors in the unfolded Brillouin zone. The are two circular hole pockets centered at the Γ point. Elliptical electron pockets are present at $(0, \pi)$ and $(\pi, 0)$. For some compounds, there is an additional hole pocket at the (π, π) point [32]. Intra- and inter-pocket interactions, U_{ee} and U_{eh}, respectively, determine the superconducting order parameter symmetry. Adapted from [33]. (b) Cartoon representation of the order parameter for various superconductor order parameter symmetries. The height of the cylinders represents the magnitudes and signs of the order parameters. For conventional s-wave compounds there is one band of uniform magnitude. For d-wave compounds, the order parameter has a line node and changes sign after every rotation of $\pi/2$. For s_{++}, there are multiple bands with the same sign. For s_{+-}, the order parameter has different signs for different bands. Adapted from [34].

This thesis is concerned with probing the the iron based superconductors using point contact spectroscopy. Special attention is paid to the correlated 'normal' state of these compounds, and its relationship with the superconducting state that emerges from it. Chapter 2 describes point contact spectroscopy, how the measurement is carried out and what it is sensitive to. Chapter 3 shows point contact spectroscopy results for the iron based compounds in their superconducting state while Chapter 4 covers the non-superconducting dopings and temperatures. Chapter 5 deals with diagnostics on point contact junctions, discussing the framework used to determine junction quality. Chapter 6 presents point contact measurements under applied magnetic field and stress. Chapter 7 summarizes the results laid out in the thesis and provides future work recommendations.

CHAPTER 2

POINT CONTACT SPECTROSCOPY

2.1 Discovery of PCS

Planar tunneling into superconducting Pb gives nonlinearities in the conductance corresponding to the Eliashberg function, $\alpha^2F(\omega)$, as was first demonstrated by McMillan and Rowell in 1965 [35, 36]. $F(\omega)$ is the density of the vibrational modes (phonons) with frequency ω and α^2 is the coupling constant of these phonons to the electrons. If the Pb is driven normal (by applying magnetic field or raising temperature), conductance is constant as per Harrison's theorem [37].

Harrison's theorem calculates the tunneling current for planar tunneling into a Fermi liquid at low bias. The tunneling current integral incorporates both the Fermi velocity and the density of states. For normal metals:

$$\text{Fermi velocity} = \frac{1}{\hbar}\frac{\partial E}{\partial k_x}, \text{density of states} = \frac{L}{\pi}(\frac{\partial E}{\partial k_x})^{-1} \tag{2.1}$$

These two quantities cancel each other out leaving the tunneling current with no density of states information, and the experimentally measured conductance is constant.

In 1974, however, I. K. Yanson found nonlinearities corresponding to $\alpha^2F(\omega)$ in a shorted Pb planar tunnel junction where the Pb had been driven normal by applied magnetic field [38]. Yanson and co-workers showed that

their observed nonlinearities arose from the nano-shorts, or 'point contacts' through the tunnel barrier. The measurement, therefore, was not tunneling, but quasiparticle scattering; hence point contact spectroscopy (PCS) is also called quasiparticle scattering spectroscopy (QPS). Since planar tunneling could only detect the phonon spectra of superconducting metals, PCS turned out to be an excellent method of determining the phonon spectra and bosonic modes for high conductivity normal metals (e.g. Cu, Ag) that do not superconduct. In 1995, A. V. Khotkevich and I. K. Yanson published an atlas containing the phonon spectra of 31 metals determined by point contact spectroscopy [39]. Yanson's 2005 book [40] provides a thorough accounting of point contact spectroscopy and its applications.

2.2 What PCS Detects

A point contact is simply a contact between two metals whose characteristic size d is much less than the electron elastic and inelastic mean free paths: $l_{el}, l_{in} >> d$. PCS detects the non-linearities of the current-voltage $(I - V)$ characteristics of these metallic constrictions. The bias voltage applied to the point contact junction defines the energy scale of the scattering process. If both metals are ohmic, the $I - V$ curve is linear and the differential conductance dI/dV is constant. However, when scattering processes are present, they show up in the PCS spectrum.

As mentioned above, PCS was initially used to study electron-phonon interactions in metals. PCS is also sensitive to magnons, and any other bosonic excitation that couples to the conduction electrons. The reason is that the point contact junction injects electrons a scattering length into the bulk of the sample, and the electron-boson coupling is detected when the electron is

inelastically backscattered into the orifice: scattering is detected as a slight decrease in the conductance due to the backflow of electrons. This is a small effect and is detected as dips in the second harmonic d^2I/dV^2. The equations for this phenomenon are presented in section 2.4.

If one of the metals is replaced by a superconductor, making an N-S junction, Andreev reflection [41] is observed. PCS on superconductors is discussed in detail in the section 2.5.

Recent work has shown that the PCS technique detects density of states arising from strong electron correlations. For heavy fermion compounds, the onset of the Kondo lattice appears as a Fano line shape in the PCS spectra [42]. PCS is also sensitive to the hybridization gap and Fano resonance in the heavy fermion URu_2Si_2 [43].

Chapter 4 of this thesis discusses how PCS is sensitive to orbital fluctuations (seen as a density of states effect) above the structural phase transition in the iron based compounds.

2.3 Different Conduction Regimes in a Point Contact

A point contact junction is described by three different conduction regimes depending on the relative sizes of the contact d, and the electron elastic and inelastic mean free paths l_{el}, l_{in} [44].

(i) The ideal situation is when $l_{el}, l_{in} >> d$ and the point contact is said to be in the ballistic or Sharvin limit. This is the best regime for PCS as the carrier energy is dissipated far from the junction area. Nonlinearities in the $I - V$ curve are then a spectroscopic (energy-dependent) measurement of quasiparticle scattering.

(ii) If elastic and inelastic scattering occurs in the junction, spectroscopic information gets smeared out. This happens if $l_{el}, l_{in} << d$ and the point contact is said to be in the thermal or Maxwell limit. Almost all energy is dissipated in the junction area, causing a local increase in temperature. The dI/dV spectrum then mirrors the temperature dependence of the bulk resistivity.

(iii) In between these two extremes is the diffusive limit, when $l_{el} < d < \sqrt{l_{el} * l_{in}}$. The quasiparticles can now experience elastic scattering processes inside the junction area but not inelastic ones. Spectral information is still preserved but the measured conductance spectrum has a weaker intensity.

Figure 2.1 shows cartoon figures to represent the three cases. The biggest challenge in conducting point contact spectroscopy experiments is making sure that the contact is either in the ballistic or diffusive regime so that the observed nonlinearities in the dI/dV spectrum actually correspond to elementary excitations and not bulk resistivity effects. Chapter 5 discusses in detail how we ensure that our point contact junctions are in the correct regime and are not being impacted by joule heating.

The resistance for a point contact junction of arbitrary size may be expressed using a formula derived by Wexler [45]:

$$R_0 = \frac{4\rho K}{3\pi d}\left[1 + \Gamma(K)\frac{3\pi}{8K}\right] = R_{Sharvin} + \Gamma(K) * R_{Maxwell} \tag{2.2}$$

where $K = l/d$, with $1/l = 1/l_{el} + 1/l_{in}$, $\Gamma(K)$ is a correction factor and ρ is the sample resistivity. $\Gamma(K)$ lies between 0.694 and 1 and is determined by solving the integral as described in Eq. 45 of [45].

$$\Gamma(K) = \frac{9K^2}{8}\int_0^\infty \sum_{n=1}^{3} B_n(t)\Phi_n(Kt)dt \tag{2.3}$$

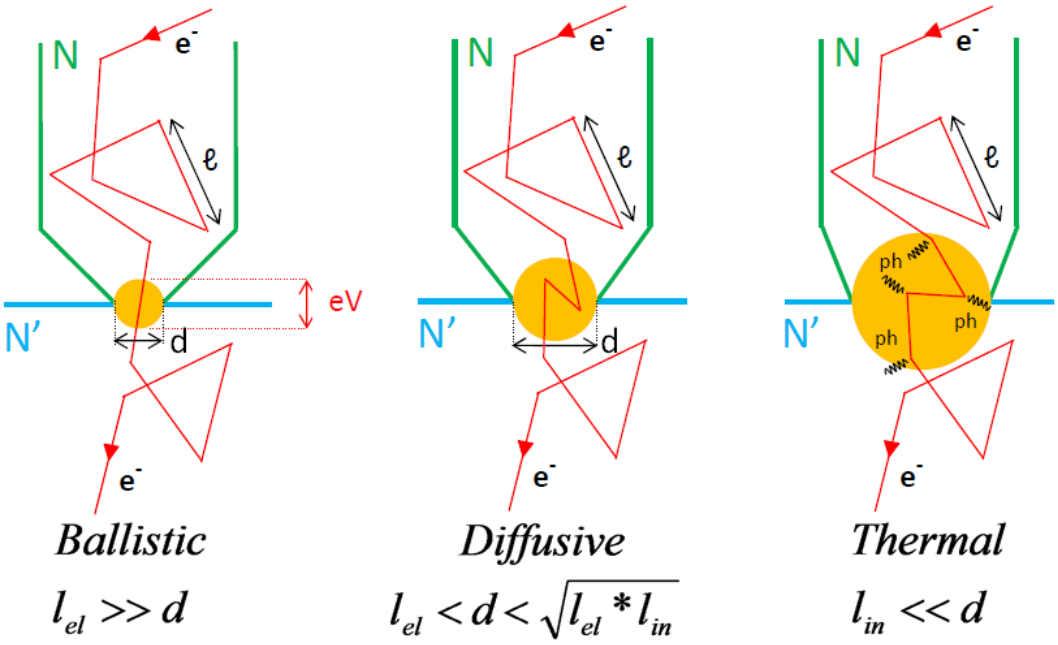

Figure 2.1: Cartoon illustrating the regimes for a point contact junction. The contact size d is represented by the gold colored circle. l is the length traveled by the electron between collisions. In the ballistic regime, no collisions occur inside the contact area and the electron gains energy eV on crossing the junction. Spectroscopic information is preserved. In the thermal regime, inelastic scattering processes occur inside the junction and the energy eV is lost at the contact, causing Joule heating. Spectroscopic information is lost to thermal smearing. In the diffusive regime, elastic scattering occurs inside the junction and some spectroscopic information is preserved. Adapted from [44].

In the Sharvin limit, $K >> 1$ and $\Gamma(K) \to 0.694$ which reduces the Wexler formula to $R_0 = \frac{4\rho l}{3\pi d^2}$. In the Maxwell limit $K \to 0$ and $\Gamma(K) \to 1$ which equates the junction resistance with the bulk metal resistance $R_0 = \frac{\rho}{2d}$.

2.4 Point Contact Spectroscopy and Bosonic Excitations

The current density j through a point contact junction normal to the z-axis is given by [40]:

$$j_z = e \int_{\epsilon_F - eV/2}^{\epsilon_F + eV/2} d\epsilon \int \frac{d\Omega}{4\pi} f(\epsilon) v_z(\epsilon) N(\epsilon) \tag{2.4}$$

where V is the bias across the junction, $d\Omega$ is the solid angle differential, $f(\epsilon)$ is the Fermi function, v_z is the Fermi velocity along the z-direction and $N(\epsilon)$ is the density of states (DOS) of the sample. For normal, non-correlated metals, $v_z(\epsilon)$ is inversely proportional to $N(\epsilon)$, resulting in no nonlinearity in the $I - V$ curves, and Ohm's law is valid for the point contact. However, if energy dependent scattering processes are present, and the DOS and Fermi velocity vary with the bias voltage, the measured dI/dV reflects the DOS.

Electrons passing through the junction gain the excess energy, eV. If phonon modes exist at this energy some electrons get backscattered and do not contribute to the current. dI/dV shows the dependence of the scattering cross section on energy and the second derivative d^2I/dV^2 resembles the Eliashberg spectral function $\alpha^2F(\omega)$ of the electron-phonon interaction [44]. At $T = 0$,

$$d^2I/dV^2 = \frac{8ed}{3\hbar v_F} \langle K \rangle \, \alpha^2 F(eV) \tag{2.5}$$

where $\langle K \rangle$ is the geometric form factor averaged over the Fermi surface and depends on the scattering angle between the initial and final electron momenta. This analysis is not exclusive to phonons and may also be used to represent scattering from other bosonic excitation mechanisms such as magnons [40].

2.5 Point Contact Spectroscopy on Superconductors

In recent years, PCS has proved to be a very useful tool to probe superconductors by Andreev reflection [41]. When a material goes superconducting, a gap Δ opens up in its density of states at the Fermi level. The existence of this gap was experimentally proven by planar tunneling using a normal metal/insulator/superconductor (NIS) junction [7]. If the tunnel junction is biased with energy $eV < \Delta$, an injected electron cannot enter the superconductor as no states exist below Δ for it to occupy. Therefore no current flows and $dI/dV = 0$. If the bias voltage is increased to $eV = \Delta$, current starts to flow and dI/dV exhibits sharp peaks at the gap extrema, mapping out the quasiparticle density of states in the superconducting phase.

In the point contact setup, there is a clean metallic NS junction with no intervening insulating layer. An injected electron with energy $eV < \Delta$ is still quantum-mechanically forbidden to enter the superconductor alone. On striking the interface, it enters the superconducting condensate as a Cooper pair by retroreflecting a hole with the opposite spin and momentum back into the normal metal. The formation of the new Cooper pair results in the transfer of charge $2e$ across the interface. This phenomenon is known as Andreev reflection and occurs within a coherence length of the NS interface. Each injected electron transfers a double charge, and for $eV < \Delta$, dI/dV

normalized with respect to the normal state is 2 instead of the 0 observed for the NIS case. Figure 2.2 shows a cartoon depicting Andreev reflection.

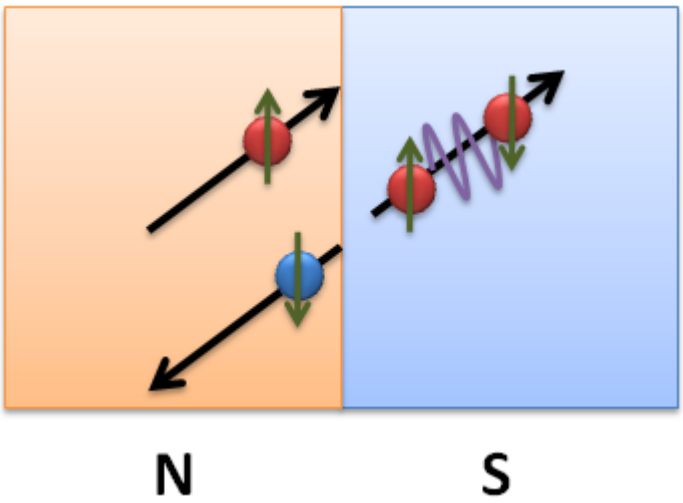

Figure 2.2: Andreev reflection at a transparent NS interface. When an electron (red circle) is incident on the superconductor from the normal metal side, a hole (blue circle) with the opposite spin and momentum is retroreflected back into the normal metal and the electron enters the superconducting condensate as a Cooper pair. Charge $2e$ gets transferred across the interface.

Fermi velocity mismatch between the normal metal and the superconductor causes a barrier to appear even in a metallic NS junction. Andreev reflection is also suppressed by a dirty interface. Consequently, some of the incident electrons undergo specular reflection. (In the NIS case, the barrier is the insulator that suppresses all Andreev reflection i.e all incident electrons undergo specular reflection). These parameters are incorporated in the Blonder-Tinkham-Klapwijk (BTK) theory [46] and used to fit PCS data on superconductors, as described below.

2.5.1 BTK Theory

The beauty of the BTK theory is that it can model N-S junctions with variable barrier strengths at the interface. For the reasons mentioned above,

typically the experimentally obtained PCS dI/dV spectrum does not show a full 100% enhancement for $eV < \Delta$. Instead, a dip occurs at zero bias and peaks appear just inside Δ. To reproduce the experimental data, the BTK model starts of with the Bogoliubov equations:

$$i\hbar\frac{\partial f}{\partial t} = \left(-\frac{\hbar^2}{2m}\nabla_x^2 - \mu(x) + V(x)\right) f(x,t) + \Delta(x)g(x,t) \tag{2.6}$$

$$i\hbar\frac{\partial g}{\partial t} = -\left(-\frac{\hbar^2}{2m}\nabla_x^2 - \mu(x) + V(x)\right) g(x,t) + \Delta(x)f(x,t) \tag{2.7}$$

assuming a constant chemical potential μ and superconducting gap Δ. The barrier at the interface is modeled as a delta function $V(x) = H\delta(x)$, with the barrier strength defined by a unitless parameter $Z = H/\hbar v_F$. A low Z corresponds to a high transparency Andreev reflection dominated junction while a high Z suppresses Andreev reflection, moving towards a tunneling dominated junction. The Bogoliubov equations reduce to Schrodinger equation for normal metals ($\Delta = 0$). f is the electron wave function while g is the hole wave function.

If the bias voltage $eV < \Delta$, an electron injected from the normal metal side with momentum q^+ can undergo one of two processes: either Andreev reflection ($q^+ \rightarrow -q^-$) or normal specular reflection ($q^+ \rightarrow -q^+$). Once the bias voltage $eV > \Delta$, in addition to Andreev and normal reflection, two additional transmission processes occur. The incident electron may be simply transmitted with a wave vector on the same side of the Fermi surface ($q^+ \rightarrow k^+$) or with a crossing of the Fermi surface ($q^+ \rightarrow -k^-$) called a 'branch crossing'. Figure 2.3 (a) shows the energy-momentum diagram for these four

processes. Quasiparticles inside the superconductor may be described using

$$\psi(x,t) = \begin{pmatrix} f(x,t) \\ g(x,t) \end{pmatrix} \tag{2.8}$$

where f and g are the electron and hole components of the quasiparticle. Using plane waves, the incident, reflected and transmitted wavefunctions are:

$$\psi_{inc} = \begin{pmatrix} 1 \\ 0 \end{pmatrix} e^{iq^+x}, \tag{2.9}$$

$$\psi_{ref} = a\begin{pmatrix} 0 \\ 1 \end{pmatrix} e^{iq^-x} + b\begin{pmatrix} 1 \\ 0 \end{pmatrix} e^{-iq^+x}, \tag{2.10}$$

$$\psi_{trans} = c\begin{pmatrix} u_0 \\ v_0 \end{pmatrix} e^{ik^+x} + d\begin{pmatrix} v_0 \\ u_0 \end{pmatrix} e^{-ik^-x}. \tag{2.11}$$

The probability for Andreev reflection is $A = a^*a$, normal reflection is $B = b^*b$, transmission without crossing the Fermi surface is $c^*cN_S(E)$ and transmission with crossing the Fermi surface is $d^*dN_S(E)$, where $N_S(E)$ is the quasiparticle density of states of the superconductor. Using these probabilities, the current across the junction is determined to be:

$$I_{NS} = I_0 \int_{\infty}^{-\infty} [f(E - eV) - f(E)][1 + A(E) - B(E)]dE \tag{2.12}$$

The BTK model is remarkably accurate at simulating the differential conductance across N-S junctions. The simulated curves in Figure 2.3 (b) show how the dI/dV spectrum changes with Z. For large values of Z, Andreev reflection is suppressed and planar tunneling results are reproduced.

Experimental data tends to be more smeared out than what the BTK model predicts. This might be due to degradation of the superconducting layer or some inelastic scattering at the junction. Better fits are obtained by introducing a factor Γ for the finite lifetime of the quasiparticles [47, 48]. Γ

has units of energy and is given by $\hbar/\tau$, where τ is the quasiparticle lifetime. Adding Γ changes the Bogoliubov equations to:

$$i\hbar\frac{\partial f}{\partial t} = \left(-\frac{\hbar^2}{2m}\nabla_x^2 - \mu(x) + V(x) - i\Gamma\right) f(x,t) + \Delta(x)g(x,t) \tag{2.13}$$

$$i\hbar\frac{\partial g}{\partial t} = -\left(-\frac{\hbar^2}{2m}\nabla_x^2 - \mu(x) + V(x) - i\Gamma\right) g(x,t) + \Delta(x)f(x,t) \tag{2.14}$$

For a fixed value of Z=0.15, Figure 2.3 (c) simulates curves for different values of the ratio Γ/Z. As Γ increase, the Andreev reflection signal is sharply reduced. Good junctions are distinguished by small values of Γ.

Finite temperatures cause the signal to be thermally smeared. In addition, the magnitude of Δ decreases as T approaches T_c. For a fixed value of Z=0.15, Figure 2.3 (d) simulates curves at finite temperature for a conventional superconductor where the temperature evolution of Δ follows the BCS theory, $\Delta = \Delta_0 \tanh[1.74 * \sqrt{\mathrm{T_c/T} - 1}]$.

2.5.2 Extensions to the BTK Model

The original BTK model assumes an isotropic s-wave superconductor. Since then, the model has been extended to model d-wave [49], p-wave [50], and multiband superconductors [51].

To solve the BTK equation for a d-wave superconductor, the constant Δ needs to be replaced by $\Delta(\theta) = \Delta_0 cos[2(\theta - \alpha)]$. Here θ is the angle the injected electron makes with the normal of the junction interface and α the angle between the interface normal and the antinodal gap direction. Figure 2.4 shows BTK curves with different Z values for a d-wave superconductor. The figures depict the results for junctions constructed along the antinodal direction ($\alpha = 0$) and the nodal direction ($\alpha = \frac{\pi}{4}$). For transparent junctions,

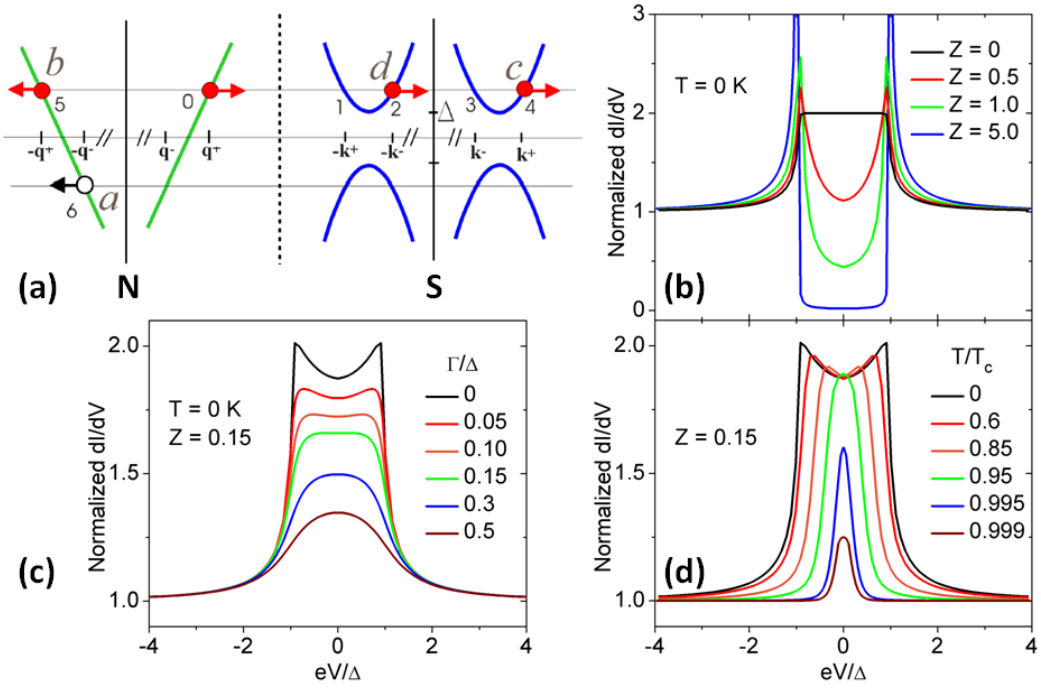

Figure 2.3: (a) A simplified Energy vs. Momentum diagram for an electron with momentum q^+, denoted by 0, encountering a Normal Metal/Superconductor interface. It may be (i) retroreflected back into the normal metal as a hole with momentum $-q^-$, denoted by a, and thus transfer a Cooper pair into the superconductor (Andreev reflection) (ii) specularly reflected with momentum $-q^+$, denoted by b (iii) transmitted across the barrier without crossing the Fermi surface with momentum $k^+ > k_F$, denoted by c (iv) transmitted across the barrier with crossing the Fermi surface with momentum $-k^- < k_F$, denoted by d. The electron cannot occupy the spots 1 and 3 on the energy band since that would violate charge/momentum conservation. Adapted from [46]. (b) BTK calculations at T = 0 K for different values of Z, the barrier strength at the N/S interface. As Z increases, Andreev reflection is suppressed. (c) BTK calculations at T = 0 K for different values of the ratio Γ/Z. A large Γ reduces the Andreev reflection signal and is a sign of inelastic scattering at the interface. (d) BTK calculations at finite temperatures for a conventional superconducting gap that follows the BCS temperature dependence. As T approaches T_c, the magnitude of Δ decreases and the magnitude of the Andreev reflection signal becomes smaller.

both directions give similar spectra. However, as Z increases, the antinodal direction develops a sharpening dip at zero bias while the nodal direction develops a sharpening peak at zero bias. Thus by making point contact junctions along different crystallographic axes, the location of the node in the superconducting order parameter may be determined [42].

For multiband superconductors, the BTK model simulates the dI/dV curves by taking a weighted average of two single band calculations. Thus $dI/dV_{\text{total}} = w * dI/dV_{\text{FirstBand}} + (1 - w) * dI/dV_{\text{SecondBand}}$. A recently discovered multiband superconductor is MgB_2, and PCS spectra on it shows features corresponding to two gaps. The value of w changes across junctions depending on how much of each Fermi surface the point contact picks up [52].

2.6 PCS junction designs

In this section we will cover the procedure by which we make point contact junctions on our samples. PCS is a near-surface sensitive technique in that it probes the sample up to the length scale of the electron mean free path. A 'dead' layer (e.g insulating oxide, impurity) on the sample can distort the PCS spectrum. A problem when dealing with novel and high temperature superconductors which are often layered compounds is that as grown, different atomic layers may be exposed at the surface. This may result in the surface comprising of superconducting and non-superconducting regions, which in turn reduces the intensity of the point contact conductance spectrum. Therefore, we take special care and construct all our junctions on crystal surfaces freshly cleaved in a dry Nitrogen or Argon environment, and minimize the time for which they are exposed to the atmosphere. I have used

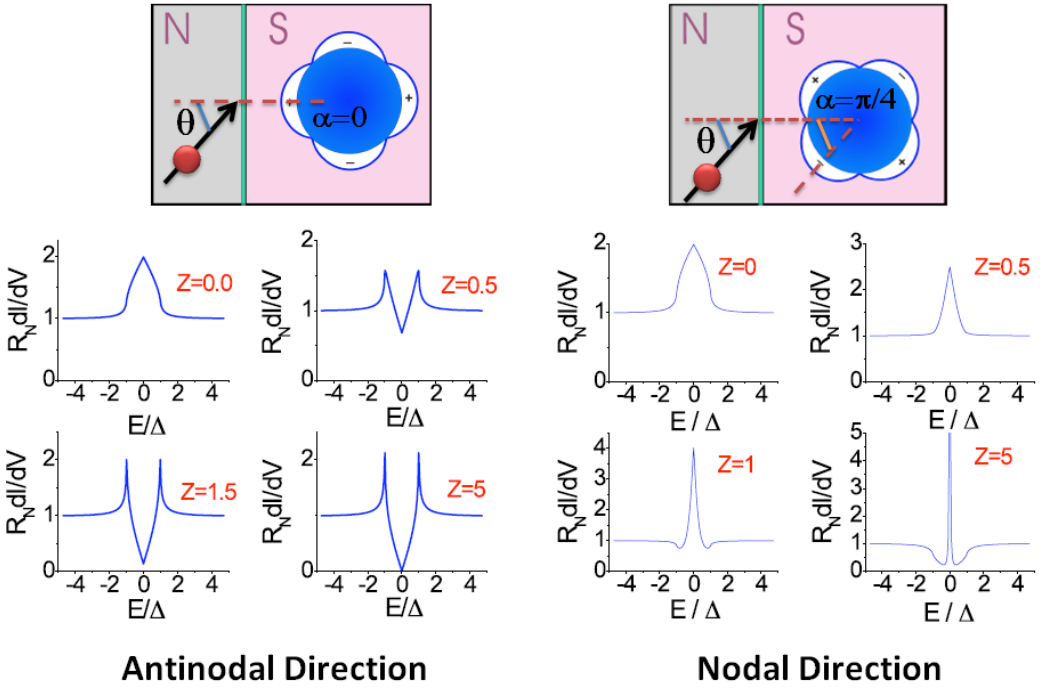

Figure 2.4: Andreev reflection spectroscopy for a d-wave superconductor. Instead of a constant Δ, $\Delta(\theta) = \Delta_0 cos[2(\theta - \alpha)]$, where θ is the angle between the injected electron and the interface normal and α is the angle between the interface normal and the antinodal gap direction. BTK curves are presented for point contact junctions made along the antinodal ($\alpha = 0$) and nodal ($\alpha = \frac{\pi}{4}$) directions. For low Z values, both directions look the same, but as Z increases, the antinodal direction develops a dip while the nodal direction develops a peak. This shows that point contact spectroscopy can determine the location of the nodes in the superconducting order parameter. Modified from [53, 54].

two techniques to construct point contact junctions: the needle-anvil method and the soft PCS method [44]. Our experimentally measured quantity is differential conductance dI/dV as a function of bias voltage at different values of temperature and applied magnetic field. Similar spectra are obtained from both methods. Figure 2.5 (a) shows cartoon representations of the two methods.

In needle-anvil PCS, a sharp tip is brought into direct contact with the sample. The tip is etched electrochemically and lowered into contact using a micrometer screw gauge with 70nm sensitivity. Gold is used since it is an inert normal metal and etches very nicely to make long, tapered tips. By scanning electron microscopy, the edge of the tip is found to be ~ 5 μm. The sharp end of the tip is curled slightly so that it acts as a small spring which provides stability to the junction and ensures that the tip remains in contact with the sample in the face of small environmental vibrations. Figure 2.5 (c) has a photograph of an etched gold tip while Figure 2.5 (d) shows the custom built probe that we use, with the micrometer screw gauge at the top and the tip and sample holder at the bottom. The length of the probe matches the length of the cryostat in the lab. Our probe was designed and built by Xin Lu [55].

The advantage of needle-anvil PCS is that the resistance of the junction can be finely tuned by varying the pressure applied by the tip on the sample. In addition, different junctions on different parts of the sample may be formed in the same cool down. The biggest problem with the needle-anvil method is thermal stability. As the temperature of the sample is varied, thermal expansion of the tip makes the junction unstable. Another issue is the difficulty in aligning the tip to hit micrometer size crystals.

The end of the tip may be larger than the electron mean free path and still provide us with spectral information. This happens because the whole tip does not behave as a single channel, instead there are multiple parallel nanoscale channels dominating the current flow. A more accurate representation of what the needle-anvil junction actually looks like is shown in Figure 2.5 (b).

Soft PCS was the first PCS technique, developed by I. K. Yanson [40], who observed deviations from Ohm's Law in planar tunnel junctions containing microshorts. To construct soft PCS junctions, after cleaving the sample in a dry Nitrogen or Argon environment we sputter or thermally evaporate $\sim$ 50 Å AlO_x onto it to act as an insulating barrier. An aluminum foil wire of thickness 5 μm is attached to the top of the oxide layer using Ag paint, which acts as the counter electrode. Parallel, nanoscale channels are introduced for current flow by fritting [56] across the oxide layer. In fritting, short current pulses are applied across the junction to open or close conduction channels in the insulating barrier. In lieu of AlO_x, we have also obtained good results by using a 50Å thick layer of thermally evaporated Germanium as the insulating barrier.

The advantage of soft PCS is that it is thermally stable over wide temperature ranges and there is less chance of inducing pressure or strain on the sample that may occur in the needle-anvil method. The disadvantage is that we have little control over the junction resistance.

The iron based superconductors are sensitive to air which makes PCS on them challenging to carry out. A large percentage of junctions formed using the electrochemically polished Au tip show insulating behavior. This is most likely due to crystal surface degradation and the Au tip being too soft to break through the 'bad' layer on the top of the crystal to access the superconducting

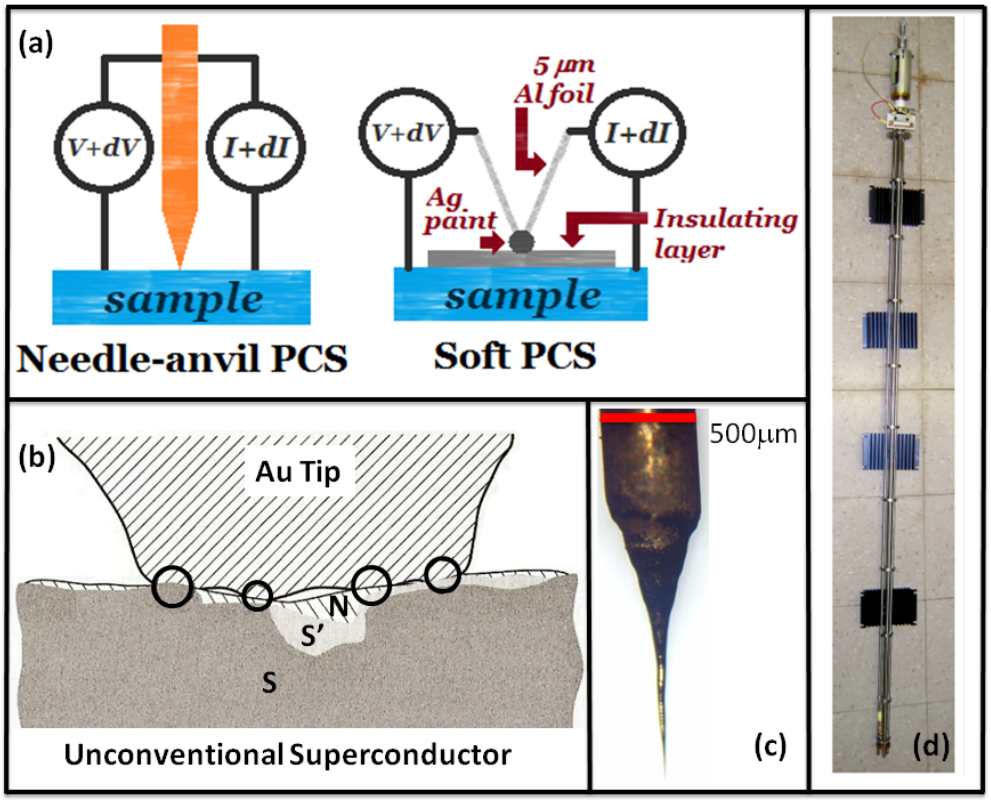

Figure 2.5: (a) The experimental setup for conducting needle-anvil and soft PCS measurements. In the needle-anvil method, an electrochemically etched Au tip is mechanically lowered into contact with the sample. In the the soft PCS method, an insulating layer of $\sim$ 50 Å AlO_x or Ge is deposited on the sample. Silver paint is used to make the contact on top of the insulating layer. Nanoscale conductance channels are then introduced in the insulating layer by fritting [56]. (b) A point contact junction is unlikely to comprise of just one conduction channel. Instead, conductance between the Au tip and the sample is dominated by multiple parallel nanoscale contacts. This provides spectral information even if the tip is larger than the mean free path. However, it may lead to complications if the sample surface is non-uniform or degraded. Modified from [40]. (c) A photograph of a Au tip used to make needle-anvil point contact junctions. It has been sharpened by electrochemical etching. (d) A photograph of the custom built probe used to carry out needle-anvil PCS. The micrometer is at the top of the probe while the tip and sample are situated at the bottom. The length of the probe matches the length of the cryostat in the lab [55].

volume underneath. Best results with the Au tip are obtained once the crystal is etched with aqua regia, followed by an immediate cool down and junction formation. It is easier to obtain clean junctions with soft PCS. This is because once they are cleaved, the crystals are immediately transferred to a high vacuum deposition chamber. Their surface is then covered with AlO_x or Germanium, which prevents degradation of the crystal.

A bigger challenge with soft point contact is obtaining junctions that are in the ballistic or diffusive limit. The droplet of Ag paint used to make the contact is $\sim$ 100 μm large, and our aim is for most of it to only see the insulating AlO_x or Ge layer, with the bulk of the transport occurring through the microshorts that have been induced by fritting. Good data is obtained for junctions with resistance between 20Ω to 80Ω. We find that anything smaller than 20Ω is in the thermal limit so there is too much thermal smearing; while anything larger than 80Ω shows insulating behavior. With our current junction growth procedure, we have a success rate of 10-20%.

We connect our point contact junctions to the measurement setup in the standard four-probe configuration and take $I-V$ and dI/dV curves to characterize them. dI/dV provides more insight into our junctions. However, just mathematically differentiating $I-V$ to obtain dI/dV gives noisy results. Thus dI/dV is measured directly using ac modulation with lock-in amplifiers. As the junction is biased at some finite dc voltage V_0 with current I_0, we use a lock-in to add a small ac voltage δv at frequency ω to the dc voltage biasing the junction. This causes a corresponding change in the measured current by δi. Now the net current I may be written as a Taylor

expansion:

$$I(V_0 + \delta v \cos(\omega t)) = I(V_0) + \left.\frac{dI}{dV}\right|_{V_0} (\delta v \cos(\omega t)) + \left.\frac{d^2 I}{2dV^2}\right|_{V_0} (\delta v^2 \cos^2(\omega t) + ... \tag{2.15}$$

$$I(V_0 + \delta v \cos(\omega t)) = I(V_0) + \left.\frac{dI}{dV}\right|_{V_0} (\delta v \cos(\omega t)) + \left.\frac{d^2 I}{4dV^2}\right|_{V_0} (\delta v^2 (\cos(2\omega t) + 1) + ... \tag{2.16}$$

We use a second lock-in amplifier to measure the ac current signal at frequency ω, and that is proportional to dI/dV. If we measure the ac current signal at frequency 2ω, the result shall be proportional to d^2I/dV^2. In our measurements, we use a δv of $\sim 100\mu$V and ω= 633Hz. If δv is kept too small, the signal will have a smaller signal to noise ratio while if it is made too large, it causes voltage broadening that appears as thermal broadening effects in the junction.

CHAPTER 3

ANDREEV REFLECTION SPECTROSCOPY ON THE IRON BASED SUPERCONDUCTORS

Point contact spectroscopy (PCS) proves to be an extremely useful spectroscopic technique for studying conventional and unconventional superconductors since it is sensitive to the magnitude and symmetry of the superconducting order parameter. As mentioned in Chapter 2, a point contact junction consists of a nanoscale metallic contact with a superconductor, with transport across the junction dominated by Andreev reflection [41]. The density of states may be directly extracted from the conductivity using the Blonder-Tinkham-Klapwijk (BTK) model [46]. PCS was instrumental in determining the precise location of the line nodes for the heavy fermion compound $CeCoIn_5$ [42], and in providing direct evidence for the multi-gap nature of the superconductor MgB_2 [52].

A number of research groups have utilized PCS to study the iron based superconductors. The results are well summarized in a recent review article by Daghero et al [57]. For the $Ba(Fe_{1-x}Co_x)_2As_2$ and $Ba_{1-x}K_xFe_2As_2$ families, measurements on near optimal and overdoped samples have revealed the existence of multiple gaps consistent with s-wave pairing [58, 59]. To our knowledge, no results have been reported for underdoped compounds, which we believe constitutes the most fascinating region of the 122 family phase diagram. Same underdoped compounds exhibit a coexistence of magnetism and superconductivity at low temperatures [16] and some exhibit nematic fluctuations in their normal state [60].

In this chapter, we present our results on point contact junctions constructed on various iron based superconductors. We have looked at the $BaFe_2As_2$ family with electron, hole and isoelectronic doping. Electron doping is achieved by replacing Fe with Co, hole doping occurs by substituting K for Ba, and isoelectronic doping happens when P takes the place of As. We also present data on the 111 family $NaFe_{1-x}Co_xAs$.

We obtain cleaner data with full temperature evolutions on the electron and hole doped $BaFe_2As_2$. For P doping and $NaFe_{1-x}Co_xAs$, the crystals appear to be more reactive in air and their smaller size (150-250 μm) makes them more difficult to handle. We often end up with incomplete temperature evolutions as warming up the crystals would drastically alter the junction quality. Therefore we shall first discuss in greater detail electron and hole doped $BaFe_2As_2$ before moving on to the other compounds.

3.1 Electron and Hole Doped $BaFe_2As_2$

Our Andreev reflection data indicates multiple s-wave superconducting gaps for electron underdoped $Ba(Fe_{1-x}Co_x)_2As_2$ ($x = 0.05, 0.055$) and hole underdoped $Ba_{0.8}K_{0.2}Fe_2As_2$. We also present data on near optimal electron doped $Ba(Fe_{1-x}Co_x)_2As_2$ ($x = 0.07, 0.08$) that is in agreement with the published PCS literature.

We fit our lowest temperature data using the extended BTK model with two s-wave superconducting gaps [51]. All the point contact junctions are nominally constructed along the c-axis. Most junctions span multiple cleavage planes and it is thus likely that occasionally, some electrons are injected along the a-b plane as well. All point contacts show split Andreev peaks and none of the compounds have a maximum at zero bias voltage. This indicates

that it is very likely that the superconducting order parameter does not have any nodes and the Fermi surfaces are fully gapped.

We define the superconducting transition by two temperatures: T_c^{onset}, for when the resistive transition starts, and T_c^{bulk}, for when it falls by 90% of the value at T_c^{onset}. The electron underdoped compounds show an Andreev reflection like conductance enhancement starting between T_c^{bulk} and T_c^{onset} which we argue arises most likely from inhomogenous doping effects. For the rest of the compounds, the temperature evolution of the excess current due to Andreev reflection appears to follows the standard BCS like behavior and disappears at T_c^{bulk}.

Most of these results have been discussed elsewhere [61].

Single crystals of $Ba(Fe_{1-x}Co_x)_2As_2$ are grown out of FeAs flux [62, 63]. We studied x = 0.05, 0.055, 0.07, 0.08. The undoped $BaFe_2As_2$ undergoes a magnetostructural transition at $\sim$ 132 K. Substituting Fe with Co suppresses the onset temperature of both the antiferromagnetic and orthorhombic phases. At close to 3% doping, superconductivity emerges. This superconducting phase coexists with the magnetic phase until $\sim$ 6% doping. Optimal T_c is achieved once the magnetic phase has been completely suppressed and this occurs for $\sim$ 8% doping. With a further increase in Co concentration, T_c starts to decrease, giving rise to the dome shaped superconducting region on the phase diagram (Figure 1.1). Figure 3.1 (a) shows the bulk resistivity curves of $Ba(Fe_{1-x}Co_x)_2As_2$ crystals with different Co doping.

3.1.1 Electron Underdoped $Ba(Fe_{0.95}Co_{0.05})_2As_2$ and $Ba(Fe_{0.945}Co_{0.055})_2As_2$

From the derivative of the bulk resistivity dR/dT, we determine that the $Ba(Fe_{0.95}Co_{0.05})_2As_2$ crystals have the tetragonal to orthorhombic structural

transition T_S at $\sim$ 78 K and the paramagnetic to antiferromagnetic transition T_N at $\sim$ 70 K. Figure 3.1 (b) shows these curves. $-dR/dT$ (red curve) develops a peak and a shoulder corresponding to T_N and T_S making these phase transitions easy to spot [64]. The blue curve shows the corresponding shape of the bulk resistivity. The superconducting transition is fairly broad. T_c^{onset} is 17 K while $T_c^{bulk} = 11.6$ K.

For $Ba(Fe_{0.945}Co_{0.055})_2As_2$, T_S is $\sim$ 75 K and T_N is $\sim$ 63 K. The superconducting transition begins at 17 K and $T_c^{bulk} = 12.5$ K

Metallic junctions are formed on freshly cleaved c-axis crystal surfaces and dI/dV across each junction is measured using a standard four-probe lock-in technique. Junctions are constructed via the soft PCS method, as detailed in [65] and Chapter 2 of this thesis.

Figures 3.2−3.4 present differential conductance curves for $Ba(Fe_{0.95}Co_{0.05})_2As_2$ and $Ba(Fe_{0.945}Co_{0.055})_2As_2$. Figures 3.2 (a) and 3.2 (b) show the dI/dV raw data at the lowest temperatures attained. The Andreev spectra clearly points to the presence of two superconducting gaps, as indicated with arrows in the figure. Figures 3.3 (a) and 3.4 (a) show BTK fits to the normalized data from Figures 3.2 (a) and 3.2 (b), respectively. The dashed blue line is an isotropic s-wave single band BTK fit. While it provides a good fit to the features corresponding to the smaller gap, it cannot account for the features corresponding to the larger gap. A two band BTK approach, shown as the solid red line, is required to accurately describe the experimental data. The parameters in the fit are the two superconducting gaps Δ_1 and Δ_2, the lifetime broadening parameter for these gaps Γ_1 and Γ_2 [47], the transparency of the junction for each gap Z_1 and Z_2, and the weight of the first gap w. (The weight of the second gap becomes $1 - w$). For the best fits, Z_1 and Z_2 are close to each other but

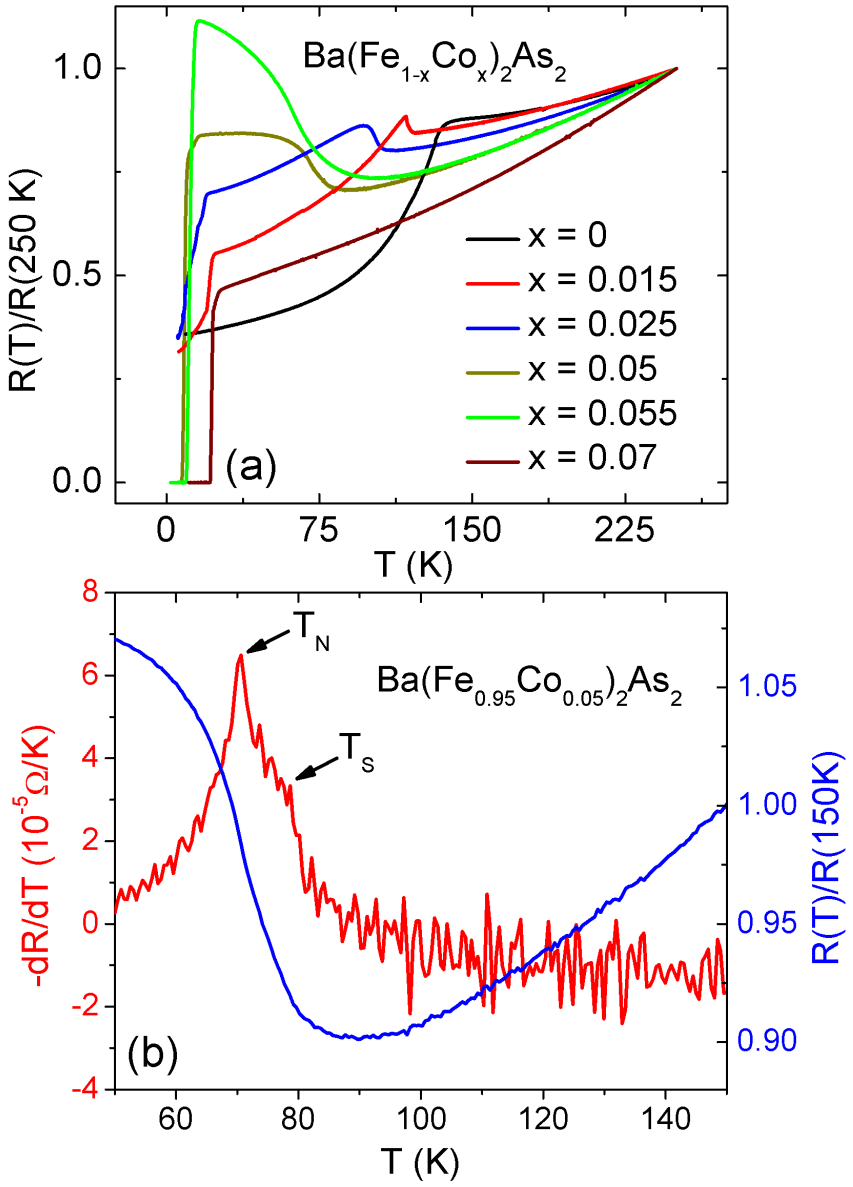

Figure 3.1: (a) Bulk resistivity curves of $Ba(Fe_{1-x}Co_x)_2As_2$ crystals with different Co doping. Increasing Co concentration suppresses the onset temperature of both the antiferromagnetic and orthorhombic phases. (b) The red curve shows $-dR/dT$ for $Ba(Fe_{0.95}Co_{0.05})_2As_2$. It develops a peak and a shoulder corresponding to T_N and T_S making these phase transitions easy to spot. The blue curve shows the corresponding shape of the bulk resistivity.

not identical. This might be due to the different Fermi velocities for the different Fermi surfaces resulting in unequal effective barrier strengths. The ratio Γ/Δ for both gaps is also similar.

The parameters for all our fits are given in Table 3.1. For $Ba(Fe_{0.95}Co_{0.05})_2As_2$ $\Delta_1 = 3.0$ meV and $\Delta_2 = 6.6$ meV, while for $Ba(Fe_{0.945}Co_{0.055})_2As_2$ $\Delta_1 = 4.0$ meV and $\Delta_2 = 7.9$ meV. Figure 3.3 (b) and 3.4 (b) show the raw data dI/dV temperature evolution curves of the Andreev spectra for these two junctions. The dashed black rectangle is highlighting the conductance enhancement that is detected between T_c^{bulk} and T_c^{onset}.

3.1.2 Near Optimal Electron-Doped $Ba(Fe_{0.93}Co_{0.07})_2As_2$ and $Ba(Fe_{0.92}Co_{0.08})_2As_2$

Figures 3.5 shows dI/dV data for $Ba(Fe_{0.93}Co_{0.07})_2As_2$. At this doping, the structural and magnetic transitions have been completely suppressed. T_c^{bulk} = 21.7 K while T_c^{onset} = 23 K. Figure 3.5 (a) shows that a two band BTK model (solid red line) provides a closer fit to the experimental data than does the one band BTK model (dashed blue line). The extracted gap values are $\Delta_1 = 4.0$ meV and $\Delta_2 = 7.0$ meV. Figure 3.5 (b) shows the temperature evolution of the Andreev spectra for this junction. Conductance enhancement is also observed just above T_c^{bulk}, as shown within the black dashed box.

Figures 3.6 shows dI/dV data for $Ba(Fe_{0.92}Co_{0.08})_2As_2$. This was the electron doping that showed us the highest T_c and the sharpest transition; T_c^{bulk} = 24.5 K and T_c^{onset} = 25 K. Figure 3.6 (a) presents a two band BTK fit (solid red line) while Figure 3.6 (b) shows the temperature evolution of the Andreev spectra for this junction. The gap values obtained are $\Delta_1 = 4.99$ meV and $\Delta_2 = 9.95$ meV.

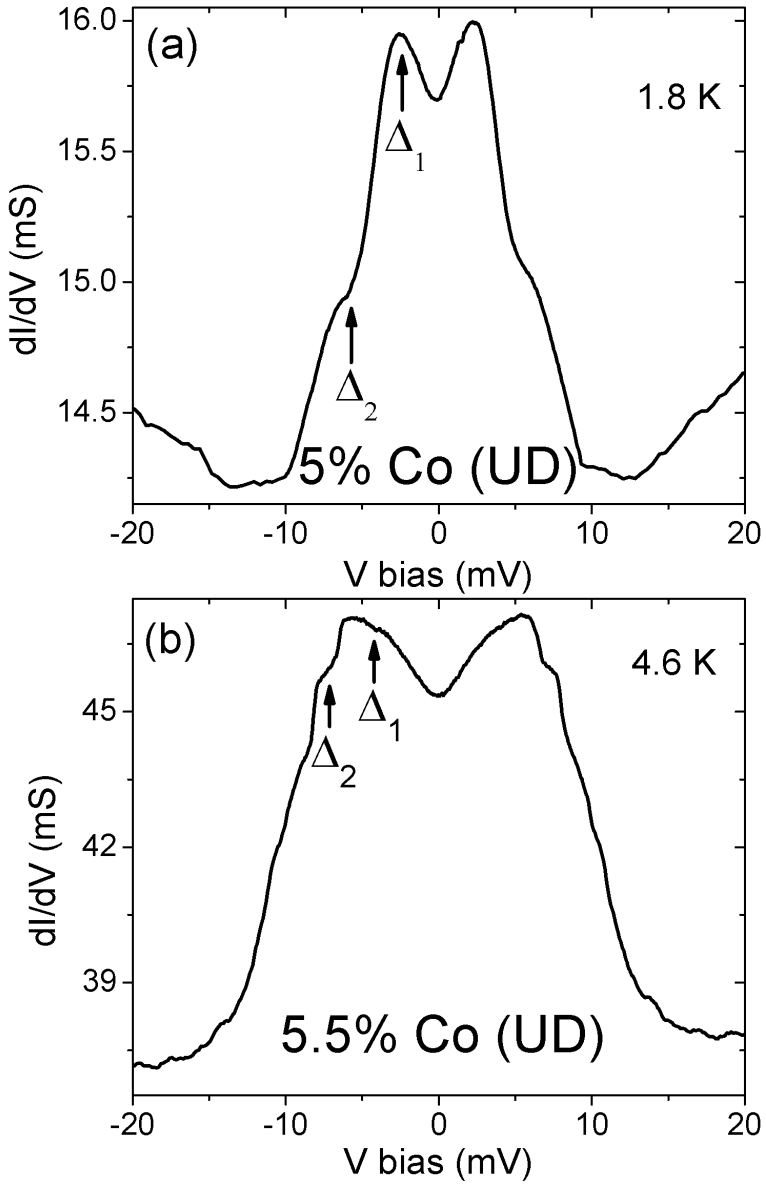

Figure 3.2: Low temperature PCS dI/dV for (a) $Ba(Fe_{0.95}Co_{0.05})_2As_2$ and (b) $Ba(Fe_{0.945}Co_{0.055})_2As_2$. The Andreev reflection spectra are shown, and the arrows point out the features corresponding to the two superconducting gaps.

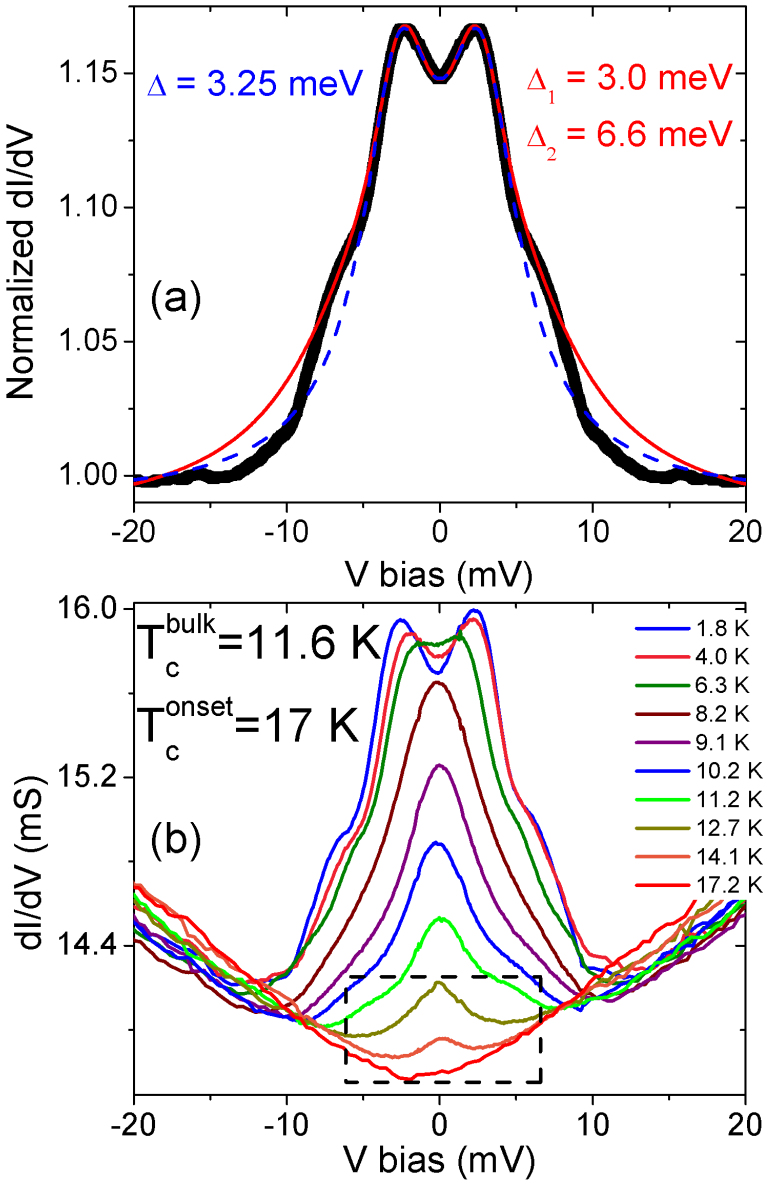

Figure 3.3: (a) The PCS spectra shown in Figure 3.2 (a) for $Ba(Fe_{0.95}Co_{0.05})_2As_2$ has been normalized and fit to one band and two band BTK models. The one band fit (dashed blue line) fails to account for the larger gap. The two band fit (solid red line) is able to track the experimental data better. The gap values obtained are $\Delta_1 = 3.0$ meV and $\Delta_2 = 6.6$ meV. (b) Temperature evolution of the Andreev reflection spectra. The dashed black rectangle points out the dI/dV enhancement that survives above T_c^{bulk}.

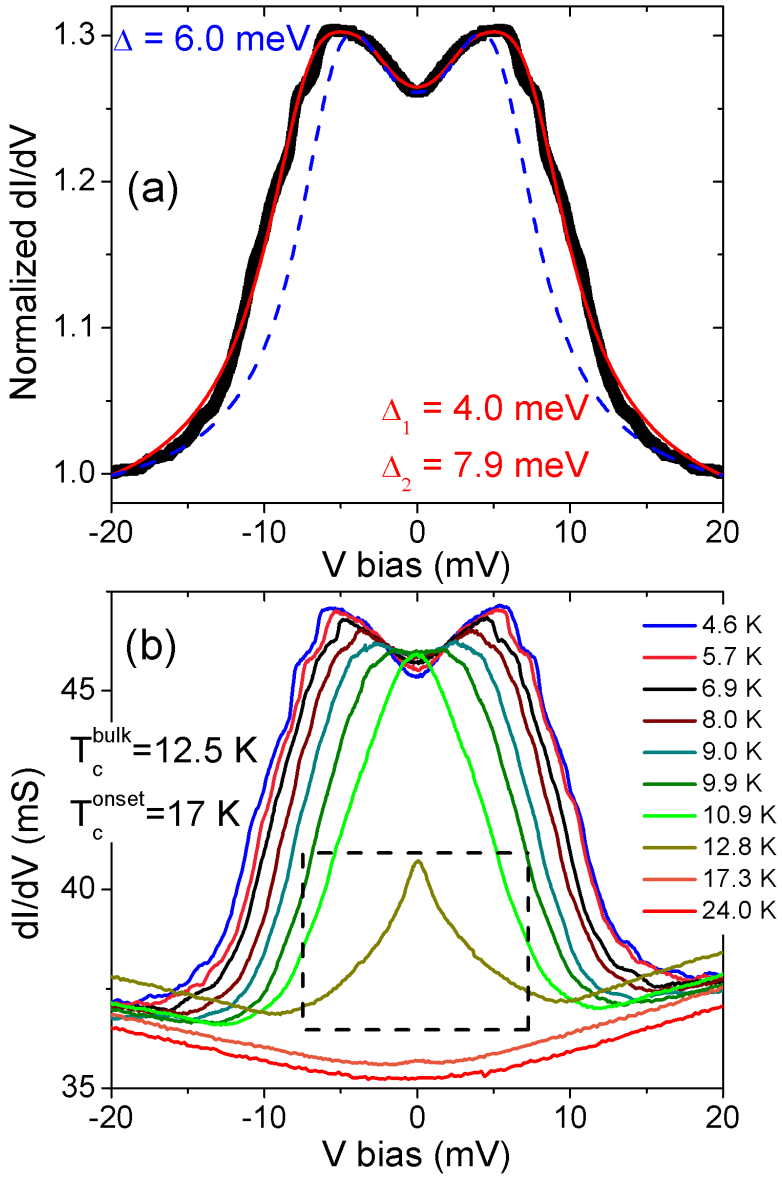

Figure 3.4: (a) The data shown in Figure 3.2 b for $Ba(Fe_{0.945}Co_{0.055})_2As_2$ has been normalized and fit to one band and two band BTK models. Like $Ba(Fe_{0.95}Co_{0.05})_2As_2$, the two band model (solid red line) provides a better fit than the one band model (dashed blue line). The gap values obtained are $\Delta_1 = 4.0$ meV and $\Delta_2 = 7.9$ meV. (b) Temperature evolution of the Andreev reflection spectra. The dashed black rectangle points out the dI/dV enhancement that survives above T_c^{bulk}.

Table 3.1: BTK Fit Parameters For $Ba(Fe_{1-x}Co_x)_2As_2$ & $Ba_{0.8}K_{0.2}Fe_2As_2$

Crystal	Δ_1	Δ_2	Z_1	Z_2	Γ_1/Δ_1	Γ_2/Δ_2	w	T_c^{onset}	T_c^{bulk}	T_S	T_N
$Ba(Fe_{0.95}Co_{0.05})_2As_2$ (e UD)	3.0 meV	6.6 meV	0.395	0.40	0.56	0.62	0.67	17 K	11.6 K	78 K	70 K
$Ba(Fe_{0.945}Co_{0.055})_2As_2$ (e UD)	4.0 meV	7.9 meV	0.31	0.35	0.25	0.30	0.10	17 K	12.5 K	75 K	63 K
$Ba(Fe_{0.93}Co_{0.07})_2As_2$ (e OD)	4.0 meV	7.0 meV	0.28	0.30	0.20	0.15	0.20	23 K	21.7 K	-	-
$Ba(Fe_{0.92}Co_{0.08})_2As_2$ (e OD)	4.99 meV	9.95 meV	0.39	0.435	0.36	0.23	0.50	25 K	24.5 K	-	-
$Ba_{0.8}K_{0.2}Fe_2As_2$ (h UD)	2.2 meV	-	0.373	-	0.18	-	1	26 K	15 K	90 K	90 K
$Ba_{0.8}K_{0.2}Fe_2As_2$ (h UD)	2.7 meV	7.5 meV	0.32	0.45	0.57	0.53	0.37	26 K	15 K	90 K	90 K

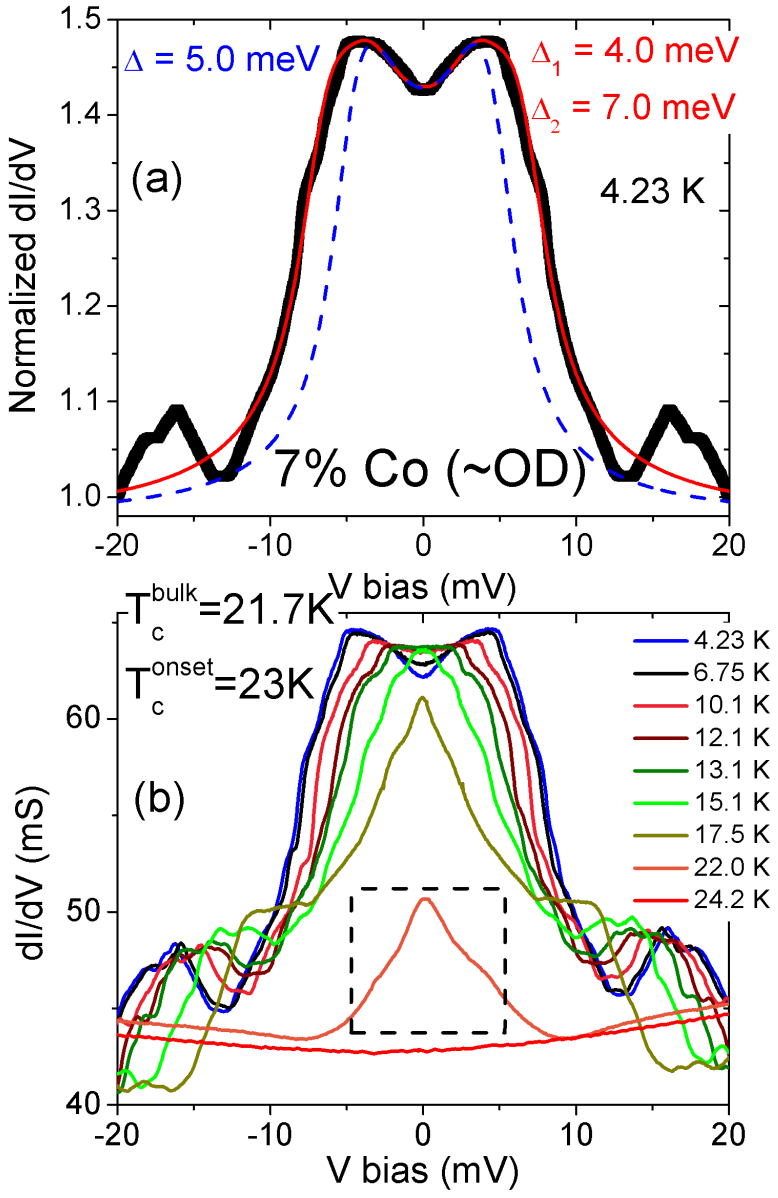

Figure 3.5: (a) Low temperature Andreev reflection spectra for $Ba(Fe_{0.93}Co_{0.07})_2As_2$, normalized, and fit to the one band (dashed blue curve) and two band (solid red curve) BTK models. The two band BTK model provides a much better fit with $\Delta_1 = 4.0$ meV and $\Delta_2 = 7.0$ meV. (b) Temperature evolution of the Andreev reflection spectra. The dashed black rectangle is highlighting the conductance enhancement that is detected between T_c^{bulk} and T_c^{onset}.

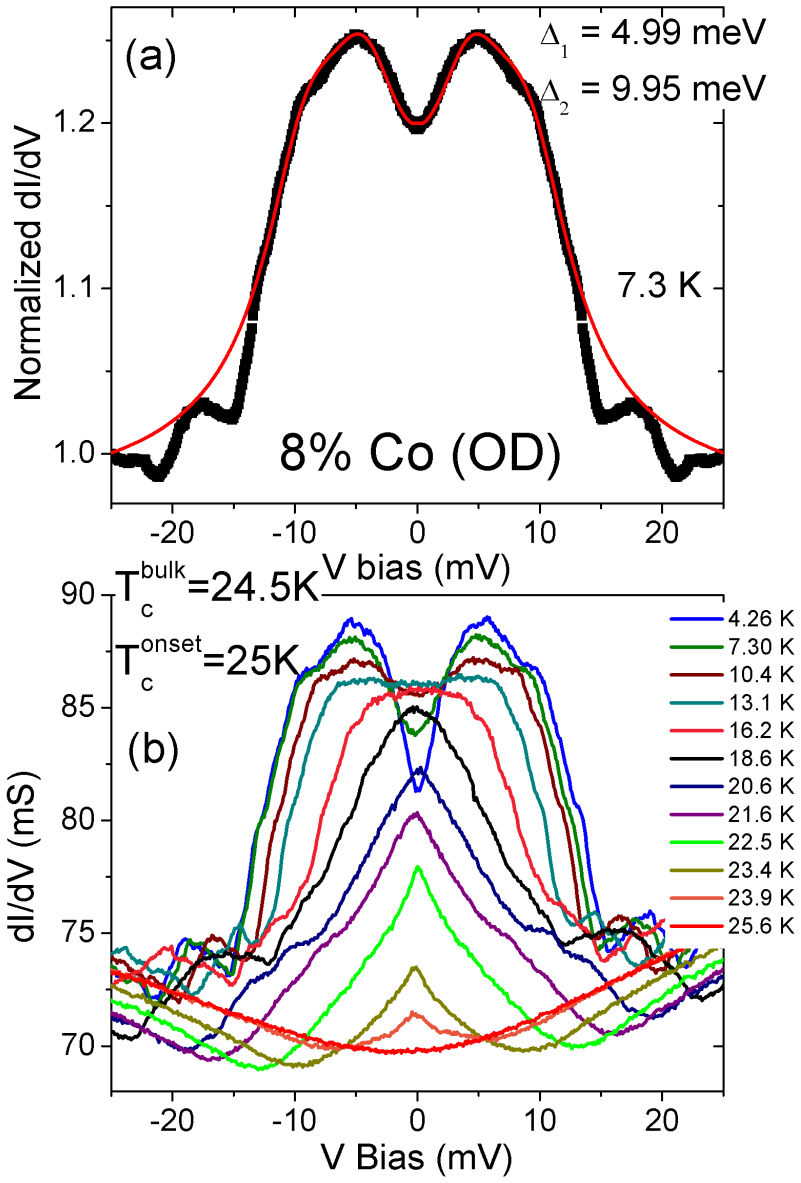

Figure 3.6: (a) Low temperature Andreev reflection spectra for $Ba(Fe_{0.92}Co_{0.08})_2As_2$ has been normalized and fit to the two band BTK model. The fit provides gap values of $\Delta_1 = 4.99$ meV and $\Delta_2 = 9.95$ meV. (b) Temperature evolution of the Andreev reflection spectra.

Table 3.2 shows that for near optimal doped $Ba(Fe_{1-x}Co_x)_2As_2$ our gap values are in good agreement with other PCS experiments [59, 57], scanning tunneling microscopy (STM) data [66], and angle resolved photoemission spectroscopy (ARPES) studies [67]. All experimental techniques show a slight variation ($\pm$ 0.5 meV) in the measured gap size and the table states the average value observed.

Table 3.2: $\overline{\Delta}$ For Near Optimal Doped $Ba(Fe_{1-x}Co_x)_2As_2$ Detected By Other Research Groups

Experimental Technique	$\overline{\Delta_1}$	$\overline{\Delta_2}$
PCS [59]	4.4 meV	9.7 meV
STM [66]	5.0 meV	10.0 meV
ARPES [67]	5.0 meV	7.0 meV

3.1.3 Holed Doped $Ba_{0.8}K_{0.2}Fe_2As_2$

Figure 3.7 show dI/dV for $Ba_{0.8}K_{0.2}Fe_2As_2$. These single crystals are grown in Sn flux [68]. This doping exhibits a coexistence of magnetism and superconductivity with $T_N = T_S \sim 90$ K [69]. The superconducting transition is very broad, with $T_c^{onset} = 26$ K and $T_c^{bulk} = 15$ K. Figure 3.7 (a) shows features corresponding to a single superconducting gap. Figure 3.7 (b) on the other hand shows clear features corresponding to two superconducting gaps. Figure 3.7 (a) is fit to a single band BTK model with gap value $\Delta = 2.2$ meV. The spectra in Figure 3.7 (b) is fit to a two band BTK model with gaps of $\Delta_1 = 2.7$ meV and $\Delta_2 = 7.5$ meV.

As mentioned in Chapter 1 of this thesis, (Figure 1.3), the Fermi surfaces of these compounds are quasi two dimensional sheets with elliptical electron pockets centered at $(0, \pi)$ and $(\pi, 0)$ and near circular hole pockets at the Γ point [33]. For $Ba_{0.6}K_{0.4}Fe_2As_2$, a small energy gap is observed on hole pocket β while nearly equal large energy gaps are found on hole pocket α and

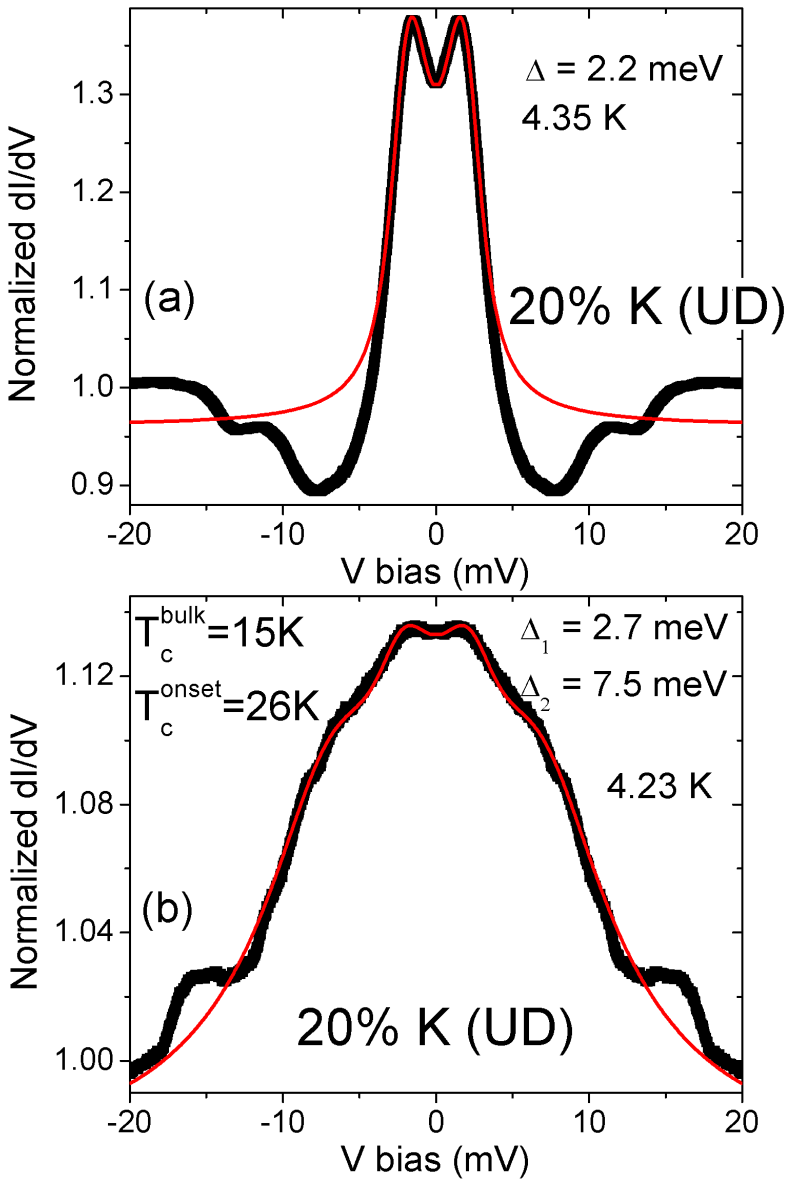

Figure 3.7: (a) Andreev reflection spectra and a single band BTK fit (red line) for PCS performed on $Ba_{0.8}K_{0.2}Fe_2As_2$ ($\Delta = 2.2$ meV). (b) Andreev reflection spectra and a two band BTK fit (red line) for a junction constructed on a different crystal of $Ba_{0.8}K_{0.2}Fe_2As_2$. Both crystals were grown together in the same flux. The gap values derived are $\Delta_1 = 2.7$ meV and $\Delta_2 = 7.5$ meV.

electron pocket γ [70]. However, the Fermi surface of β is 4−6 times larger than that of α and γ. It is plausible that on occasion our point contacts pick up the gap only from β causing our spectra to be a good fit to the single gap BTK model.

All the fits we have shown assume isotropic s-wave superconducting gaps. We have also not included any coupling between the two bands in the multi-gap fits. Extensions to the BTK theory have been proposed to incorporate interference and phase difference between the two superconducting bands [71, 72]. A single band BTK fit has three free parameters (Δ, Z, Γ) while an independent two band BTK fit has seven (Δ_1, Z_1, Γ_1, Δ_2, Z_2, Γ_2, w). The independent two band BTK model is giving quite good fits to the experimental data, albeit the values of the parameters are somewhat degenerate, meaning that equally good fits can be obtained for slightly different values of the fitting parameters. The gap sizes can be influenced within ± 0.5 mV by changing the relative weight of the bands. We have found that adding interference and a phase difference between the bands adds two more free parameters and increase uncertainty in the extracted results without improving fit quality. In the transparent junction (low Z limit) data presented here, the dI/dV spectra predicted by the independent and interfering band models do not differ greatly. The interfering band models would be useful to differentiate between s_{++} and s_{+-} symmetry if the barrier strength Z for the same junction could be varied systematically from the metallic to the tunneling regime. However, this is very hard to achieve experimentally.

3.2 The Excess Current Anomaly

3.2.1 Zero Bias Conductance

In Figure 3.8 we plot the zero bias conductance and bulk resistivity on the same temperature scale for some of our junctions. For underdoped $Ba(Fe_{1-x}Co_x)_2As_2$ [Figure 3.8 (a),(b)], the superconducting transitions are broad and the zero bias conductances of the point contacts start rising near T_c^{onset}. For the near optimally doped sample [Figure 3.8 (c)], the superconducting transition is narrow. For underdoped $Ba_{0.8}K_{0.2}Fe_2As_2$ [Figure 3.8 (d)], the transition is again broad. However, in this case, the zero bias conductance starts to rise closer to T_c^{bulk} as opposed to T_c^{onset}. The temperature at which the zero bias conductance starts to rise is the temperature at which an 'excess current' starts to flow across the junction. In this section, we discuss the excess current of the point contact junctions in detail.

3.2.2 Excess Current

The approximate temperature dependence of the energy gap for weakly coupled s-wave BCS superconductors may be given by $\Delta = \Delta_0 \tanh[1.74 * \sqrt{T_c/T - 1}]$. As the temperature is increased, the Andreev reflection signal decreases with a concomitant increase in the thermal broadening in the dI/dV curves. The gap values extracted by BTK fits develop larger and larger error bars and the smaller gap becomes especially hard to distinguish. Instead of plotting the temperature evolution of the extracted Δ values, we therefore focus on the excess current, I_{exc}, that flows through our point contact junctions due to Andreev reflection. From the BTK theory [46] for s-wave superconductors, I_{exc} has the same

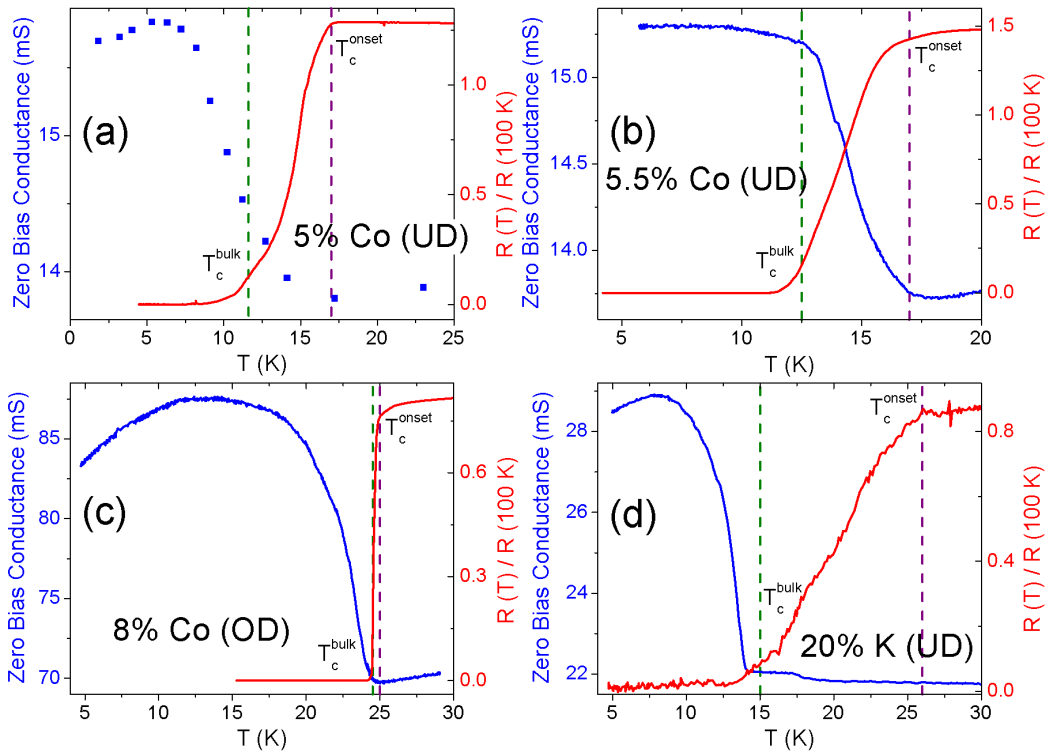

Figure 3.8: Comparison of the zero bias conductance (blue) and bulk resistivity (red) curves. (a, b) For the electron underdoped compound $Ba(Fe_{0.95}Co_{0.05})_2As_2$ and $Ba(Fe_{0.945}Co_{0.055})_2As_2$, the superconducting transitions are wide and the zero bias conductance starts to rise close to T_c^{onset}. (c) For the near optimally doped compound $Ba(Fe_{0.92}Co_{0.08})_2As_2$ the superconducting transition is narrow. (d) For $Ba_{0.8}K_{0.2}Fe_2As_2$, like the electron underdoped compounds, the transition is broad but the zero bias conductance only starts to rise close to T_c^{bulk}. T_c^{onset} and T_c^{bulk} are shown by vertical purple and green dashed lines, respectively.

temperature dependence as Δ ($I_{exc} \propto \Delta/R_{junction}$, where $R_{junction}$ is the resistance of the point contact junction). We calculate I_{exc} by integrating the normalized dI/dV curves over $\pm(\mathrm{V} >> \Delta)$. Details are provided in Section 3.2.3. Figure 3.9 (a) shows I_{exc} vs. T. To compare each doping, we normalize T_c and the low temperature I_{exc} each to 1. We find that the near optimally doped $Ba(Fe_{0.93}Co_{0.07})_2As_2$, $Ba(Fe_{0.92}Co_{0.08})_2As_2$ and hole underdoped $Ba_{0.8}K_{0.2}Fe_2As_2$ crystals show a reasonable agreement with the BCS temperature dependence.

Analysis of the data taken on the electron underdoped $Ba(Fe_{0.95}Co_{0.05})_2As_2$ and $Ba(Fe_{0.945}Co_{0.055})_2As_2$ crystals is more complex. While Andreev spectra on the optimally and hole underdoped crystals exhibit I_{exc} close to T_c^{bulk}, the data on electron underdoped compounds (5% and 5.5% Co doping) exhibit I_{exc} at T_c^{onset}. The superconducting transition for these crystals is broad; 4.5-5 K. In Figure 3.9 (a) the solid black line is the BCS behavior vs. temperature normalized to T_c^{bulk}. Data from $Ba(Fe_{0.945}Co_{0.055})_2As_2$ (purple circles) follows the fit up to T_c^{bulk} after which I_{exc} remains enhanced up to T_c^{onset}. $Ba(Fe_{0.95}Co_{0.05})_2As_2$ (red squares) follows a similar trend.

Microscopic variations in the Co doping may be used to explain why the electron underdoped $Ba(Fe_{1-x}Co_x)_2As_2$ crystals show I_{exc} above their bulk T_c. Our soft PCS junctions are comprised of multiple point contacts and the conductivity from each adds to give the measured I_{exc}. We assume a Gaussian distribution function for the local T_c's of the point contacts centered at T_c^{bulk} (details in Section 3.2.4) and calculate the resulting I_{exc} [Figure 3.9 (b)]. The simulated curve (dashed blue line) reproduces the experimentally observed I_{exc} above T_c^{bulk} quite well. The solid lines are those calculated for multiple point contacts (with different T_c values) whose weighted sum gives the total I_{exc}.

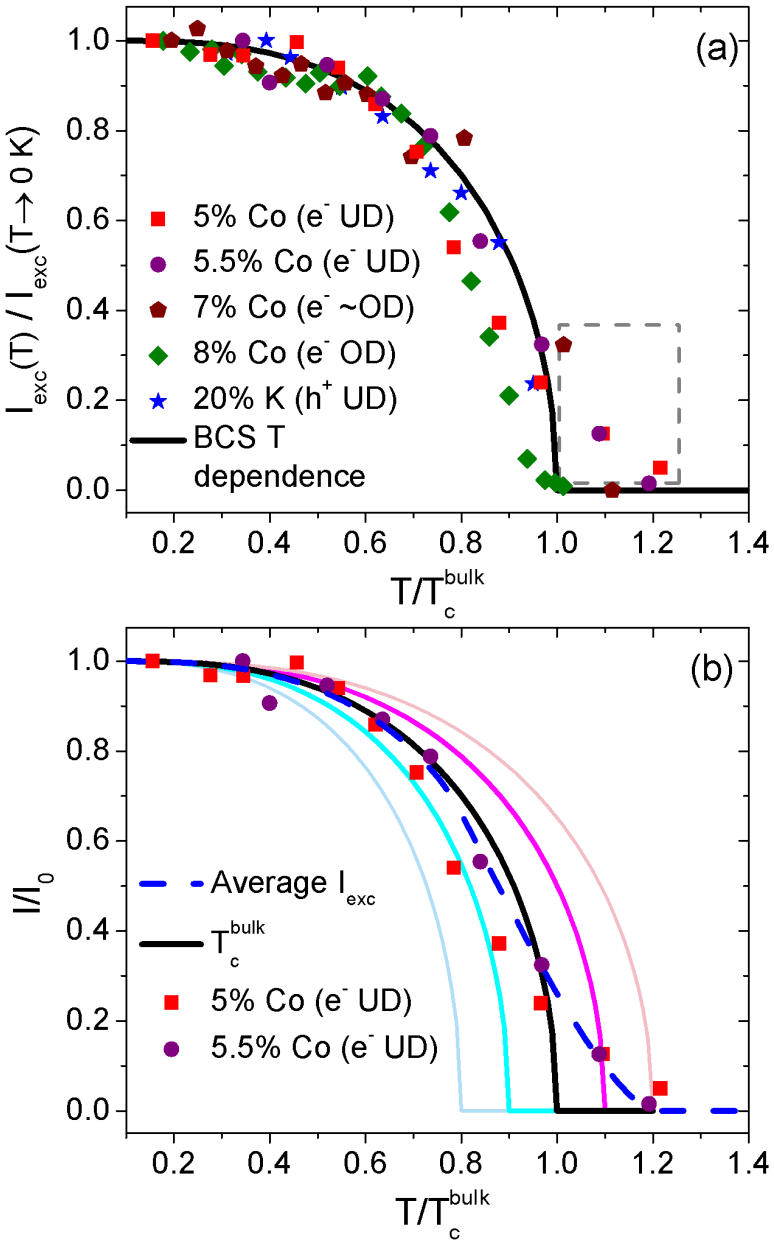

Figure 3.9: (a) The temperature evolution of the excess current, I_{exc}, for all crystals measured with the temperature normalized to T_c^{bulk} and the I_{exc} normalized to its value at the lowest temperatures measured. The solid black line is the dependence for a weakly coupled s-wave BCS superconductor. Reasonable fits are obtained for all but the electron underdoped compounds. For those, I_{exc} follows the BCS dependence at low temperatures, but at higher temperatures, a tail extending to higher $T > T_c^{bulk}$ is seen. The dashed gray rectangle is highlighting this anomaly. (b) The dashed blue line is I_{exc} calculated by assuming that the junction is comprised of multiple point contacts in parallel, with microscopic inhomogeneities in the Co doping. This gives rise to a Gaussian distribution of all the local T_c's centered at T_c^{bulk}.

An alternate explanation is that this enhancement above bulk T_c is due to a novel scattering mechanism. Such scenarios have previously been reported in $FeTe_{0.55}Se_{0.45}$ (spin fluctuations) [73] and $Ba(Fe_{1-x}Co_x)_2As_2$ (phase-incoherent superconducting pairs) [74].

Chapter 4 of this thesis discusses point contact spectra in the normal state of the iron based superconductors. We find that underdoped $Ba(Fe_{1-x}Co_x)_2As_2$ crystals show a conductance enhancement in their normal state, well above the magnetostructural transition temperatures (T_S, T_N). This enhancement is being caused by orbital fluctuations [65, 75]. Underdoped $Ba_{0.8}K_{0.2}Fe_2As_2$ crystals do not show any enhancement above their T_S, T_N. Optimally doped $Ba(Fe_{1-x}Co_x)_2As_2$ do not have a magnetostructural transition and do not show any conductance enhancement in their normal state.

It is worth noticing that compounds exhibiting orbital fluctuations in their normal state are the same ones that show I_{exc} above T_c^{bulk}, and the compounds whose I_{exc} disappears at T_c^{bulk} do not show anything anomalous in their normal state. It could be conjectured that the underlying physics behind the anomalous behavior above T_c^{bulk} and the anomalous behavior above T_S, T_N might be related since the same crystal dopings show them.

3.2.3 Excess Current Calculation

Andreev reflection causes an increase in the current transmitted across a normal metal-superconductor point contact junction. I_{exc} is defined as the extra current that flows through the junction when compared with its non-superconducting state. To calculate this current we use the equation:

$$I_{exc}(T) = \int_{-V<<-\Delta}^{V>>\Delta} \frac{dI}{dV}(T)\mathrm{d}V - \int_{-V<<-\Delta}^{V>>\Delta} \frac{dI}{dV}(T \geq T_c^{onset})\mathrm{d}V \qquad (3.1)$$

We illustrate how this integration is performed for $Ba(Fe_{0.95}Co_{0.05})_2As_2$ in Figure 3.10.

Figure 3.10 (a) shows the raw dI/dV curves taken at 1.8 K (blue, lowest temperature attained for this junction) and 17.2 K (red, $\sim T_c^{onset}$). Figure 3.10 (b) shows the same curves after they has been symmetrized and normalized with the curve at 17.2 K. Symmetrization is carried out by taking the average of the dI/dV values at positive and negative biases.

The next step is to integrate the area under the curves and subtract the integral of the current at 17 K from that of 1.8 K. We choose the integration limit to be from -20mV to +20mV since at biases higher than that, Andreev reflection dies out and the two dI/dV curves are nearly identical. The gray shaded area in Figure 3.10 (b) represents the final I_{exc} that we obtain.

This same procedure is repeated for all our crystals at various temperatures. Figure 3.9 (a) is obtained by combining all of the I_{exc} data points calculated this way.

3.2.4 Inhomogeneous Doping Model

Our basic assumption is that our point contact junction is comprised of multiple channels and there is slight variation in the local T_c values of these channels. Most of the channels start showing Andreev reflection at T_c^{bulk} but some of them exhibit Andreev reflection above T_c^{bulk} while other do not exhibit Andreev reflection until below T_c^{bulk}. We define a variable T_c^{local} and

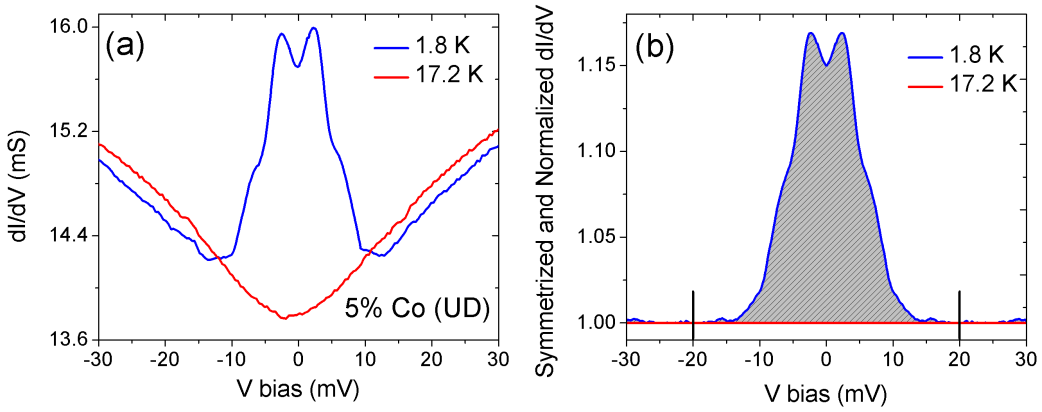

Figure 3.10: (a) Raw dI/dV curves taken on $Ba(Fe_{0.95}Co_{0.05})_2As_2$ at 1.8 K (blue) and 17.2 K (red). (b) The same curves after they have been symmetrized and normalized to dI/dV at 17.2 K. I_{exc} is represented by the shaded gray area on the plot. It is calculated by integrating the area under the curves and subtracting the value at 17.2 K from the value at 1.8 K. The integration limits are set at ± 20 mV, represented by the short vertical black lines. At biases higher than 20 mV the two dI/dV curves are nearly identical.

set its limits to be 0.8-1.2 T_c^{bulk}. A ±20% varaition in T_c^{bulk} captures the experimental data points very well.

We have tried various distribution functions for T_c^{local}. Figure 3.11 (b) shows the number of channels (or point contacts) sampled for a given T_c for Gaussian and Linear distribution functions. The Gaussian distribution function is $e^{-\frac{1}{2}(\frac{T_c^{local}-T_c^{bulk}}{\sigma})^2}$ where σ is the standard deviation, which we set as 5% T_c^{bulk}. The largest number of channels superconduct at T_c^{bulk} and as T_c^{local} deviates more and more from T_c^{bulk}, the number of channels with that T_c falls.

I_{exc} is calculated by summing up the excess current due to all the Andreev reflection channels. Figure 3.9 (b) uses the Gaussian distribution function to calculate I_{exc}. In Figure 3.11 (a), we compare I_{exc} from the Gaussian and linear distribution functions with BCS I_{exc}. The general feature is that the I_{exc} for for either of the distribution functions develops a tail above T_c^{bulk}.

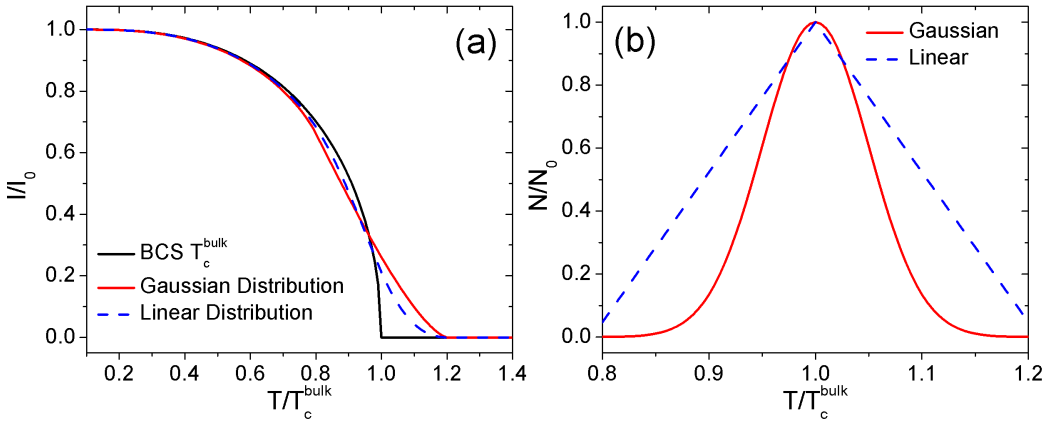

Figure 3.11: (a) Comparing the I_{exc} calculated from Gaussian and linear distribution functions with BCS I_{exc}. The distribution function I_{exc} develops a tail above T_c^{bulk}. (b) The number of channels with a given T_c for the Gaussian ($\sigma = 5\%\ T_c^{bulk}$) and the Linear distribution functions.

To conclude, we have presented Andreev reflection PCS dI/dV data for $Ba(Fe_{1-x}Co_x)_2As_2$ (x = 0.05, 0.055, 0.07, 0.08) and $Ba_{0.8}K_{0.2}Fe_2As_2$. All junctions are made along the c-axis. Our spectra provide clear evidence for multiple, nodeless, s-wave superconducting gaps. The values of the two gaps may be extracted by using the independent multiband BTK model. Apart from underdoped $Ba(Fe_{1-x}Co_x)_2As_2$, the temperature evolution of the excess current for the crystals is well described by the BCS temperature dependence. The excess current for underdoped $Ba(Fe_{1-x}Co_x)_2As_2$ exhibits excess conductance at higher temperatures that survives above the bulk T_c. The shape of I_{exc} vs. T can be simulated assuming microscopic inhomogeneity of the Co doping in the crystals.

3.3 Isoelectronic Substituted $BaFe_2(As_{1-x}P_x)_2$

Superconductivity may be induced in the 122 compounds by the substitution of As with P. This doping does not change the electron/hole concentration but rather works through chemical pressure due to the different ion sizes of

As and P [76]. Chemical pressure causes structural distortions similar to those obtained by applying physical pressure.

Optimal T_c is 30 K and is achieved for $\sim 32\%$ P doping. Evidence for nodes on the superconducting gap is provided by thermal conductivity [77], magnetic penetration depth [78], and nuclear magnetic resonance measurements [79]. Angle resolved photoemission spectroscopy studies have been carried out to detect the location of these nodes. Shimojima et al. [80] observe three fully gapped hole Fermi surfaces at the zone center and speculate that the line nodes probably exist on the electron pockets at the zone corners. On the other hand, Zhang et al. [81] find these corner electron pockets to be fully gapped and instead observe a line node on one of the center hole pockets.

3.3.1 Over-substituted $BaFe_2(As_{0.57}P_{0.43})_2$

We perform PCS experiments on $BaFe_2(As_{0.57}P_{0.43})_2$. They are grown as described in [82, 83]. At 43% P substitution, the crystal is over-substituted and superconducts at $T_c \sim 25$ K.

Andreev spectra from three separate junctions, J1-J3, constructed on the c-axis of $BaFe_2(As_{0.57}P_{0.43})_2$ is presented in Figure 3.12. The raw data for J1 shows clear two gap behavior; the arrows in Figure 3.12 (a) point out the features corresponding to the gaps. Figure 3.12 (b) shows that data normalized and fit to both the one and two band BTK models. Figure 3.12 (c) and (d) show the spectra for the other two junctions, J2 and J3, respectively.

For J1 and J3, the two band BTK model provides better fits (solid red curves) than the one band model (dashed blue curves). The gap values are $\Delta_1 = 2.9$ meV and $\Delta_2 = 6.9$ meV for J1; and $\Delta_1 = 3.0$ meV and $\Delta_2 = 6.9$

meV for J3. Note the single gap BTK model with $\Delta = 2.8$ meV (dashed blue curve) is sufficient to describe J2. The parameters for these fits are given in Table 3.3.

In an s-wave superconductor with nodes, calculations based on the extended BTK theory predict a maximum at zero bias voltage when the PCS conductance is measured in the direction of the gap node (Figure 3.13, based on Figure 2 (a) of [57]). The top panel in Figure 3.13 shows simulated curves without any smearing ($\Gamma = 0$) while the bottom panel shows simulated curves for $\Gamma = \Delta/4$. The inset shows how the magnitude of the gap size varies in space and the black arrow points out the direction of the current injected by the point contact junction.

Our data do not show such a feature, but to definitively discount the presence of a node on the superconducting gap, point contact junctions need to be constructed on the a-b plane of the crystal. The crystals are exceedingly thin, less than 50μm on their sides, making such a measurement very challenging.

We are not certain which Fermi surfaces our detected gaps of ~ 3 and 7 meV correspond to. That only the smaller gap is detected in J2 suggests that the Fermi surface corresponding to the smaller gap couples better to c-axis transport.

3.3.2 Under-substituted $BaFe_2(As_{0.76}P_{0.24})_2$

We also look at crystals of under-substituted $BaFe_2(As_{0.76}P_{0.24})_2$ ($T_N \sim 70$ K, $T_c \sim 16$ K [83]). Figure 3.14 presents the Andreev spectra obtained on these crystals. The junction in Figure 3.14 (a) is fit to a single, isotropic

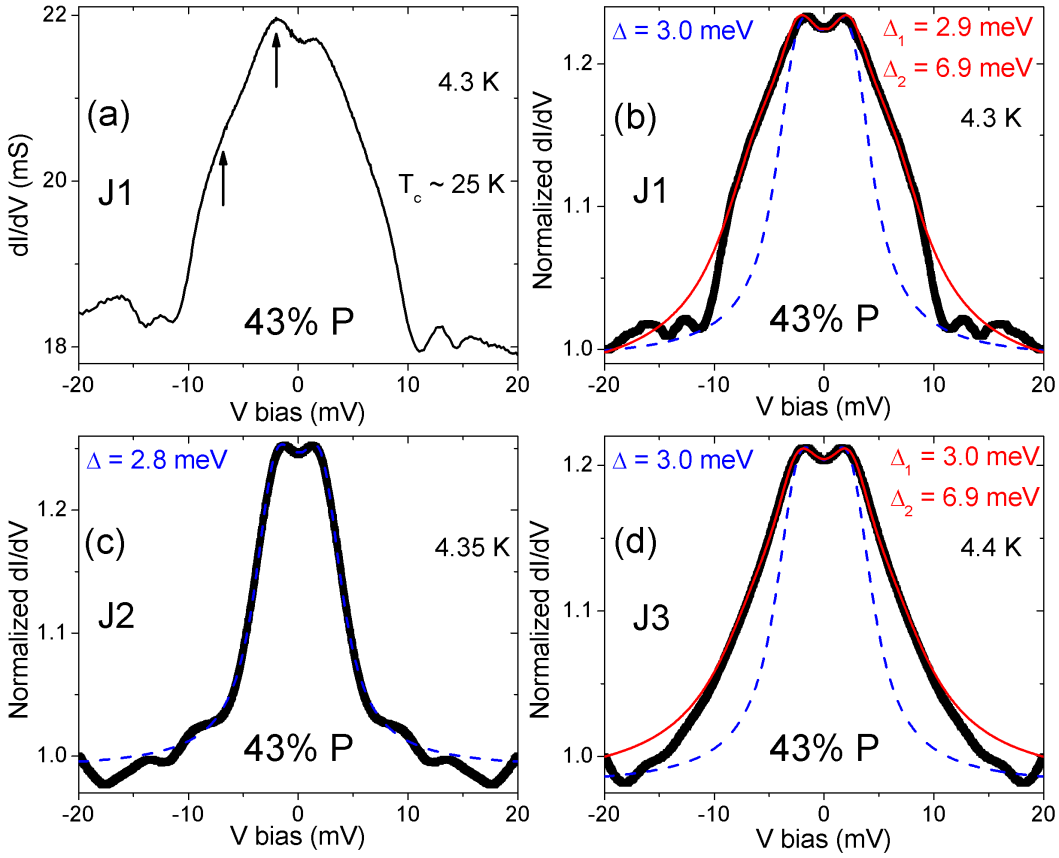

Figure 3.12: Andreev spectra for three different junctions J1, J2, and J3 on $BaFe_2(As_{0.57}P_{0.43})_2$. (a) Raw dI/dV data for J1: the arrows point out the features corresponding to the two gaps. (b) One band (dashed blue curve) and two band (solid red curve) BTK fits on the normalized data for J1. The two band model with $\Delta_1 = 2.9$ meV and $\Delta_2 = 6.9$ meV is better at reproducing the experimental data. (c) For J2, the one band BTK fit (dashed blue curve) with $\Delta = 2.8$ meV is sufficient to describe the data. (d) Like J1, J3 is also described better with the two band BTK model (solid red curve, $\Delta_1 = 3.0$ meV and $\Delta_2 = 6.9$ meV) as opposed to the single band BTK model (dashed blue curve).

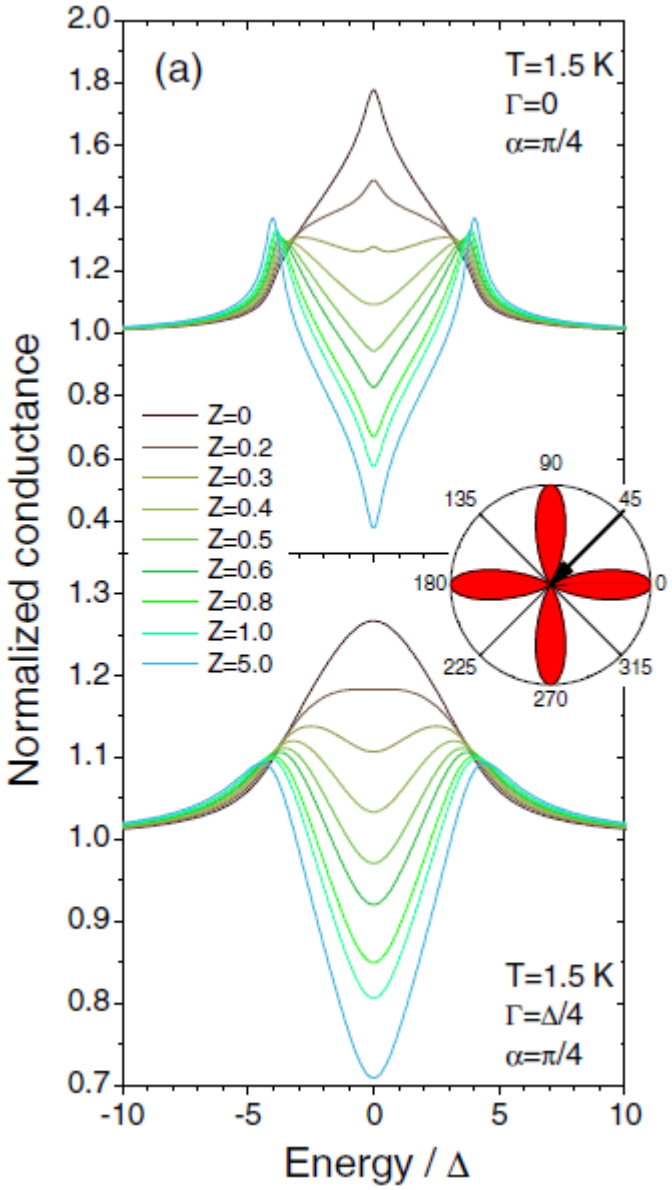

Figure 3.13: Simulated PCS spectra for a nodal s-wave gap where the current is injected along the direction of the node. The inset shows the gap symmetry while the black arrow points out the direction of the injected current. The top panel shows simulated curves without any smearing ($\Gamma = 0$) while the bottom panel shows simulated curves for $\Gamma = \Delta/4$. From [57].

Table 3.3: BTK Fit Parameters For $BaFe_2(As_{1-x}P_x)_2$

Doping	Δ_1, Δ_2 meV	Z_1, Z_2	Γ_1/Δ_1, Γ_2/Δ_2	w_1, w_2
43% P, Fig. 3.12 (b)	2.9, 6.9	0.35, 0.35	0.428, 0.428	0.4, 0.6
43% P, Fig. 3.12 (c)	2.8, -	0.335, -	0.446, -	1, 0
43% P, Fig. 3.12 (d)	3.0, 6.9	0.35, 0.35	0.483, 0.507	0.5, 0.5
24% P, Fig. 3.14 (a)	3.5, -	0.415, -	0.586, -	1, 0
24% P, Fig. 3.14 (b)	5.0, 8.0	0.2, 0.45	0.04, 0.05	0.03, 0.03

s-wave gap of magnitude 3.5 meV. The parameters for the fits are given in Table 3.3.

Most of our junctions on these crystals show very weak Andreev reflection signals. The junction in Figure 3.14 (b) exhibits a conductance enhancement of less than 3%. To fit it, we assume that, along with N-S transport channels, our junction also has parallel N-N transport channels. Part of the contact could be non-superconducting due to the contamination of the crystal surface on exposure to air. An alternate explanation is that since the crystal is underdoped, its full volume is not superconducting, giving rise to parallel N-S and N-N channels. There could also be inhomogeneous doping effects as disucussed in Section 3.2.

Our measured conductance may be described by the equation:

$$\frac{dI}{dV}_{total} = w * \frac{dI}{dV}_{superconducting} + \frac{dI}{dV}_{non-superconducting} \tag{3.2}$$

where we assume the non-superconducting term to be constant for all bias voltage.

The fit shown in Figure 3.14 (b) provides gap values of $\Delta_1 = 5.0$ meV and $\Delta_2 = 8.0$ meV if we set w = 0.06, meaning that only 6% of the transport channels are N-S, with the rest being N-N. The value of w was chosen to minimize Γ while maintaining a good fit.

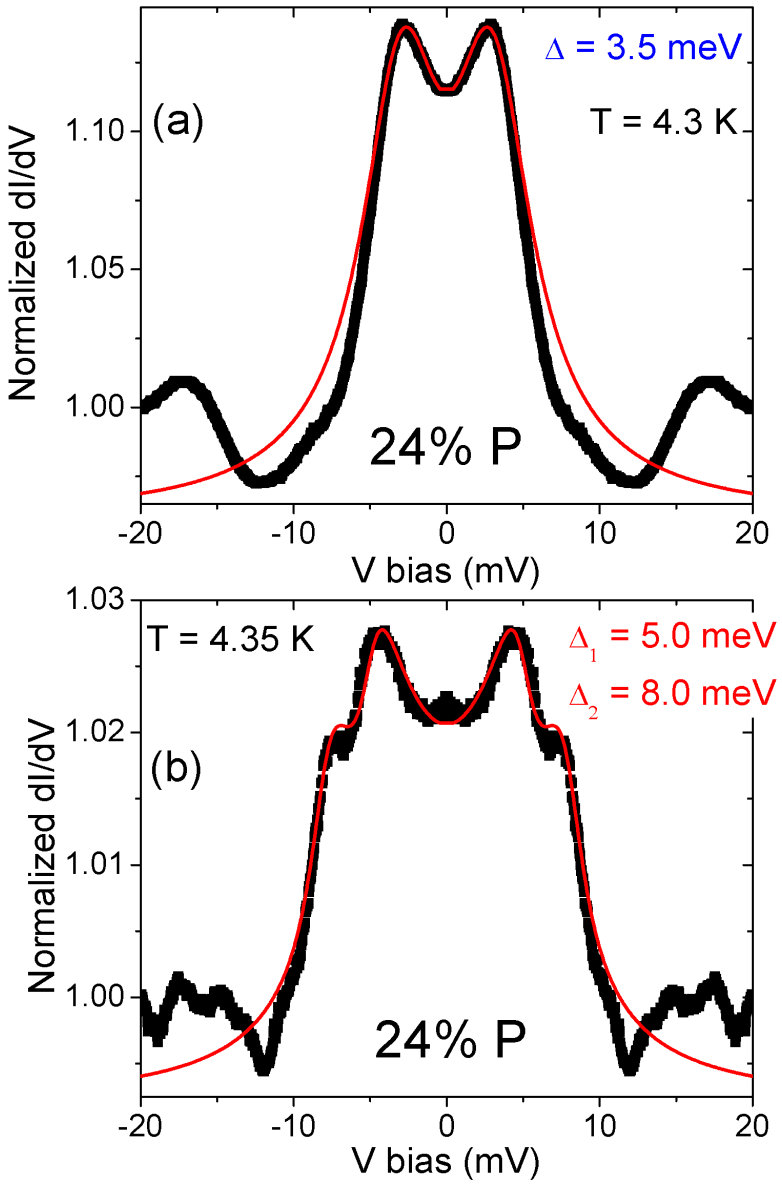

Figure 3.14: Andreev spectra for $BaFe_2(As_{0.76}P_{0.24})_2$. (a) dI/dV data is fit to a single, isotropic s-wave gap of magnitude 3.5 meV. (b) The Andreev signal is very weak, with an enhancement of less than 3%. A two gap BTK fit is done assuming that only 6% of the transport channels in the point contact junction are N-S, with the rest being N-N. The obtained gap values are $\Delta_1 = 5.0$ meV and $\Delta_2 = 8.0$ meV.

To conclude, $BaFe_2(As_{1-x}P_x)_2$ crystals have proven to be very challenging to work with. For 43% P substitution, our c-axis point contact junctions do not show evidence for a node in the superconducting order parameter. In-plane junctions might detect nodes but the small crystal size has precluded us from making such junctions. For 24% P substitution, most of our junctions show only small Andreev enhancements leading us to propose that N-N transport channels exist in parallel with N-S transport channels in our junctions.

3.4 $NaFe_{1-x}Co_xAs$

In addition to the Ba122 family, we also study the Na111 family of the iron based superconductors. NaFeAs has a metallic antiferromagnetic ground state. Bulk superconductivity is achieved upon Co doping on the Fe site [18]. We study underdoped $NaFe_{0.98}Co_{0.02}As$ ($T_c \sim 22.5$ K) and overdoped $NaFe_{0.94}Co_{0.06}As$ ($T_c \sim 20.2$ K).

Na111 crystals are 100-150μm in size and quite brittle. Handling them with tweezers often causes them to crumble. These factors, along with their reactiveness in air, makes obtaining good Andreev reflection spectra from them very challenging.

Figure 3.15 shows the characteristic Andreev spectra we obtain on these crystals. Features corresponding to two superconducting gaps are observed, the arrows in the figures are pointing them out. The BTK fits are done for two isotropic s-wave gaps. For the 2% Co doped sample, $\Delta_1 = 5.0$ meV and $\Delta_2 = 9.0$ meV. For the 6% Co doped samples, the Andreev enhancement is small, and it is likely that along with N-S transport channels, our junction also has N-N transport channels. Using Equation 3.2 with w=0.28, we obtain

$\Delta_1 = 4.95$ meV and $\Delta_2 = 6.90$ meV. The value of w was chosen to minimize Γ while maintaining a good fit. The parameters for the fits are given in Table 3.4. ARPES detects nearly isotropic s-wave gaps on these crystals with values comparable to what we obtain [84].

Table 3.4: BTK Fit Parameters For $NaFe_{1-x}Co_xAs$

Doping	Δ_1, Δ_2 meV	Z_1, Z_2	Γ_1/Δ_1, Γ_2/Δ_2	w_1, w_2
2% Co, Fig. 3.15 (a)	5.0, 9.0	0.43, 0.5	0.76, 0.7	0.4, 0.6
6% Co, Fig. 3.15 (b)	4.95, 6.90	0.1, 1.5	0.12, 0.49	0.14, 0.14

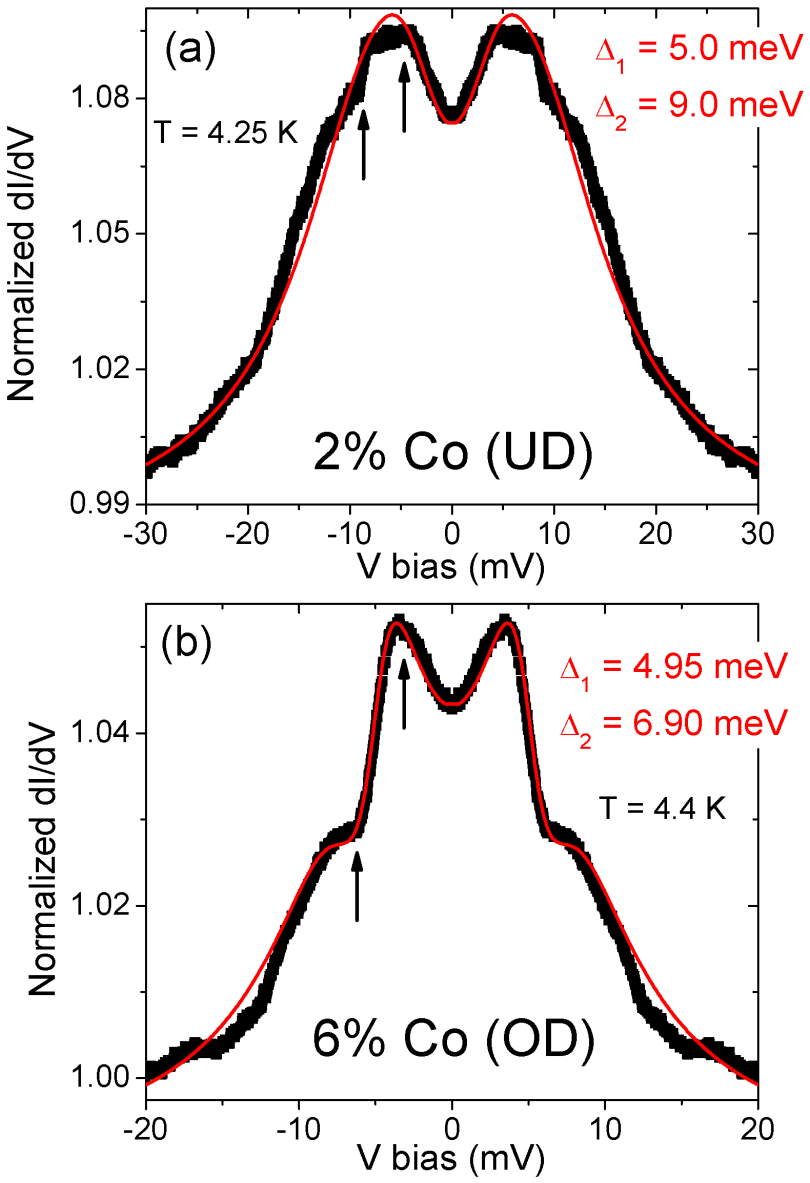

Figure 3.15: Andreev reflection spectra for $NaFe_{1-x}Co_xAs$. Features corresponding to two superconducting gaps are observed, the arrows in the figures are pointing them out. BTK fits are done for two isotropic s-wave gaps. (a) For 2% Co doped sample, $\Delta_1 = 5.0$ meV and $\Delta_2 = 9.0$ meV. (b) For the 6% Co doped samples, the Andreev enhancement is small, and it is likely that along with N-S transport channels, the junction also has N-N transport channels. Using Equation 3.2 with w=0.28, we obtain $\Delta_1 = 4.95$ meV and $\Delta_2 = 6.90$ meV.

CHAPTER 4

PCS ON THE IRON BASED SUPERCONDUCTORS IN THEIR NORMAL STATE

In the previous chapter we discussed in detail how we use point contact spectroscopy (PCS) to probe the superconducting properties of the iron based superconductors. PCS is also sensitive to the normal state properties of certain compounds. Recent work has shown that dI/dV measured across PCS junctions detects a density of states arising from strong electron correlations. For the heavy fermion compound $CeCoIn_5$, the onset of the Kondo lattice appears as a Fano line shape in the PCS spectra [42]. PCS is also sensitive to the hybridization gap and Fano resonance in the heavy fermion URu_2Si_2 [43]. Orbital hybridization and inter-ion correlations effects in the Kondo insulator SmB_6 are also detected by PCS [85]. PCS has also been shown to be sensitive to the incommensurate spin density wave in Chromium [86] and charge density wave in Nb_3Sn [87].

This chapter discusses how PCS detects orbital fluctuations and density of states effects in the normal state of the iron based superconductors. Most of the data in this chapter has been published as a paper [65].

4.1 Electron and Hole Doped $BaFe_2As_2$

The low temperature ground state of the parent compounds of the iron based superconductors is an antiferromagnetic spin density wave metal with an orthorhombic or monoclinic crystal lattice. Above the magnetostructural tran-

sition ($T_N \approx T_S$), they are paramagnetic metals with a tetragonal crystal lattice [21, 22]. It is not clear if this transition is driven by magnetic fluctuations [23, 24] or orbital ordering fluctuations [25, 26, 27, 28]. A suppression of this antiferromagnetic state by various means corresponds to the emergence of superconductivity [30]. In certain families of these iron based compounds, superconductivity and antiferromagnetism coexist. There is evidence that the quantum critical fluctuations associated with the magnetostructural transition are nematic in character and extend in to the normal state of these compounds [88, 89]. An electron nematic phase here is defined as an electronic state that breaks the C_4 symmetry of the underlying lattice. We show that PCS is sensitive to these nematic electron phases. We start of by discussing the PCS dI/dV spectra observed on $BaFe_2As_2$, $Ba(Fe_{1-x}Co_x)_2As_2$ (electron doping) and $Ba_{1-x}K_xFe_2As_2$ (hole doping).

4.1.1 Undoped $BaFe_2As_2$

Single crystals of $Ba(Fe_{1-x}Co_x)_2As_2$ are grown out of FeAs flux as described in [62, 63](for x = 0 to 0.08) and [64] (for x = 0.085 to 0.125). The undoped $BaFe_2As_2$ undergoes a magnetostructural transition at ~ 132 K. Metallic soft point contact junctions are formed on freshly cleaved c-axis crystal surfaces and dI/dV across each junction is measured using a standard four-probe lock-in technique.

Figure 4.1 (a) shows PCS dI/dV for $BaFe_2As_2$. At the lowest temperature (blue curve), we see a dip at zero bias and two asymmetric conductance peaks at ~ 65 mV. This double peak feature is superimposed on a parabolic background. (For point contacts on normal metals, at high biases the conductance is slightly downward sloping due to scattering off of non-equilibrium phonons

[40]. The background observed over here is the opposite.) As the temperature is increased, the dip at zero bias fills, the conductance peaks move inward, and the bias voltage range of the conductance enhancement decreases. No dramatic change in the spectra is observed as T_S is crossed (red curve). The enhancement eventually disappears leaving behind the parabolic background at 177 K, more than 40 K above T_S. We define T_o as the temperature below which the conductance enhancement is observed. Similar spectra [Figure 4.4 (a), (b)] are obtained from two other underdoped non-superconducting samples: x = 0.015 ($T_S \sim 119$ K, $T_o \sim 165$ K); and x = 0.025 ($T_S \sim 107$ K, $T_o \sim 160$ K). For the underdoped crystals $T_N < T_S$ while for the undoped crystal $T_N = T_S$.

4.1.2 Co underdoped $BaFe_2As_2$

Figure 4.1 (b) shows dI/dV for x = 0.05, where at low temperatures long-rage magnetic order coexists with superconductivity ($T_c^{onset} = 17$ K, $T_S \sim 78$ K, $T_N \sim 70$ K). At 1.8 K, the lower bias voltages (< 15 mV) are dominated by Andreev reflection (Figure 4.1 (b) right inset). However, just like the parent compound, two conductance peaks occur at ~ 65 mV. Above the onset temperature of the superconducting transition, Andreev reflection completely disappears and the high bias conductance evolves just like it does for $BaFe_2As_2$. Figure 4.2 (a) shows dI/dV for another coexisting sample x = 0.055 ($T_c^{onset} = 17$ K, $T_S \sim 75$ K, $T_N \sim 63$ K) depicting the same features. The split Andreev peaks at low temperature attest to the transparency of our junction. The high-bias conductance features are completely reproducible, and are not heating artifacts, as we discuss in Chapter 5 of this thesis.

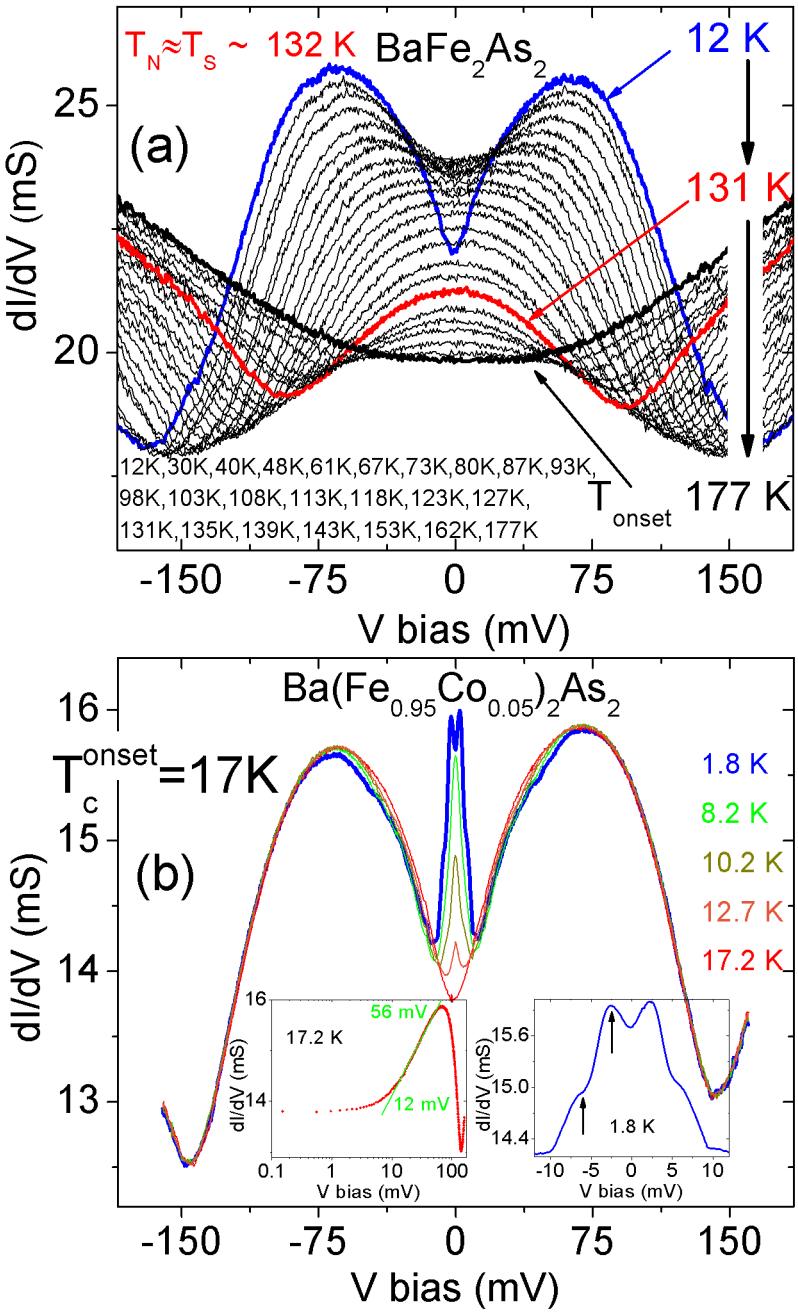

Figure 4.1: (a) dI/dV for $BaFe_2As_2$. Conductance enhancement with peaks at $\sim$ 65mV are observed at low temperature. The enhancement survives well above T_S (red curve). (b) Underdoped 5% Co shows clear Andreev peaks at low temperature (right inset), along with a high bias conductance enhancement like the one seen in the parent compound $BaFe_2As_2$. This enhancement increases logarithmically near zero bias (left inset), meaning it is unlikely to be due to a spin density wave gap (discussed in Section 4.4).

4.1.3 Co overdoped $BaFe_2As_2$

Figure 4.2 (b) shows PCS dI/dV for an overdoped sample with x = 0.125 (T_c^{onset} = 16 K, no T_S). At 4.5 K, superconducting Andreev peaks are observed (Figure 4.2 (b) inset). Unlike the underdoped samples, no high bias conductance peaks are observed. Above the superconducting transition only a V-shaped background remains. The strength of the V-shaped background varies from junction to junction, and is most likely influenced by the quality of cleaved sample surface. Near optimal doped samples with x = 0.07 (T_c^{onset} = 23 K) and x = 0.08 (T_c^{onset} = 25 K) show similar spectra with Andreev peaks below T_c and a V-shaped background above it [Figure 4.4 (c), (d)].

4.1.4 K underdoped $BaFe_2As_2$

Figure 4.3 (a) shows dI/dV for $Ba_{0.8}K_{0.2}Fe_2As_2$. They are grown in Sn flux [68]. These crystals show a coexistence of magnetism and superconductivity [69] ($T_N = T_S \sim 90$ K, $T_c^{onset} = 26$ K). Low temperature spectra show Andreev peaks (Figure 4.3 (a) inset). The Andreev signal disappears above $\sim$ 15K leaving behind a background that does not change with a further increase in temperature. Unlike $BaFe_2As_2$ and $Ba(Fe_{1-x}Co_x)_2As_2$, the background for $Ba_{0.8}K_{0.2}Fe_2As_2$ is downward sloping at high bias voltages, as is typical of PCS junctions on normal metals [40].

Figure 4.3 (b) shows zero bias conductance (ZBC) curves for $Ba(Fe_{0.945}Co_{0.055})_2As_2$ and $Ba_{0.8}K_{0.2}Fe_2As_2$. These zero bias conductance curves are for the same junctions whose voltage and temperature evolutions have been presented in Figures 4.2 (a) and 4.3 (a). Superconductivity and magnetism coexist in both samples and both show Andreev spectra below T_c. However, while PCS spectra on underdoped crystals with Co doping show a

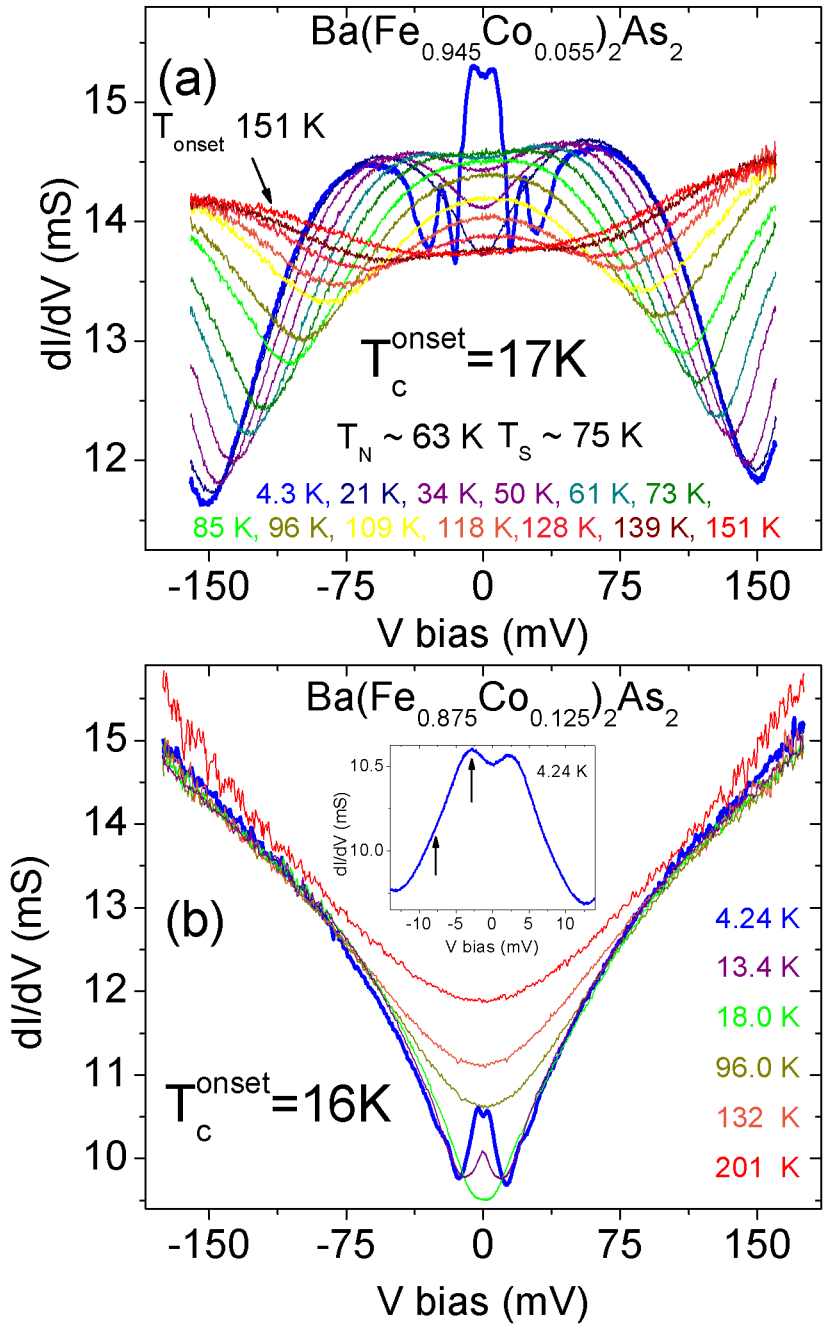

Figure 4.2: (a) dI/dV for underdoped $Ba(Fe_{0.945}Co_{0.055})_2As_2$. Like the 5% Co doped crystal [Figure 4.1 (b)], the spectra depict high bias conductance peaks coexisting with Andreev reflection. (b) Overdoped 12.5% Co shows Andreev spectra below T_c, and no high bias conductance peaks. The inset shows the Andreev peaks at low temperature.

conductance enhancement that lasts above T_S, no such enhancement is observed on underdoped crystals doped with K. The insets of the PCS dI/dV curves in the figure correlate the spectra obtained at different temperatures to their positions on the ZBC curves. The magnetic and structural transition temperatures are marked by vertical dashed lines on the ZBC curves. It is pertinent to note here that in $BaFe_2As_2$, K substitutes Ba to cause hole doping while Co replaces Fe to cause electron doping. In addition, Co doping causes the magnetic and structural transitions to split with $T_S > T_N$. For K doping, the two transitions occur at the same temperature ($T_N = T_S$).

4.2 $SrFe_2As_2$ and $CaFe_2As_2$

Single crystals of $SrFe_2As_2$ are grown out of FeAs flux as described in [62, 63]. $CaFe_2As_2$ crystals are grown from both Sn and FeAs flux [90]. Figure 4.5 (a) shows the PCS dI/dV for $SrFe_2As_2$; and Figure 4.6 (a) for $CaFe_2As_2$. The trend for $SrFe_2As_2$ is very similar to that of $BaFe_2As_2$. It has a $T_N = T_S$ of $\sim$ 190 K and a T_o of $\sim$ 240 K. (Data are taken on an unannealed sample; annealing increases T_S to 200 K) [63]. However, $CaFe_2As_2$ shows a different behavior. Of the 13 junctions tested, 11 of them showed a conductance enhancement disappearing above 100 K-110 K, below $T_N = T_S \sim 170$ K. For the remaining 2, the enhancement is observed as high as 170-180K.

4.3 $Fe_{1+y}Te$

$Fe_{1+y}Te$ single crystals are grown by a horizontal unidirectional solidification method [19]. Figure 4.7 (a) shows dI/dV for the Fe-chalcogenide $Fe_{1.13}Te$. Like $BaFe_2As_2$, $Fe_{1.13}Te$ shows a conductance enhancement that survives

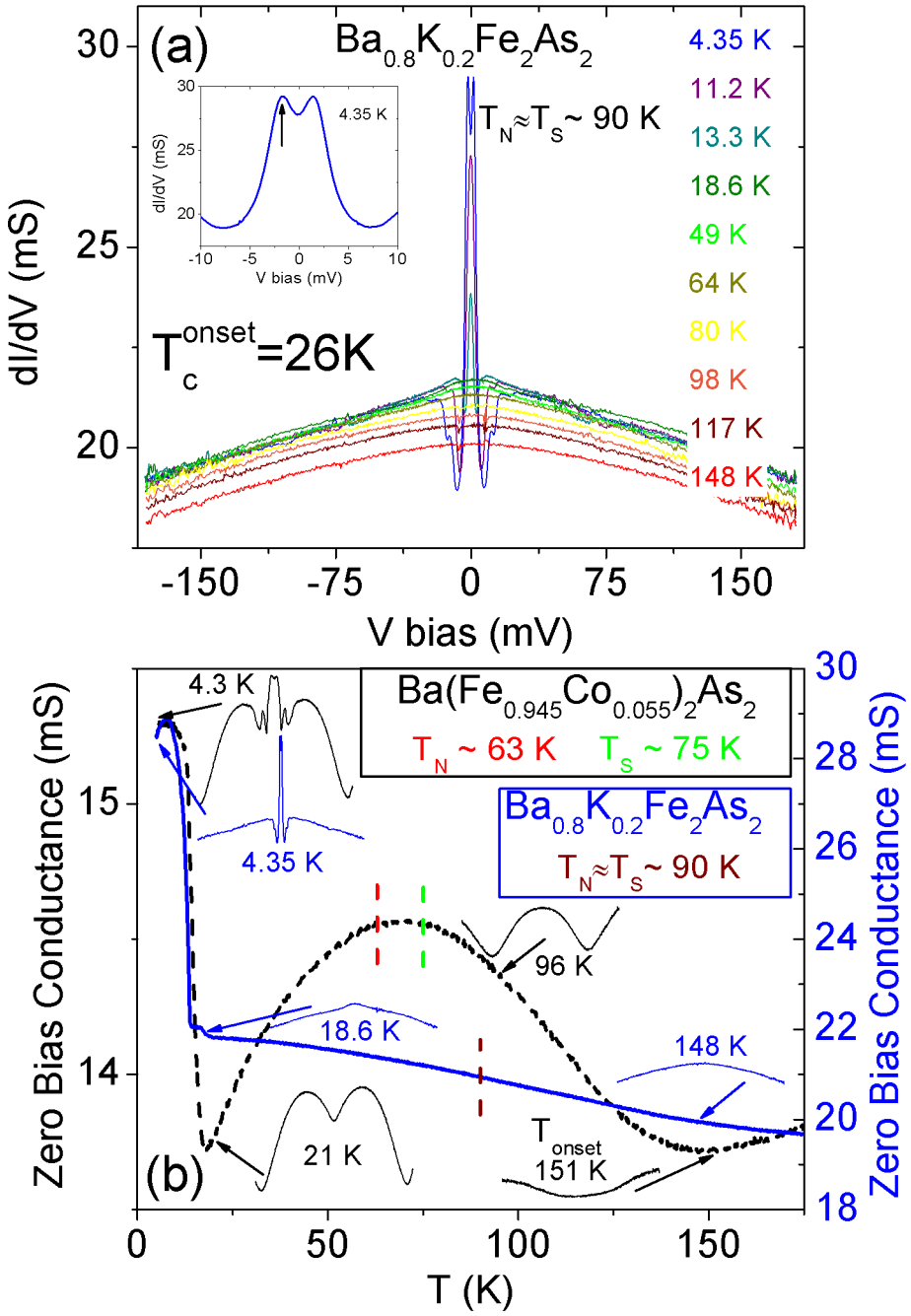

Figure 4.3: (a) dI/dV for hole doped $Ba_{0.8}K_{0.2}Fe_2As_2$. Andreev reflection is observed below T_c (inset), and there are no high bias conductance peaks. The background is concave down as opposed to the concave up seen for the Co doped crystals. (b) The zero bias conductance (ZBC) vs. T curves for 5.5% Co (black dashed curve) and 20% K (blue solid curve) corresponding to Figure 4.2 (a) and Figure 4.3 (a). Both compounds exhibit T_N, T_S and T_c. Underdoped crystals that are Co doped exhibit a conductance enhancement above T_S, while those underdoped with K do not. The insets correlate the spectra obtained at different temperatures to the ZBC curves.

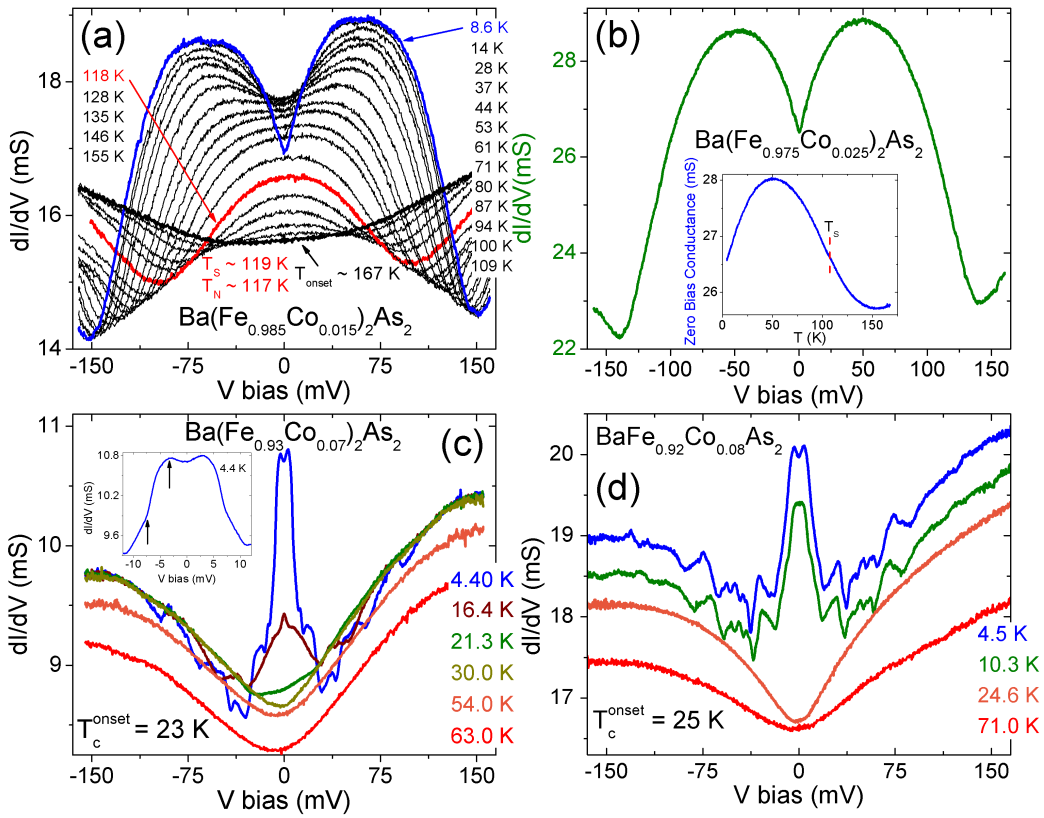

Figure 4.4: (a, b) dI/dV for nonsuperconducting underdoped $Ba(Fe_{0.985}Co_{0.015})_2As_2$ and $Ba(Fe_{0.975}Co_{0.025})_2As_2$. The spectra is very similar to that of $BaFe_2As_2$ shown in Figure 4.1 (a) and both dopings show a conductance enhancement above their magnetostructural transition. The inset of (b) shows the zero bias conductance vs. temperature curve. (c, d) dI/dV for near optimally doped $Ba(Fe_{0.93}Co_{0.07})_2As_2$ and $Ba(Fe_{0.92}Co_{0.08})_2As_2$. The spectra is very similar to that of overdoped $Ba(Fe_{0.875}Co_{0.125})_2As_2$ [Figure 4.2 (b)]. Andreev reflection is observed below T_c and the spectra above T_c is a parabolic background with no conductance enhancement. The arrows in the inset in (c) point out the Andreev peaks.

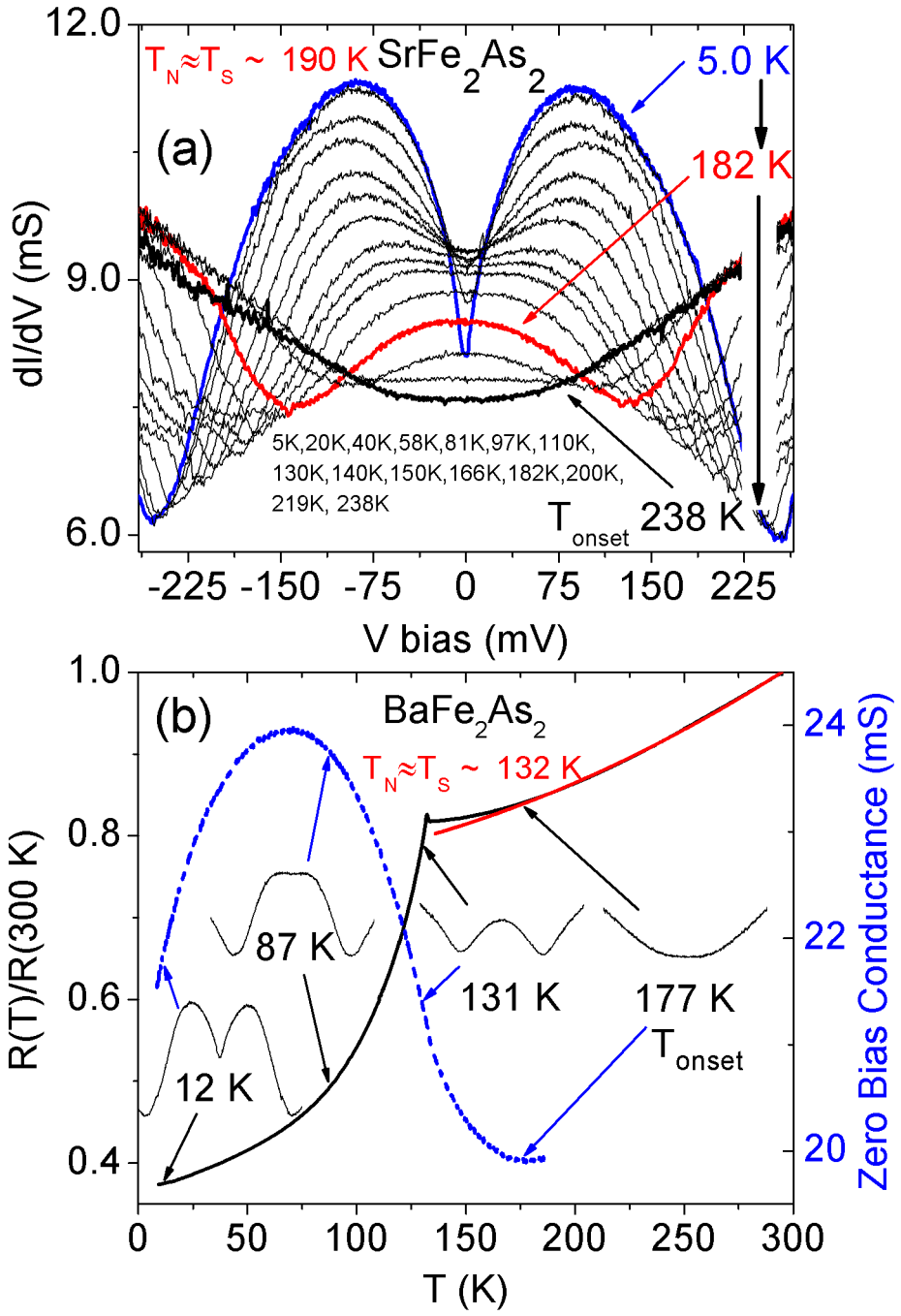

Figure 4.5: (a) PCS conductance spectra for $SrFe_2As_2$. Similar to $BaFe_2As_2$, the conductance enhancement lasts above $T_S \sim 190$ K. (b) The ZBC (blue dashed curve) and the resistance vs. temperature, (black solid curve) for the junction measured on $BaFe_2As_2$ from Figure 4.1 (a). The conductance enhancement lasts into the normal state. The insets correlate the spectra obtained at different temperatures to the ZBC curve. The red curve is a fit to $\rho = \rho_0 + AT^2$, as discussed in Section 4.4. Note that the bulk resistivity and ZBC curves are very different. This is an important diagnostic for PCS junctions and is discussed in detail in Chapter 5.

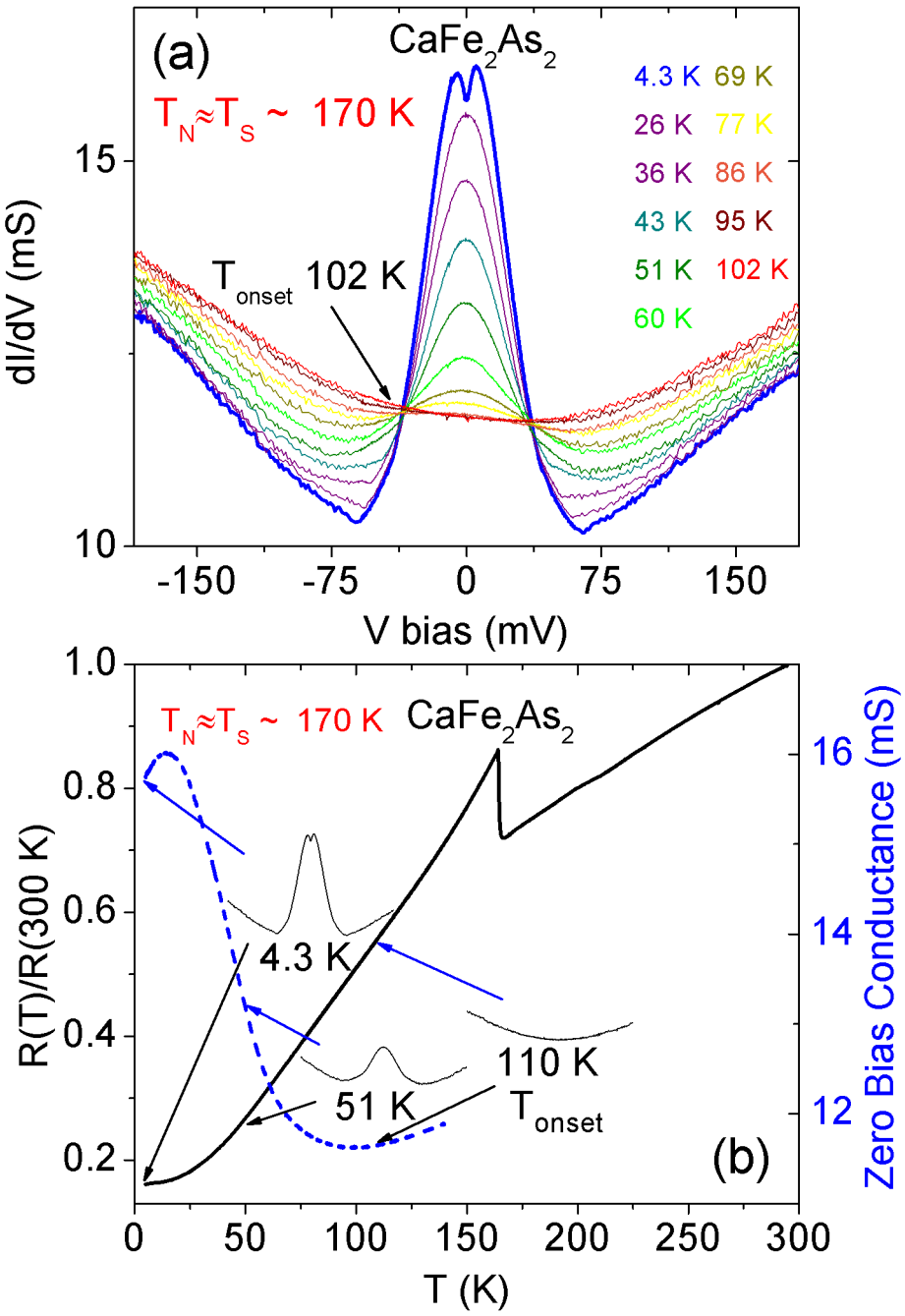

Figure 4.6: (a) PCS Conductance spectra for $CaFe_2As_2$. Unlike $BaFe_2As_2$ and $SrFe_2As_2$, the conductance enhancement disappears below T_S. (b) The ZBC (blue dashed curve) and the resistance vs. temperature, (black solid curve) for $CaFe_2As_2$. The conductance enhancement disappears below T_S. The insets correlate the spectra obtained at different temperatures to the ZBC curve. Note that the bulk resistivity and ZBC curves are very different. This is an important diagnostic for PCS junctions and is discussed in detail in Chapter 5.

above the magnetic and structural transition temperatures. The conductance enhancement is observed up to 75 K ($T_N = T_S \sim 59$ K). $Fe_{1.03}Te$ (data not shown) shows a conductance enhancement as high as 85 K ($T_N = T_S \sim 69$ K).

Figures 4.5 (b), 4.6 (b), and 4.7 (b) show zero bias conductance (blue dashed) and bulk resistivity $R(T)$ (black solid) curves for $BaFe_2As_2$, $CaFe_2As_2$ and $Fe_{1.13}Te$. The conductance enhancement above T_S is clearly seen for $BaFe_2As_2$ and $Fe_{1.13}Te$. No conductance enhancement above T_S is seen for $CaFe_2As_2$. The insets in these figures show the conductance spectra taken at the temperatures noted. Note that for all the crystals, the bulk resistivity and ZBC curves are very different. This is an important diagnostic for the quality of PCS junctions and is discussed in detail in Chapter 5.

To summarize thus far, we have studied iron based compounds that exhibit magnetic and structural transitions. $BaFe_2As_2$, $SrFe_2As_2$, underdoped $Ba(Fe_{1-x}Co_x)_2As_2$ and $Fe_{1+y}Te$ exhibit a dI/dV enhancement that sets in above T_S, $CaFe_2As_2$ only shows the enhancement below T_S while $Ba_{0.8}K_{0.2}Fe_2As_2$ does not show any conductance enhancement. Overdoped $Ba(Fe_{1-x}Co_x)_2As_2$ crystals do not undergo a magnetostructural transition and do not exhibit any conductance enhancement in their normal state; they show Andreev spectra below T_c. The high bias background for all compounds except for $Ba_{0.8}K_{0.2}Fe_2As_2$ is concave up.

4.4 Discussion

The iron based superconductors form dense structural twinned domains upon being cooled across their tetragonal to orthorhombic structural transition [91, 60]. The twins correspond to the alteration of the orthorhombic a and

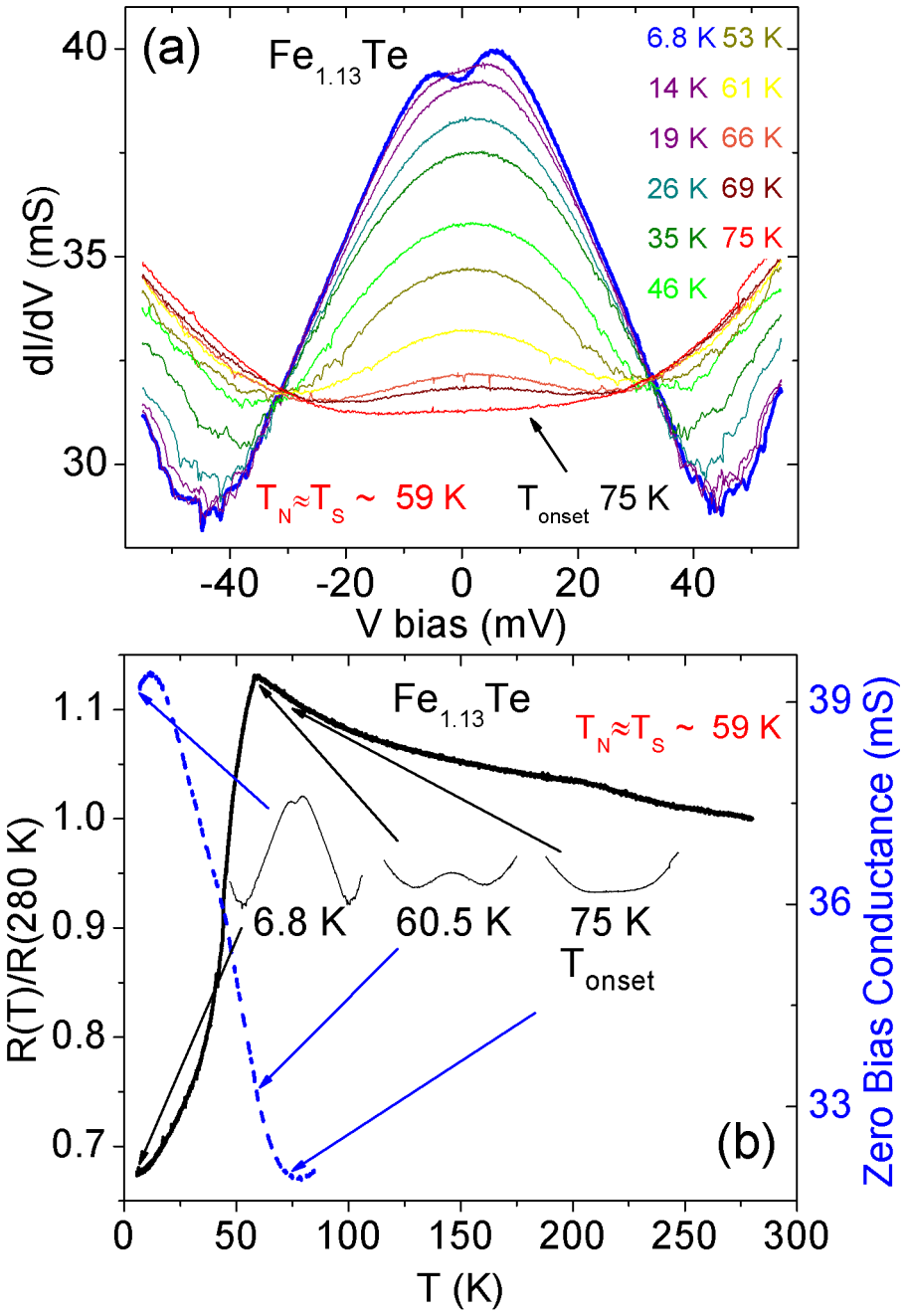

Figure 4.7: (a) PCS Conductance spectra for $Fe_{1.13}Te$ show an enhancement that lasts above T_S. (b) The ZBC (blue dashed curve) and the resistance vs. temperature, (black solid curve) for $Fe_{1.13}Te$. The enhancement lasts into the normal state. The insets correlate the spectra obtained at different temperatures to the ZBC curve. Note that the bulk resistivity and ZBC curves are very different. This is an important diagnostic for PCS junctions and is discussed in detail in Chapter 5.

b axes [Figure 4.8 (a)]. The twinning hides any electronic anisotropy that may be present in the orthorhombic phase. Twinning may be prevented from occurring if uniaxial stress or strain is applied on the crystal as it is cooled across the structural transition. The compressive stress defines the direction in which the shorter b axis of the orthorhombic lattice forms.

We compare the presence of the conductance enhancement in the PCS spectra of compounds presented in the previous sections with their in-plane resistivity behavior. For detwinned underdoped $AEFe_2As_2$ it has been shown that below T_S in the orthorhombic state, a resistive anisotropy exists [60, 92, 93]. Above T_S, in the tetragonal state, since the applied uniaxial stress/strain is already breaking the four-fold symmetry of the lattice, some finite resistive anisotropy may be expected to be detected. It is found that above T_S there is notable anisotropy for AE = Ba, negligible anisotropy for AE = Sr and no anisotropy for AE = Ca [Figure 4.8 (b)] [93]. This means that certain iron based superconductors have a strong nematic susceptibility above T_S that couples to the applied stress/strain and causes in-plane resistive anisotropy in the tetragonal state. Figure 4.8 (e) shows the in-plane resistivity behavior of detwinned $Ba(Fe_{1-x}Co_x)_2As_2$ [88]. Resistive anisotropy is detected for the underdoped samples but not for the optimally doped one. Detwinned underdoped $Ba_{1-x}K_xFe_2As_2$ does not show any anisotropy at all, either below or above T_S [Figure 4.8 (c)] [94]. Detwinned $Fe_{1+y}Te$ shows a resistive anisotropy above the structural transition [Figure 4.8 (d)] [95].

For the crystals that show resistive anisotropy above T_S, the magnitude of the anisotropy is sensitive to the uniaxial force being applied to ensure electronic detwinning. However, it is clear from the in-plane resistivity behavior of the detwinned iron based superconductors that some of them have a strong nematic susceptibility above T_S while others do not.

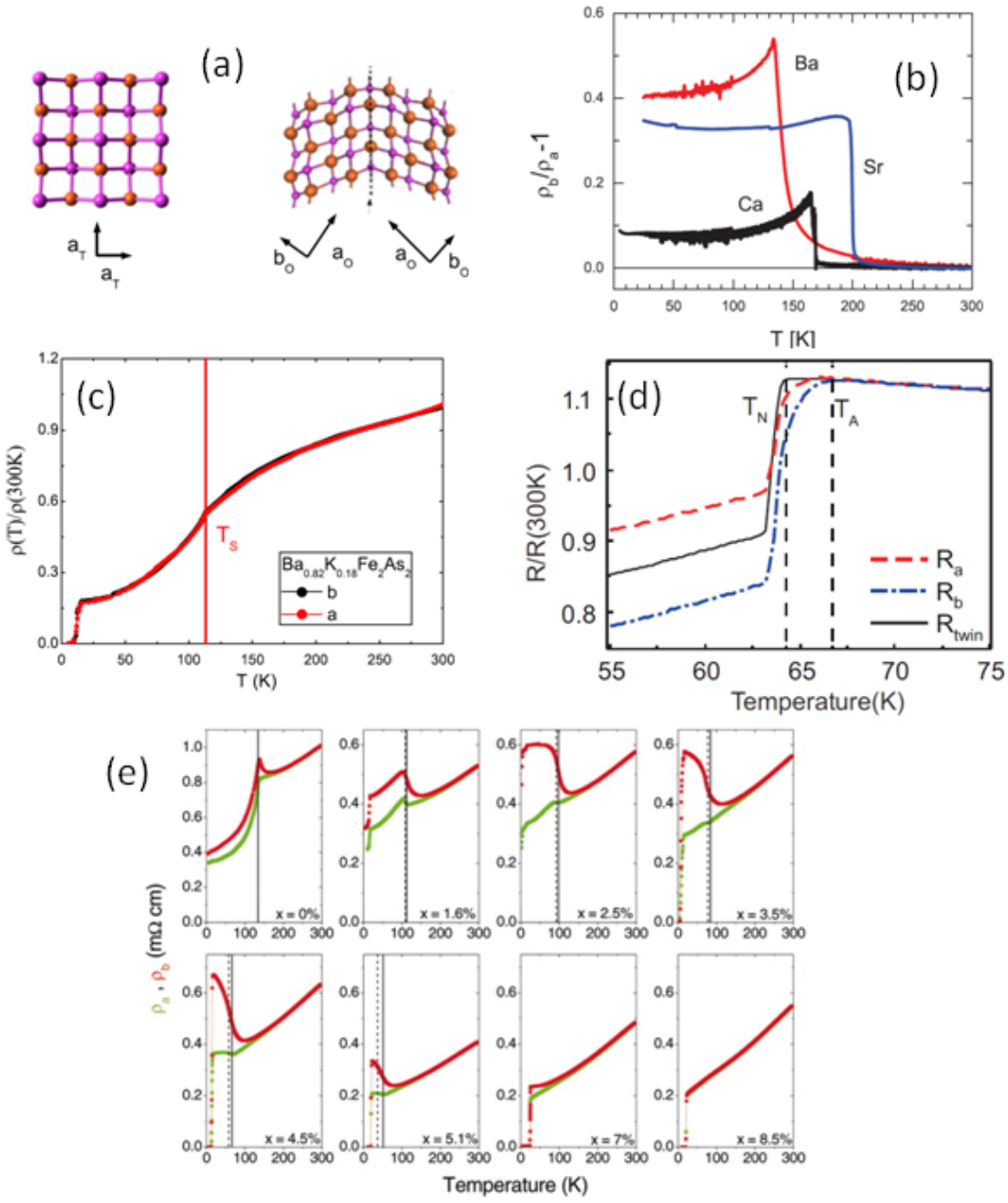

Figure 4.8: (a) Twin formation in the iron based superconductors as the lattice changes from a tetragonal symmetry to an orthorhombic symmetry. From [60]. (b) Detwinned underdoped $AEFe_2As_2$ exhibit a resistive anisotropy below T_S. For AE = Ba, this anisotropy sets in above T_S. From [93]. (c) Detwinned underdoped $Ba_{1-x}K_xFe_2As_2$ does not show any anisotropy at all, either below or above T_S. From [94]. (d) Detwinned $Fe_{1+y}Te$ shows a resistive anisotropy above the structural transition. From [95]. (e) Resistive anisotropy is detected for the underdoped $Ba(Fe_{1-x}Co_x)_2As_2$ but not for the optimally doped one. From [88].

We have used PCS to probe unstressed crystals along the c-axis. The presence or absence of the in-plane resistive anisotropy matches with whether a conductance enhancement is detected or not. For underdoped $Ba(Fe_{1-x}Co_x)_2As_2$ and $Fe_{1+y}Te$ PCS detects a conductance enhancement in the normal state and they also have a resistive anisotropy in the normal state. For $CaFe_2As_2$ PCS only detects a conductance enhancement below T_S and it develops a resistive anisotropy only below T_S. For underdoped $Ba_{1-x}K_xFe_2As_2$ and overdoped $Ba(Fe_{1-x}Co_x)_2As_2$ PCS does not detect any conductance enhancement and these compounds do not have any resistive anisotropy.

This indicates strongly that the conductance enhancement we observe is caused by the same phenomenon that causes the in-plane resistive anisotropy in the iron based superconductors.

The normal state resistivity of metals may be fit to a power law $\rho = \rho_0 + AT^\alpha$ where $\alpha = 2$ for standard Fermi liquid theory. Figure 4.5 (b) shows such a fit for as-grown unstressed $BaFe_2As_2$. From 300 K down to $\sim$ 180 K, the resistance follows a T^2 dependence. The deviation from $\alpha = 2$ sets in very close to T_o. This suggests that the conductance enhancement observed by PCS is tied to the deviation from Fermi liquid behavior in $BaFe_2As_2$.

To reiterate, at high temperatures $BaFe_2As_2$ behaves as a standard Fermi liquid. Around $\sim$ 180 K, a strong nematic susceptibility develops, and the bulk resistivity deviates from Fermi liquid behavior. This is the same temperature at which PCS dI/dV starts showing a conductance enhancement around zero bias.

We construct a revised phase diagram for $Ba(Fe_{1-x}Co_x)_2As_2$, [Figure 4.9 (a)] marking a new line on the underdoped side showing the temperature below which the conductance enhancement is observed. The onset temperature

for the conductance enhancement decreases as the Co doping is increased. The enhancement coexists with superconductivity at low temperatures.

Recent theoretical work [75] has shown that orbital fluctuations above T_S are expected to provide extra contributions to the single particle density of states (DOS) at zero energy. The DOS were shown to follow a log dependence as the energy is increased. We provide a brief overview of this work in Section 4.5. Figure 4.9 (b) shows that our conductance enhancement for $BaFe_2As_2$ above T_S follows a log dependence from $\sim$ 40 mV to $\sim$ 90 mV. Thermal population effects at 135 K cause scatter in the data at low bias voltage. Similar fits are observed above T_S for $SrFe_2As_2$ and $Fe_{1.13}Te$. Furthermore, the absence of similar effects in our data on $Ba_{0.8}K_{0.2}Fe_2As_2$ is consistent with the prediction that crystals that do not show the stress-induced resistance anisotropy will also not exhibit the excess conductance due to orbital fluctuations [75]. Our data therefore strongly indicates that the enhancement in conductance observed by our experiments is a consequence of orbital fluctuations.

It should be kept in mind that the dI/dV measured by point contact spectroscopy does not directly correspond to the density of states. Our measured conductance is a convolution of the Fermi velocity and the energy dependent density of states along with any scattering processes that might be present. For normal metals, the Fermi velocity and the density of states are inversely related and cancel each other out [37]. There is a lack of theoretical models for interpreting PCS data on correlated metals, where the DOS are energy dependent and do not cancel out with the Fermi velocity when dI/dV is measured. A theory considering both the energy dependence of the electronic DOS and scattering processes would be extremely helpful in obtaining a better understanding of the experimental data. W.-C. Lee et al. [96] are

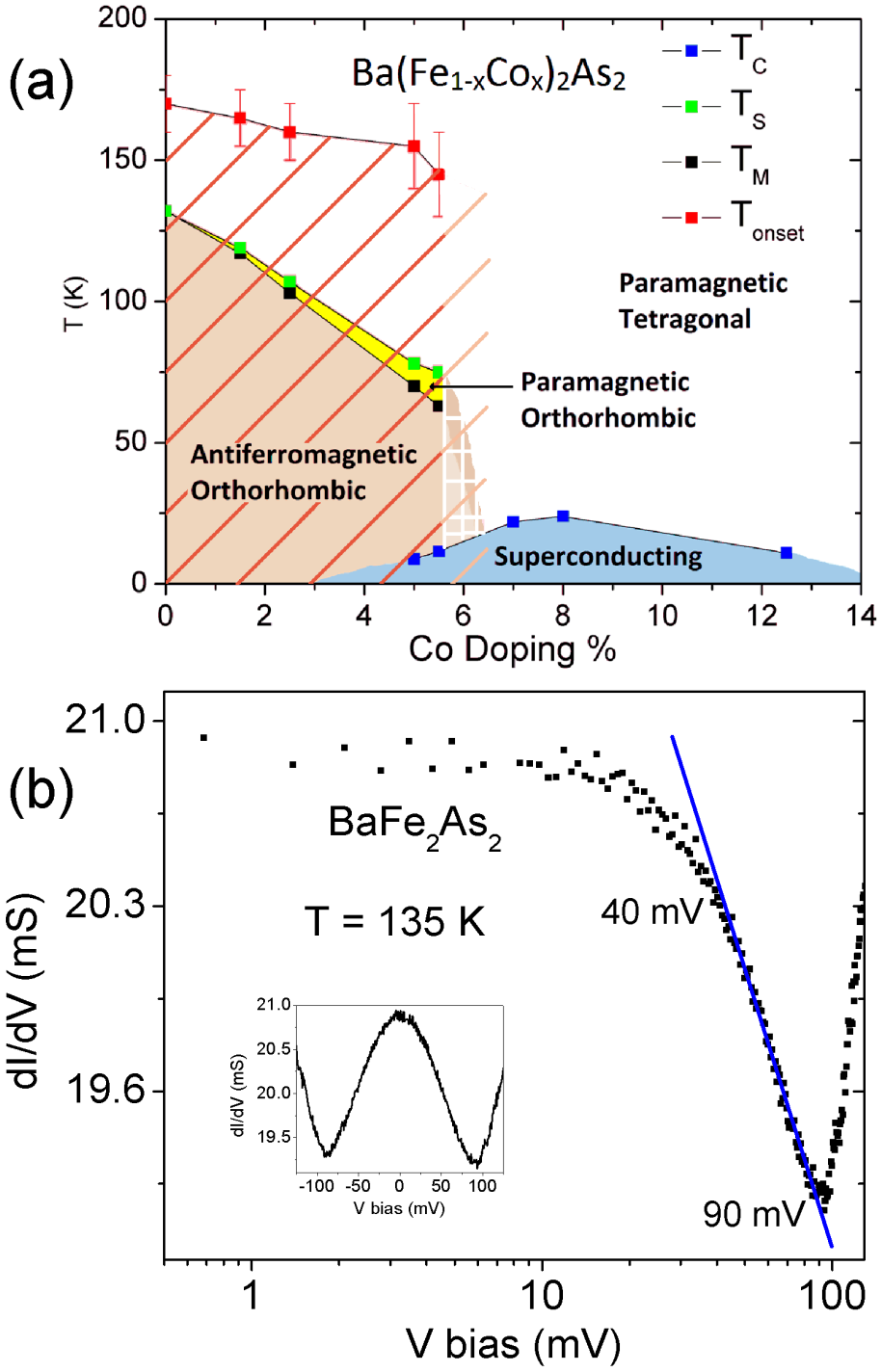

Figure 4.9: (a) Phase diagram for $Ba(Fe_{1-x}Co_x)_2As_2$. The structural, magnetic and superconducting transition temperatures (T_S, T_M, T_C) are determined by bulk resistivity measurements. For the underdoped side, a new region is marked (diagonal stripes) indicating the conductance enhancement that sets in above T_S. From [65]. (b) dI/dV above T_S for $BaFe_2As_2$ follows a log dependence from $\sim$ 40 mV to $\sim$ 90 mV. Such a behavior is predicted by [75].

working on developing such a model. Their preliminary work shows that as the size of the contact is reduced from the thermal to the ballistic limit, the transport evolves from the two-particle Green's function (resistivity, electronic transport) to the one-particle Green's function (tunneling density of states).

With decreasing temperature, the excess conductance curves all develop a dip at zero bias that sharpens as the temperature is lowered further. This could happen if there are two dominant scattering processes with opposite voltage dependence at work, and the crossover between them giving rise to a double peak structure about zero bias in dI/dV. PCS on Kondo systems shows a similar effect where the Kondo scattering and phonon scattering give rise to a similar split peak structure in dI/dV [97]. An alternate explanation is that this may be due to the formation of the spin density wave (SDW) gap. Previous work has shown PCS to be sensitive to such gapping [86, 87]. For $BaFe_2As_2$, the conductance peak to peak distance lies between 110-140 mV. This agrees well the SDW gap size (100-125 mV) reported by Raman spectroscopy, optical conductivity and ARPES [98, 99, 100, 101, 102] However, dI/dV increases logarithmically near zero bias (Figure 4.1 (b) left inset) which lends support to the scattering scenario.

A maximum is observed at $\sim$ 200 K in the interplane c-axis resistivity of $BaFe_2As_2$ [103], marking the crossover from high temperature nonmetallic to low temperature metallic behavior. The T_o determined from our PCS data occurs at a comparable temperature to this maximum. However unlike our data, the c-axis resistivity maximum is observed at all Co dopings.

Evidence for normal state nematicity/nematic susceptibility from detwinned samples is complicated by the symmetry breaking pressure applied to detwin the crystal. Apart from the resistive anisotropy already discussed,

ARPES [104] detects orbital ordering, and optical conductivity detects [105] an in-plane anisotropy in the normal state of stressed samples. On unstressed twinned samples, inelastic neutron scattering reveals high energy (>100meV) spin excitations above T_S in $BaFe_2As_2$ [89], although that these are truly indicative of nematicity is unclear [106]. Torque magnetometry on unstressed $BaFe_2(As_{1-x}P_x)_2$ detects a C_4 symmetry breaking in the normal state, across the phase diagram [107]. Strong anisotropy observed by scanning tunneling microscopy on unstressed FeSe, that lacks long range magnetic order, has been explained using orbital ordering [108, 109].

4.5 Orbital Order and Orbital Fluctuations in the Iron Based Superconductors

This section is drawn from the papers [29, 75].

In the iron based superconductors, Fe^{2+} has six electrons in its $3d$ orbitals, and Hund's coupling should favor ferromagnetism. However, hybridization with the As p orbitals suppresses such an effect. This hybridization also causes multiple Fermi surfaces with separate electron and hole pockets to emerge. In all cases, the structural phase transition precedes or happens simultaneously with the magnetic transition i.e. $T_S \geq T_N$. Orbital ordering of the Fe d_{xz} and d_{yz} orbitals is postulated to be the driving force behind T_S. These two orbitals make dominant contributions on the Fermi surface as opposed to the other three Fe d orbitals (d_{xy}, $d_{x^2-y^2}$ and $d_{3z^2-r^2}$). The order parameter for the orbital ordering is m, the difference between the occupation number of the two orbitals: $m = n_{xz} - n_{yz}$. When d_{xz} and d_{yz} are degenerate, $m = 0$.

As discussed in Chapter 1, in the unfolded Brillouin zone, there is a circular hole pocket at the zone center $\Gamma = (0, 0)$, and elliptical electron pockets at $X = (\pi, 0)$ and $Y = (0, \pi)$. For simplicity, we ignore the second hole pocket at $\Gamma = (0, 0)$ and a possible third one at $M = (\pi, \pi)$. The eigenstates on different parts of the Fermi surface shall have different weights of d_{xz} and d_{yz} orbitals. In Figure 4.10, the Fermi surface with major d_{xz} contribution is colored red while that with major d_{yz} contribution is colored blue. Under a $\pi/2$ rotation, the shape of the Fermi surface stays the same but d_{xz} and d_{yz} orbitals swap places.

At high temperatures, the two orbitals are degenerate with equal occupancy numbers. Figure 4.10 (b) shows how the Fermi surfaces would change if the occupancy of d_{xz} becomes larger than that of d_{yz}. The hole pocket will be elongated along the x direction and shortened along the y direction. At the same time, the electron pocket at X will shrink while the one at Y will expand. If d_{yz} has a larger occupancy, the Fermi surfaces will change in the opposite directions, as shown in Figure 4.10 (c). The Fermi surface distortions cause Coulomb repulsion along one axis to become stronger than along the other axis, making the orthorhombic crystal structure more energetically favorable and causing the structural transition [110].

The Fermi surface distortions due to orbital ordering determine the wave vector for the stripe-like antiferromagnetic ordering in the iron based superconductors. The magnetic order is induced by nesting between the hole and electron pockets. As shown in Figure 4.10 (a), without orbital order, due to a mismatch between the shape of the hole and electron pockets, the nesting condition is not perfect and the nesting wavevector is incommensurate. However, once orbital order sets in, the Fermi surface distortions enhance the nesting condition along either the X or Y direction and the nesting wavevec-

tor is commensurate. d_{xz} orbital order promotes $(\pi, 0)$ magnetic order while d_{yz} orbital order promotes $(0, \pi)$ magnetic order.

This reasoning naturally explains why the structural transition, caused by the onset of orbital order, always precedes the magnetic transition.

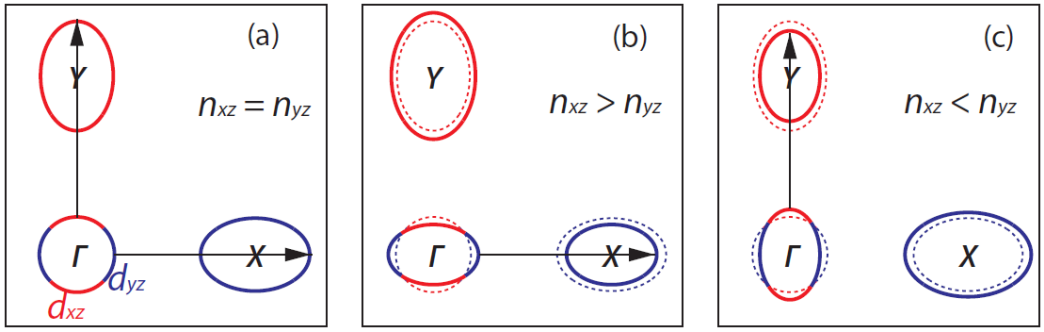

Figure 4.10: Fermi surface distortions due to orbital order. The area dominated by d_{xz} orbital is colored red while that with major d_{yz} orbital contribution is colored blue. The black arrows point out the nesting conditions between the hole and electron pockets. (a) Fermi surfaces without orbital order. The nesting condition is same along both axes. (b) Fermi surfaces with d_{xz} orbital order. The nesting condition is enhanced along the X axis. (c) Fermi surfaces with d_{yz} orbital order. The nesting condition is now enhanced along the Y axis. In (b) and (c) the original Fermi surfaces are represented by the dashed lines. From [29].

As mentioned in Section 4.4, nematic signals are detected in the normal state (above T_S) of certain iron based superconductors [60, 107, 104, 105, 89]. In point contact spectroscopy, certain compounds show a conductance enhancement above T_S. Such behavior may be explained by considering the effect of orbital fluctuations on the normal state properties of the iron based superconductors. A microscopic model developed by Wei-Cheng Lee et al. [75] shows how these fluctuations give rise to non-Fermi liquid behavior at temperatures higher than T_S. An overdamped collective mode develops at low frequencies in channels associated with the d_{xz} and the d_{yz} bands. The mode modifies the electron self-energy and we show how this is likely responsible for the conductance enhancement above T_S observed by PCS.

Wei-Cheng Lee et al. use random phase approximation (RPA) to calculate the electron self-energy. The details of their calculation are provided in [75]. Figure 4.11 summarizes the results of their theory. Here U determines the interaction term in the hamiltonian. Figure 4.11 (a) shows the orbital fluctuation spectrum for different values of U. At low frequencies, the spectrum is dominated by an overdamped collective mode, highlighted by the arrow in the figure. In the calculation, U has a critical value of ~ 2.1 eV and as this value is approached, the overdamped mode gains more and more spectral weight. Thus there is an enhanced density of states at low frequency, and the electron self-energy moves away from Fermi liquid behavior. Figure 4.11 (b) plots the electron self-energy vs. the frequency ω for different values of U. As U approaches its critical value, for low frequencies, the self energy moves from an $\sim \omega^2$ dependence (Fermi liquid behavior) to $\omega^\lambda, \lambda \leq 1$ dependence (non-Fermi liquid behavior).

The impact of this non-Fermi liquid behavior setting in above T_S is observable in the bulk resistivity of $BaFe_2As_2$. As shown in Figure 4.5 (b), the bulk resistivity starts deviating from the Fermi liquid T^2 behavior at $\sim$ 180 K, well above the the structural phase transition, and close to T_o, the temperature below which we start seeing a conductance enhancement around zero bias.

Lawler et al. [111] have shown that when nematic fluctuations are present, the single-particle density of states has the form:

$$N(\omega) = N(0) + B\omega^{2/3} ln\omega + ... \tag{4.1}$$

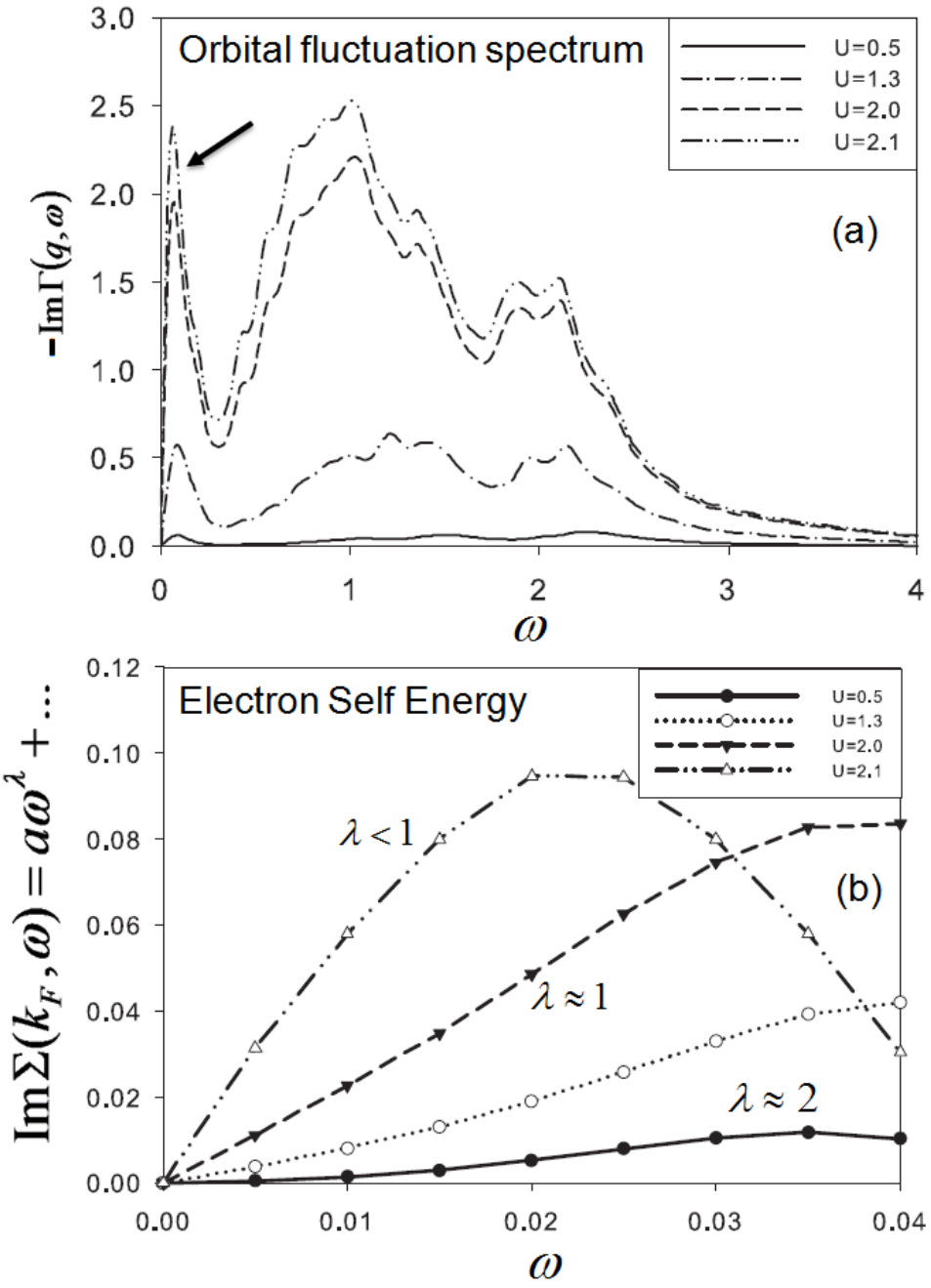

Figure 4.11: (a) Orbital fluctuation spectrum for different values of the interaction potential U. The arrow points out an overdamped collective mode that dominates the low frequency spectrum. As U approaches its critical value of ~ 2.1 eV, the overdamped mode becomes larger. (b) Electron self-energy for different values of U. For small U, the self-energy follows Fermi liquid behavior with $\lambda \sim 2$. As U approaches its critical value, non-Fermi liquid behavior emerges with $\lambda \leq 1$. Adapted from [75].

$N(\omega)$ obtains extra contributions due to the non-Fermi liquid self-energy. This causes a peak to occur in the density of states at zero frequency, and a subsequent decrease as the frequency increases.

Our data show that for correlated materials, the dI/dV measured by PCS reflects the density of states. Wei-Cheng Lee et al. have shown how orbital fluctuations cause a non-Fermi liquid to emerge above T_S and Lawler et al. have determined the density of states in the presence of such fluctuations. Therefore, in Figure 4.9 (b), for $BaFe_2As_2$, we show that our measured dI/dV at $T > T_S$ has a maximum at zero energy, and falls as a ln function as the energy is increased, in agreement with the theoretical predictions.

4.6 Isoelectronic Substituted $BaFe_2As_2$

So far we have shown that PCS detects a conductance enhancement above T_S in Co (electron) underdoped $BaFe_2As_2$ and this enhancement can be fully explained in the orbital fluctuations scenario. We have also discovered that K underdoped $BaFe_2As_2$ (hole doping) does not show such a signal. The third option of doping $BaFe_2As_2$ is isoelectronic substitution, where replacing As with P drives superconductivity. This section presents our results for PCS in the normal state of $BaFe_2(As_{1-x}P_x)_2$. Optimal T_c for this family is 30 K and is achieved for $\sim$ 32% P substitution. We present data obtained on an overdoped crystal 43% P, and an underdoped crystal 24% P. They are grown as described in [82, 83]. These crystals are highly reactive in air and most of the point contact junctions that we construct on them do not show Andreev reflection below T_c. Even though we are concentrating on the normal regime, we can only consider the data obtained from those junctions that do show Andreev reflection below T_c. The absence of an Andreev signal means that

the junction area is dominated by impurity/insulating oxides and any normal state spectra obtained from it cannot be trusted. The presence of an Andreev signal below T_c is an important junction diagnostic.

4.6.1 $BaFe_2(As_{0.57}P_{0.43})_2$

At 43% P, the crystal is over-substituted and superconducts at $\sim$ 25 K. Figure 4.12 shows the spectra for two different junctions on this crystal. At the lowest temperatures, both junctions show Andreev reflection at small voltage bias values.

For Figure 4.12 (a), two assymetric conduction peaks, centered at ~ 55 mV, coexist with the Andreev reflection. Above T_c, the Andreev reflection dies out and there is a dip at zero bias voltage. As the temperature is increased, the dip at zero bias fill up, the high bias conductance peaks move in, and the amplitude of the dI/dV signal becomes smaller and smaller. At 133 K, (the highest temperature for which we have data), the splitting between the high bias peaks is no longer visible, and the curve may be described as showing a broad enhancement around zero bias.

The situation is different for the junction in Figure 4.12 (b). At low temperatures, Andreev reflection is detected but no high bias conductance peaks are observed. Instead, there is a broad conductance enhancement centered at the zero bias voltage. As the temperature is increased, the amplitude of this enhancement is reduced. The reduction is smooth, and it is hard to spot a switching on temperature for this enhancement. Even at 200 K, a maximum at zero bias voltage is visible.

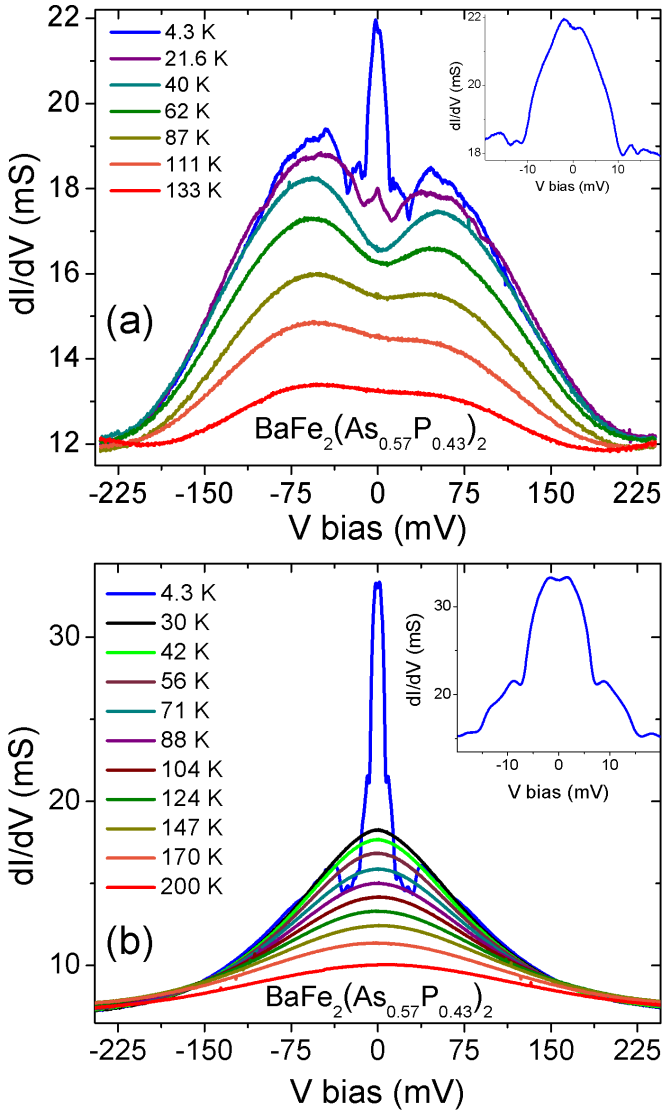

Figure 4.12: dI/dV for two different junctions on $BaFe_2(As_{0.57}P_{0.43})_2$. (a) For the first junction, at the lowest temperature, two assymetric conduction peaks, centered at ~ 55 mV, coexist with the Andreev reflection. As the temperature is increased, the high bias conductance peaks move in, and the amplitude of the dI/dV signal decreases. At 133 K, the splitting between the high bias peaks is no longer distinguishable, and the curve is essentially a broad conductance enhancement around zero bias. (b) For the second junction, Andreev reflection is detected but no high bias conductance peaks are observed. Instead, there is a broad conductance enhancement centered at the zero bias voltage. As the temperature is increased, the amplitude of this enhancement reduces smoothly. For both junctions, we cannot pinpoint a 'switching on' temperature for the conductance enhancement around zero bias.

4.6.2 $BaFe_2(As_{0.76}P_{0.24})_2$

The $BaFe_2(As_{0.76}P_{0.24})_2$ crystal is under-substituted, has a T_N of $\sim$ 70 K, and superconducts at $\sim$ 16 K. It is harder to observe Andreev reflection from $BaFe_2(As_{0.76}P_{0.24})_2$ than on $BaFe_2(As_{0.57}P_{0.43})_2$. One possible reason is that since the 24% P doped crystal is underdoped, its full volume might not be superconducting.

Figure 4.13 shows the spectra for two different junctions on this crystal that did show a good Andreev signal. Both junctions have higher bias conductance peaks at $\sim$ 60 mV that coexist with the Andreev signal. There is an upward turning background present for both the junctions as well. For Figure 4.13 (a), this background starts dominating the spectra from $\sim$ 120 mV onwards. For Figure 4.13 (b), the background is much stronger and becomes prominent from $\sim$ 95 mV onwards.

Unfortunately, we did not succeed in obtaining a temperature evolution of the spectra for either junction as for these particular crystals the change in temperature dramatically altered the junction properties.

4.6.3 Discussion

Unlike electron doped $Ba(Fe_{1-x}Co_x)_2As_2$, isoelectronic doped $BaFe_2(As_{1-x}P_x)_2$ shows high bias conductance peaks for both underdoped and overdoped crystals. Previously, we have tied the conductance enhancement detected by the point contact dI/dV to the nematic fluctuations present in the crystals. One signature of nematicity in the iron based superconductors is an in-plane resistive anisotropy that precedes the structural phase transition. In-plane resistive anisotropy on underdoped $BaFe_2(As_{1-x}P_x)_2$ has been detected by [112]. However, we are also detecting

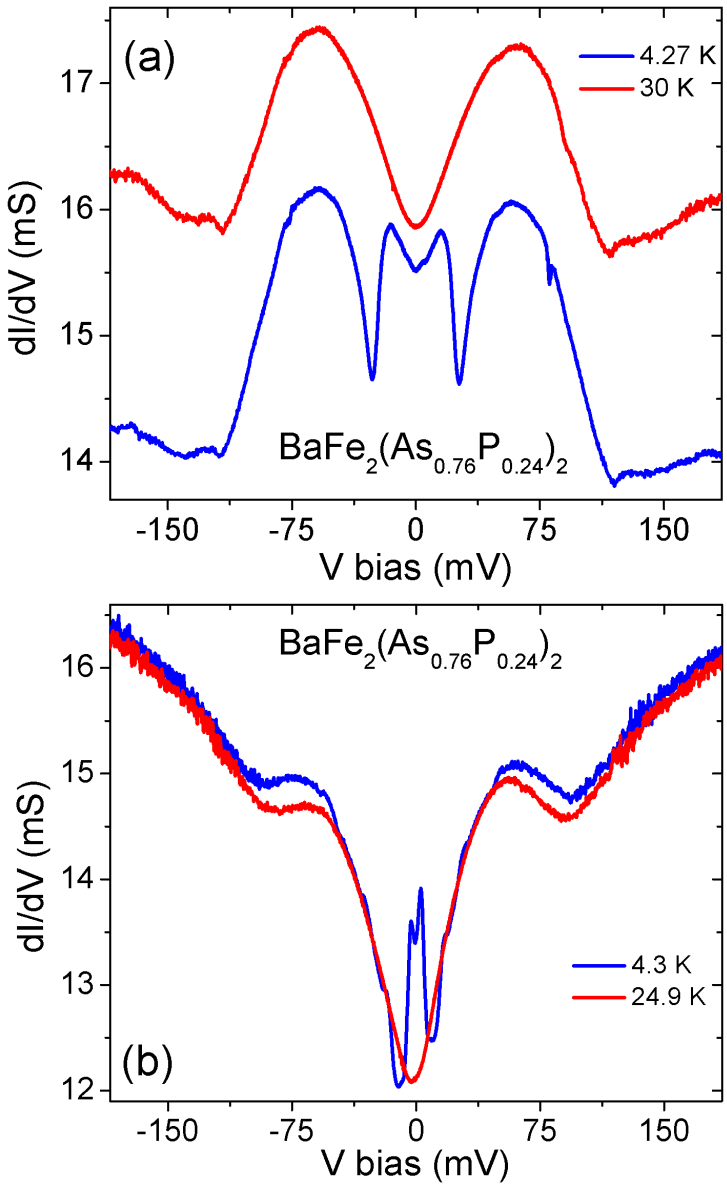

Figure 4.13: dI/dV for two different junctions on $BaFe_2(As_{0.76}P_{0.24})_2$. Both junctions have higher bias conductance peaks at $\sim$ 60 mV that coexist with the Andreev signal. There is an upward turning background present as well. For the junction in (a), the background starts dominating the spectra from $\sim$ 120 mV onwards, while for (b), the background is much stronger and becomes prominent from $\sim$ 95 mV onwards.

a conductance enhancement for overdoped $BaFe_2(As_{1-x}P_x)_2$, where a structural phase transition does not occur.

Nematic signals for $BaFe_2(As_{1-x}P_x)_2$ are observed by magnetic torque magnetometry and synchrotron X-ray measurements [107]. Torque magnetometry detects electron matter that breaks the tetragonal C_4 symmetry below a temperature $T^* > T_S$. X-ray detects a very small but finite lattice distortion in the same temperature range. Interestingly, both these techniques detect a T^* for overdoped $BaFe_2(As_{1-x}P_x)_2$, dopings that do not have a T_S. Keeping these measurements in mind, it is not surprising that PCS is also detecting a conductance enhancement for overdoped $BaFe_2(As_{0.57}P_{0.43})_2$.

The origins of the electron nematic state that occurs for $BaFe_2(As_{1-x}P_x)_2$ are not clear, with orbital fluctuations or spin fluctuations being the main contenders. While spin fluctuations is a plausible candidate for causing nematicity in the underdoped crystals, the observation of nematicity in the overdoped region far from the antiferromagnetic phase casts a strong doubt on this. Therefore, orbital fluctuations might be a better candidate for causing the nematic phase.

4.7 $NaFe_{1-x}Co_xAs$

In addition to the 122 and the 11 families of the iron based superconductors, we also probe the normal state of the 111 compounds. NaFeAs has an antiferromagnetic ground state. Bulk superconductivity is achieved by Co doping that suppresses the magnetic state [18]. Along with the undoped NaFeAs, we study underdoped $NaFe_{0.98}Co_{0.02}As$ ($T_c \sim 22.5$ K) and overdoped $NaFe_{0.94}Co_{0.06}As$ ($T_c \sim 20.2$ K). Na111 crystals are 100-150 μm in size and quite brittle. Handling them with tweezers often causes them to

crumble. These factors, along with their reactiveness in air makes obtaining good spectra from them very challenging.

4.7.1 NaFeAs

In literature, NaFeAs is reported to have a structural transition at $\sim$ 50 K and a magnetic transition at $\sim$ 40 K [18]. Completely pure NaFeAs does not superconduct. However, on exposure to air, oxidation occurs causing partial superconductivity [113]. Oxidizing the crystal gently with water extracts electrons and Na^+ cations from the structure, yielding $Na_{1-x}FeAs$ with a maximum T_c of $\sim$ 25 K. Oxidizing the sample more vigorously by exposure to air changes the structure to $NaFe_2As_2$ ($ThCr_2Si_2$-type) and results in a maximum T_c of $\sim$ 12 K.

We probe NaFeAs crystals grown from melt [Figure 4.14 (a)] and from NaAs flux [Figure 4.14 (b)]. They show us remarkably different spectra. For the melt grown crystal, at the lowest temperature we detect a very weak Andreev signal. This signal is superimposed on a broad conductance enhancement. Once the Andreev signal disappears, conductance peaks are detected at $\sim$ 22 mV and a minimum develops at zero bias voltage. As the temperature is increased, the peaks move in and the conductance enhancement is reduced. The dI/dV curve becomes completely flat around 90 K. The dI/dV values in Figure 4.14 (a) have been normalized to the values at -200 mV.

The situation for the flux grown crystal is completely different. At the lowest temperature, dI/dV exhibits a sharp dip at zero bias voltage. As the temperature is increased, the dip gets shallower and shallower, and disappears at $\sim$ 40 K, as pointed out by the black arrow in Figure 4.14 (b). This

is also the temperature at which the antiferromagnetic transition occurs in the crystal. Any further increase in temperature does not change the spectra. The inset in the figure shows the curve obtained at 99 K. It is strongly asymmetric with the positive voltage bias showing higher conductance values than the negative voltage bias. The dI/dV values in Figure 4.14 (b) have been normalized to the values at -100 mV, and all curves after the one at 4.3 K have been shifted vertically up by 0.005.

4.7.2 $NaFe_{0.98}Co_{0.02}As$

Figure 4.15 shows the dI/dV spectra obtained from two separate junctions on underdoped $NaFe_{0.98}Co_{0.02}As$, ($T_c \sim 22.5$ K). At the lowest temperatures, Andreev reflection is detected by both junctions (blue curves in Figures 4.15 (a), (b)). Above T_c, the Andreev reflection dies out leaving behind a broad asymmetric conductance enhancement centered at zero bias voltage (red curves in Figures 4.15 (a), (b)). Figures 4.15 (c), (d) show how this enhancement evolves for the junctions introduced in Figures 4.15 (a), (b), respectively. For (c), the spectra has been normalized with respect to the value at -150 mV while for (d) it has been normalized to the value at -70 mV. With increasing temperature, the conductance enhancement is reduced. For (c), the enhancement disappears between 117 K and 151 K, leaving behind an upward shaping, weakly parabolic background. The junction in (d) is only biased up to ± 70 mV, and at 85 K, the conductance enhancement appears to have disappeared within that voltage range, leaving behind an asymmetric background.

Many of our junctions on $NaFe_{0.98}Co_{0.02}As$ do not show Andreev reflection below T_c, but rather a peculiar asymmetric feature that we reproduce in

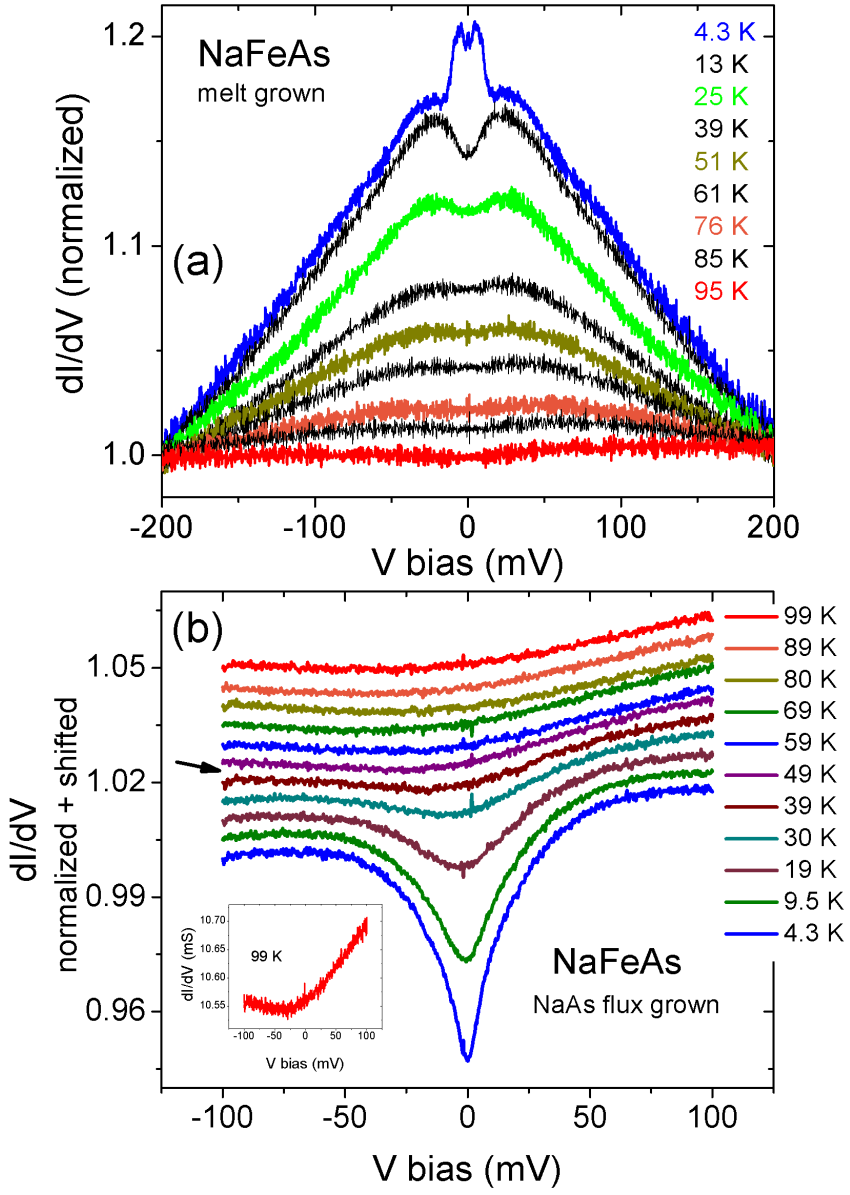

Figure 4.14: dI/dV for NaFeAs. (a) For melt grown NaFeAs, a weak Andreev signal is detected at the lowest temperature. A broad conductance enhancement is observed with peaks at $\sim$ 22 mV. With increasing temperature, the enhancement gets reduced and disappears around 90 K. (b) For flux grown NaFeAs, at the lowest temperature, dI/dV develops a sharp dip at zero bias voltage. The dip disappears close to T_N, $\sim$ 40 K, as pointed out by the black arrow in figure. Any further increase in temperature does not change the spectra. The inset shows dI/dV for 99 K. It is strongly asymmetric with the positive voltage bias showing higher conductance values than the negative voltage bias.

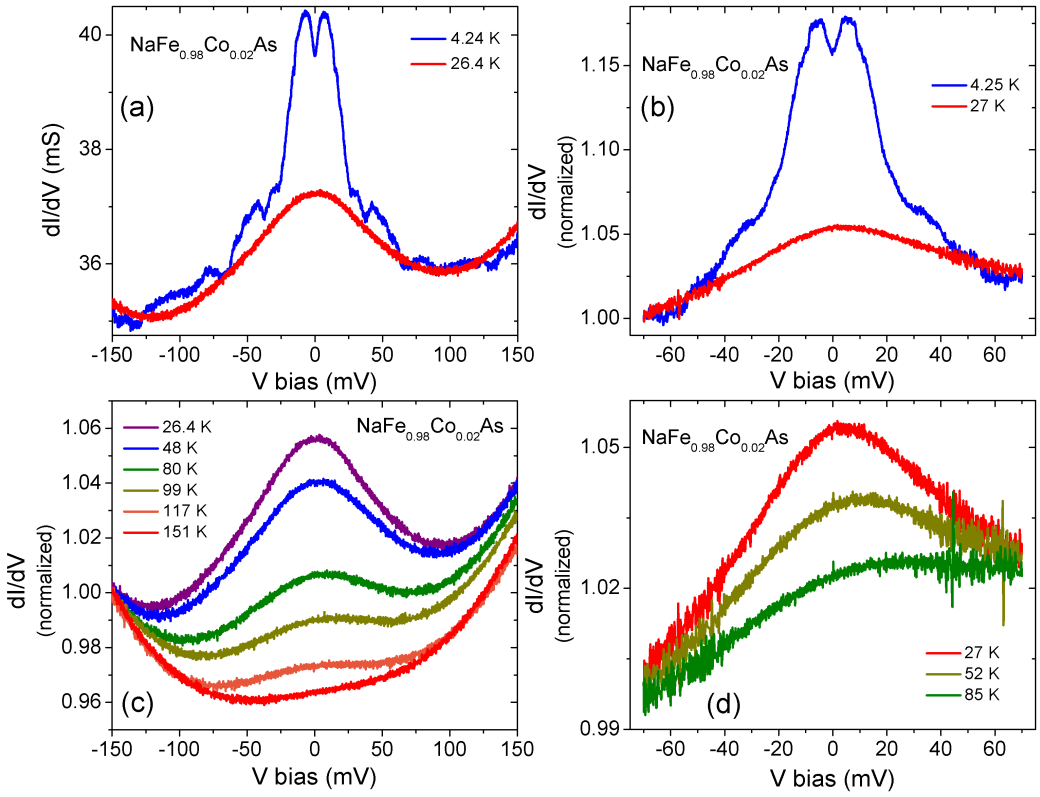

Figure 4.15: dI/dV for two different junctions on $NaFe_{0.98}Co_{0.02}As$. (a, b) At the lowest temperatures, Andreev reflection is detected by both junctions (blue curves). Above T_c, the Andreev reflection dies out leaving behind a broad asymmetric conductance enhancement centered at zero bias voltage (red curves). (c) Temperature evolution of the junction from (a). The conductance enhancement disappears between 117 K and 151 K, leaving behind an upward shaping, weakly parabolic background. (d) Temperature evolution of the junction from (b). At 85 K, the conductance enhancement appears to have disappeared within ±70 mV, leaving behind an asymmetric background.

Figure 4.17 (a). For the two junctions shown, dI/dV is larger for positive bias values than for the negative bias values. The gradient of the curve changes twice, at $\sim$ +5 mV and $\sim$ -5 mV. With increasing temperature, these features become thermally smeared and are not observable (not shown in figure).

4.7.3 $NaFe_{0.94}Co_{0.06}As$

The final compound of the Na111 family that we study is the overdoped $NaFe_{0.94}Co_{0.06}As$, with a $T_c \sim 20.2$ K. Figure 4.16 shows the data that we obtain from two separate junctions on this crystal.

The junction in Figure 4.16 (a) shows Andreev spectra at the lowest temperature (blue curve). The dI/dV also has some higher bias bumps present. At 22 K (above T_c, red curve), all these features disappear and only an asymmetric parabolic background remains. There is also a slight dip in the dI/dV around zero bias voltage, running for -15 mV to +15 mV. The inset shows that this dip has filled up by 40 K, and further increase in temperature causes no change in the spectra.

For the junction in (b), we only have the data for the lowest temperature. Just like the junction in (a), the conductance shows Andreev spectra at low biases, and has some bumps at higher bias values. Our speculation is that, just like the junction in (a), all these features would disappear above T_c, leaving behind a background that is fairly constant with further increase in temperature. The inset in the figure is a blow-up of the Andreev spectra, with the arrows pointing out the features corresponding to the multiple superconducting gaps.

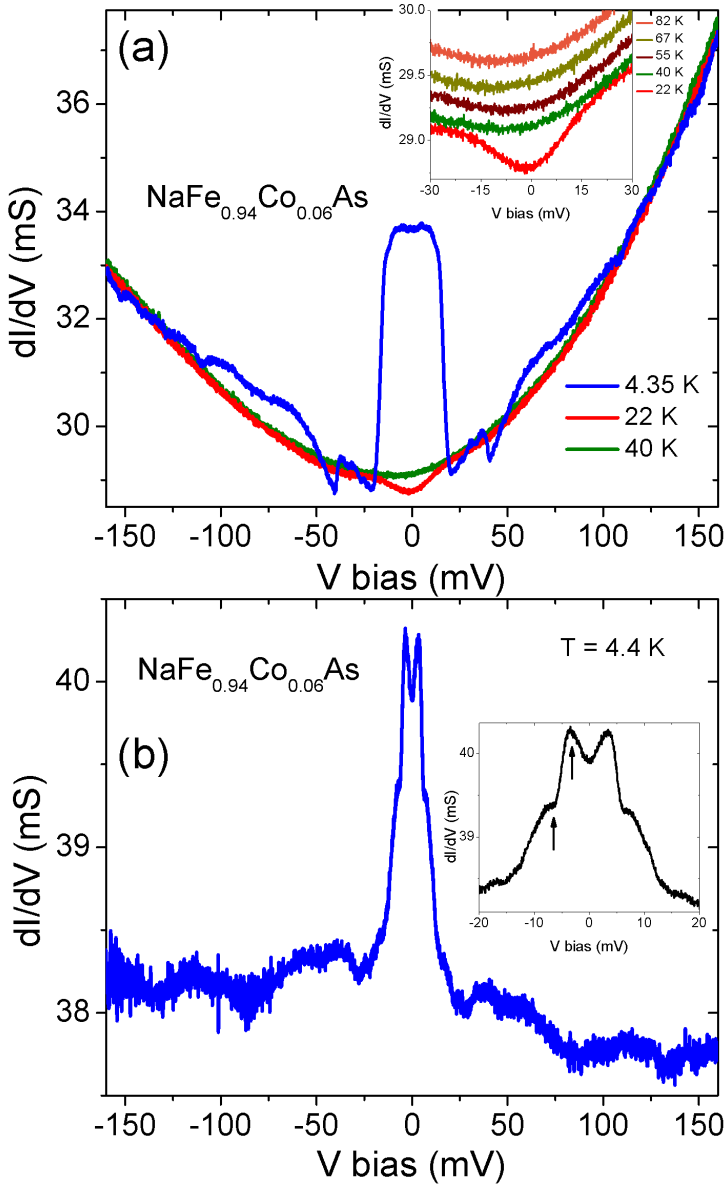

Figure 4.16: dI/dV for two different junctions on $NaFe_{0.94}Co_{0.06}As$. (a) At the lowest temperature, Andreev reflection, along with some bumps at higher bias values are detected (blue curve). Above T_c, the Andreev reflection dies out leaving behind an asymmetric parabolic background, and a slight dip in dI/dV, running for -15 mV to +15 mV (red curve). The inset shows that this dip has filled up by 40 K, and further increase in temperature causes no change in the spectra. (b) The second junction also shows Andreev reflection at the lowest temperature, along with some bumps at higher bias values. The inset is a blow-up of the Andreev spectra, with the arrows pointing out the features corresponding to the multiple superconducting gaps.

As we mentioned earlier for $NaFe_{0.98}Co_{0.02}As$, many of our junctions on $NaFe_{0.94}Co_{0.06}As$ also do not show Andreev reflection below T_c, but rather a peculiar asymmetric curve. Figure 4.17 (b) depicts such a spectra for two different junctions on $NaFe_{0.94}Co_{0.06}As$. These curves look fairly similar to the ones observed on $NaFe_{0.98}Co_{0.02}As$ [Figure 4.17 (a)].

4.7.4 Discussion

Melt grown NaFeAs shows us a conductance enhancement in the normal state reminiscent of what we observe on the 122 parent compounds and $Fe_{1+y}Te$. In addition, an in-plane resistive anisotropy that sets in above the structural transition has also been detected in NaFeAs [95]. Thus it is likely that the same mechanism is at play in all these compounds and the conductance enhancement observed in NaFeAs is also a consequence of orbital fluctuations.

The bigger puzzle is as to why the spectra obtained from flux grown NaFeAs are so different. Instead of an enhancement, a dip develops in the conductance and the temperature evolution of the dip tracks the T_N of the crystal. Scanning tunneling microscopy (STM) dI/dV has observed a similar feature from NaFeAs [114]. They attribute it to the gapping of the the Fermi surface due to the spin density wave transition. In addition, both STM and PCS detect a similar shaped asymmetric background for $T > T_N$.

As mentioned earlier, oxidation changes NaFeAs into $Na_{1-x}FeAs$ or $NaFe_2As_2$. Our crystals are most likely a combination of all three structures. Different levels of purity in the melt grown and flux grown NaFeAs is probably the cause of the variance in our spectra.

We also note that PCS spectrum similar to 'V' shaped curve obtained from flux grown NaFeAs has previosuly been seen on a variety of materials by our

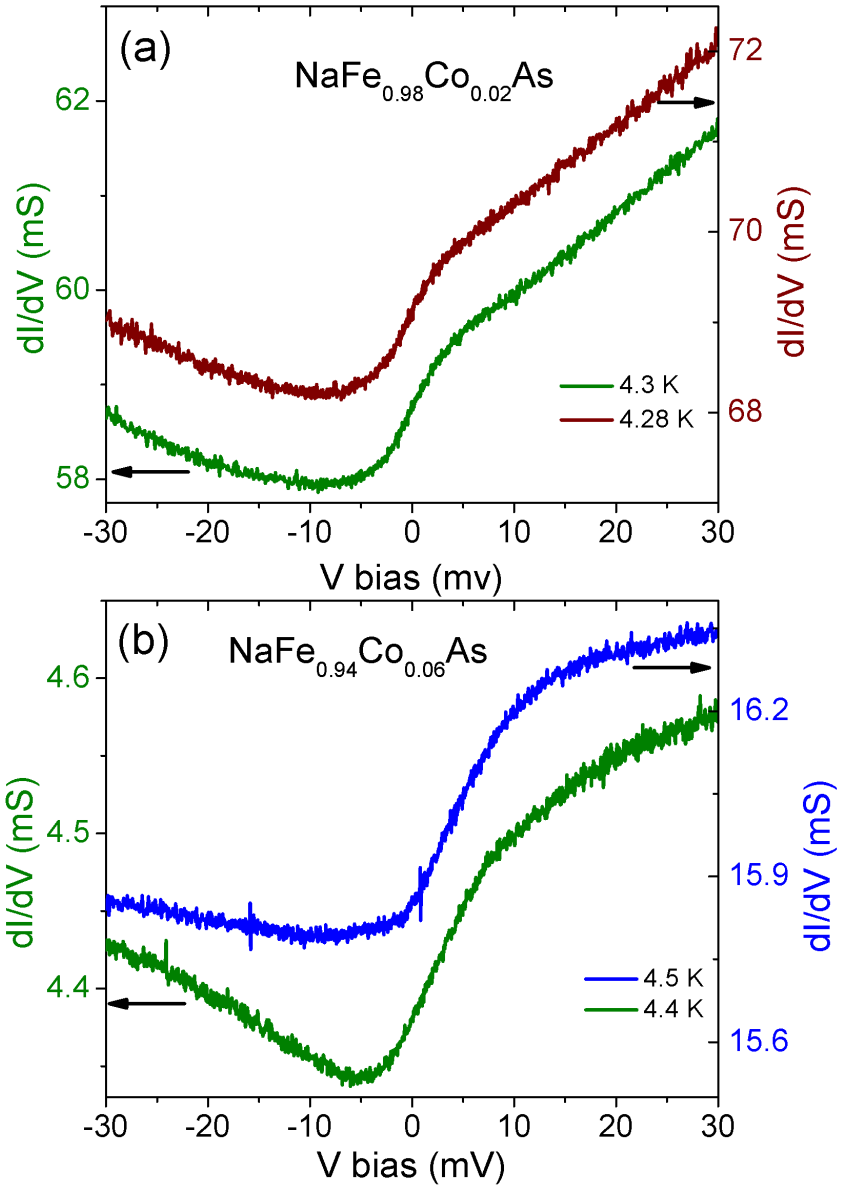

Figure 4.17: dI/dV curves below T_c that do not show Andreev reflection. (a) Two different junctions constructed on $NaFe_{0.98}Co_{0.02}As$. Instead of Andreev reflection, we observe a peculiar asymmetric feature. dI/dV is larger for positive bias values than for the negative bias values. The gradient of the curve changes twice, at $\sim$ +5 mV and $\sim$ -5 mV. (b) Two different junctions for $NaFe_{0.94}Co_{0.06}As$. These dI/dV curves are similar to the ones obtained for 2% Co doping and shown in (a).

research group, and might be an artifact caused by disorder in the system [115, 116]. In such a scenario, our data on flux grown NaFeAs [Figure 4.14 (b)] does not reflect the intrinsic properties of the crystal.

For underdoped $NaFe_{0.98}Co_{0.02}As$ we detect a dI/dV enhancement in the normal state while for overdoped $NaFe_{0.94}Co_{0.06}As$ such a signal is not present. Like undoped NaFeAs, underdoped detwinned $NaFe_{1-x}Co_xAs$ also has an in-plane resistive anisotropy above T_S (Figure 1 (b) in [117]). This matches up with the trend that PCS detects a conductance enhancement in the normal state if an in-plane resistive anisotropy exists. Based on our PCS results, overdoped $NaFe_{1-x}Co_xAs$ does not exhibit nematic susceptibility in its normal state.

The final puzzle is that instead of Andreev reflection below T_c, we occasionally pick up an anomalous, highly anisotropic dI/dV signal from both $NaFe_{0.98}Co_{0.02}As$ and $NaFe_{0.94}Co_{0.06}As$ (Figure 4.17). A comparison with a recent STM paper helps in providing an explanation [118]. The paper shows that while the surface of cleaved $Sr_{0.75}K_{0.25}Fe_2As_2$ is dominated by the Sr/K layer, patches of As interspersed between the Sr/K layer also exist. The superconducting gap is only detected on the Sr/K layer, while the As patches show an gapless, anisotropic dI/dV signal (Figure 1 (e) in [118]), that is very similar to our Figure 4.17. It is conceivable that the surface of cleaved $NaFe_{1-x}Co_xAs$ is dominated by either Na or As layers, and we pick up Andreev reflection from the Na portions and the anomalous, anisotropic signal from the As patches.

An apt summary of this chapter is dividing the iron based superconductors into two groups: those who show a dI/dV enhancement in their normal state and those who do not show such a feature. Table 4.1 presents the two groups.

Table 4.1: Crystals That Show dI/dV Enhancement In Their Normal State

Crystal	Yes	No
$BaFe_2As_2$	X	
underdoped $Ba(Fe_{1-x}Co_x)_2As_2$	X	
overdoped $Ba(Fe_{1-x}Co_x)_2As_2$		X
underdoped $Ba_{1-x}K_xFe_2As_2$		X
underdoped $BaFe_2(As_{1-x}P_x)_2$	X	
overdoped $BaFe_2(As_{1-x}P_x)_2$	X	
$CaFe_2As_2$		X
$SrFe_2As_2$	X	
$Fe_{1+y}Te$	X	
NaFeAs	X	
underdoped $NaFe_{1-x}Co_xAs$	X	
overdoped $NaFe_{1-x}Co_xAs$		X

CHAPTER 5

PCS JUNCTION DIAGNOSTICS

In Chapter 2 we discuss the different conduction regimes of a point contact junction. Spectroscopic information is only obtained if the size of the junction is comparable to the electron elastic and inelastic mean free paths. If the junction is in the thermal regime, increasing bias voltage causes local heating and the measured dI/dV resembles the bulk resistivity. We also mention that the physical size of a point contact junction does not give an accurate estimate of the effective size of the junction. This happens because the whole junction does not behave as a single channel, instead there are multiple parallel nanoscale channels dominating the current flow. A more accurate representation of what a point contact junction actually looks like is shown in Figure 2.5 (b).

To ensure that our point contact junction is in the appropriate conduction regime, we need to carry out certain diagnostics on our dI/dV spectra. This chapter covers these diagnostics.

5.1 PCS spectra on Superconductors

PCS spectra on superconductors is fit to the BTK model. We introduce the BTK model in Chapter 2. Under the BTK model, dI/dV enhancement due to Andreev reflection can reach a maximum of 100%, and that occurs only if Z=0. This makes it easy to spot thermal spectra. The biggest giveaway is

that thermal dI/dV shows an enhancement in excess of 100%. This happens because increasing bias voltage is driving the superconductor normal and causing a precipitous drop in the measured dI/dV.

Figure 5.1 shows thermal (green) and non-thermal (blue) spectra on $Ba(Fe_{0.93}Co_{0.07})_2As_2$ and $BaFe_2(As_{0.57}P_{0.43})_2$. The thermal spectra shows a peak at zero bias voltage and the dI/dV falls sharply as the bias voltage is increased. In fact, dI/dV at 0 mV is more than twice the dI/dV at 20 mV. Metallic PCS junctions cannot show such a large enhancement meaning that this feature is being caused by thermal heating at the junction which is driving the superconductor normal. Thus such junctions are not providing any spectroscopic information. On the other hand, the non-thermal spectra may be fit to the BTK model to extract the size and symmetry of the superconducting gaps. The BTK fit for the blue curve in Figure 5.1 (a) is shown in Figure 3.5 (a) while the fit for Figure 5.1 (b) is provided in Figure 3.12 (b).

Our aim is to make metallic point contact junctions on superconductors to observe Andreev reflection. However, every once in a while, we end up with junctions that instead of Andreev reflection, exhibit weak tunneling characteristics. This happens more frequently when working with the $NaFe_{1-x}Co_xAs$ and $BaFe_2(As_{1-x}P_x)_2$ crystals. Amongst the iron based superconductors, these two families are more reactive in air than $Ba(Fe_{1-x}Co_x)_2As_2$. This tunneling behavior is most likely due to the formation of an insulating oxide layer on the top of the crystal. Figure 5.2 shows the spectra from one such junction on $NaFe_{0.98}Co_{0.02}As$. Instead of a conductance enhancement at low bias voltages ($\pm$ 20 mV), dI/dV shows a depression. At the lowest temperature (blue curve), peaks corresponding to the two superconducting gaps are clearly visible. However, the tunnel

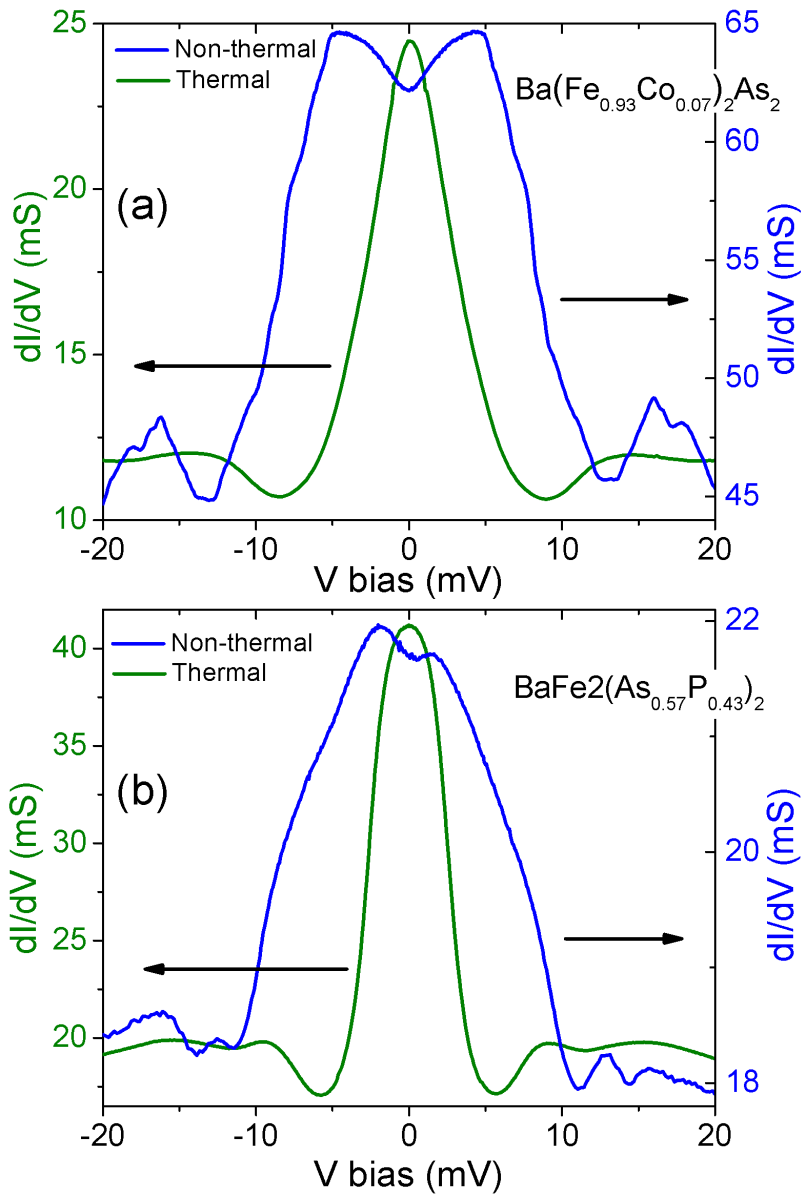

Figure 5.1: Thermal (green) and non-thermal (blue) point contact spectra for (a) $Ba(Fe_{0.93}Co_{0.07})_2As_2$ and (b) $BaFe_2(As_{0.57}P_{0.43})_2$. For the green curves, dI/dV at 0 mV is more than twice the dI/dV at 20 mV, indicating that the junction is impacted by thermal heating that is driving the superconductor normal. The blue curves are provided for comparison, the BTK fits to them have been shown previously in Figure 3.5 (a) and Figure 3.12 (b) respectively.

junction is of a poor quality since the drop in the conductance when $V < \Delta$ is only about 5%. It is difficult to fit such a spectrum to the BTK theory.

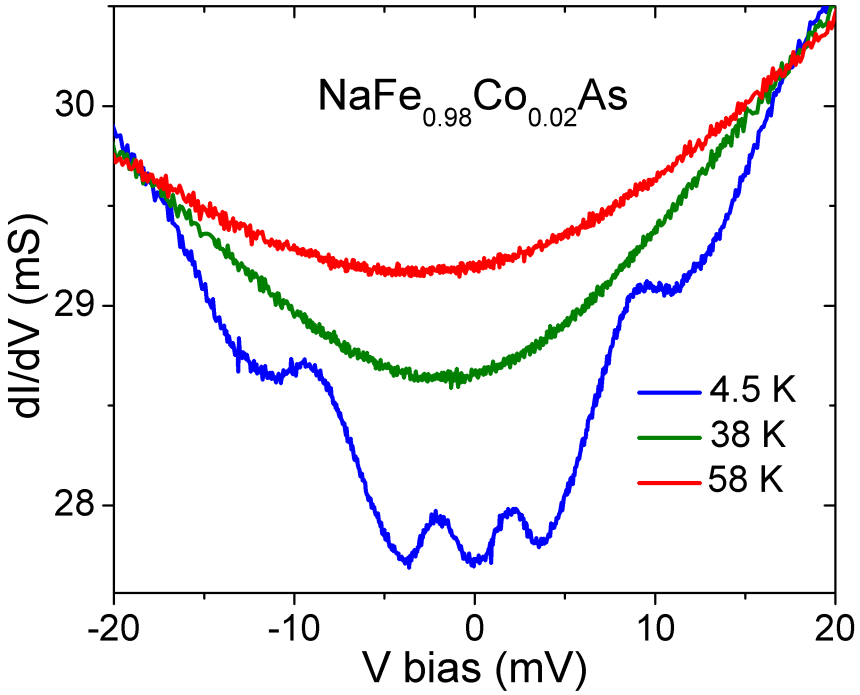

Figure 5.2: Tunneling like spectrum on $NaFe_{0.98}Co_{0.02}As$. At the lowest temperature (blue curve), peaks corresponding to the two superconducting gaps are clearly visible. However, the tunnel junction is of a poor quality since the drop in the conductance when $V < \Delta$ is only about 5%.

5.2 PCS spectra on correlated materials

There is no BTK like theory that can be used to differentiate between thermal and non-thermal point contact junctions on correlated materials. However, heating causes certain tell-tale signs that can be easily spotted by performing some diagnostics.

5.2.1 dV/dI tracks the bulk resistivity in the thermal limit

For junctions in the thermal regime, there is a strong resemblance between the temperature dependent bulk resistivity $R(T)$ and the voltage dependent point contact resistance dV/dI [119].

Figure 5.3 shows $R(T)$ and dV/dI for two soft point contact junctions on $BaFe_2As_2$. Both junctions are constructed in the exact same way. First, 50Å AlO_x is sputtered on our crystals to act as an insulating barrier and then using Ag paint as a counter electrode, channels are introduced for current transport by fritting [56] across the oxide layer. For junction 2 in Figure 5.3 (b) (black solid curve), larger channels are opened for current transport as opposed to the junction 1 in Figure 5.3 (b) (blue dashed curve), as is evident by their resistances at zero bias (16Ω vs. 40Ω). Consequently, junction 2 is in the thermal limit while junction 1 is not.

The resistance of $BaFe_2As_2$ always increases with rising temperature, and a gradient change occurs at the magnetostructural transition. dV/dI for a junction dominated by heating effects should therefore increase with rising voltage, as a higher voltage would correspond to more heating in the junction. That is exactly what junction 2 in Figure 5.3 (b) shows. The kink that occurs at ~ 52 mV corresponds to the junction being heated across the magnetostructural transition. On the other hand, junction 1 shows a completely different scenario. dV/dI actually decreases with an increasing voltage from 0 to ~ 70 mV. There is a bigger chance of heating up the junction at larger bias voltages, but dV/dI starts to decrease again at ~ 198 mV and keeps sloping down till our largest bias value, which is 225 mV for this junction. Similar behavior is observed in $SrFe_2As_2$ and $CaFe_2As_2$ which are biased up to 270 mV and 200 mV and still show a decreasing dV/dI.

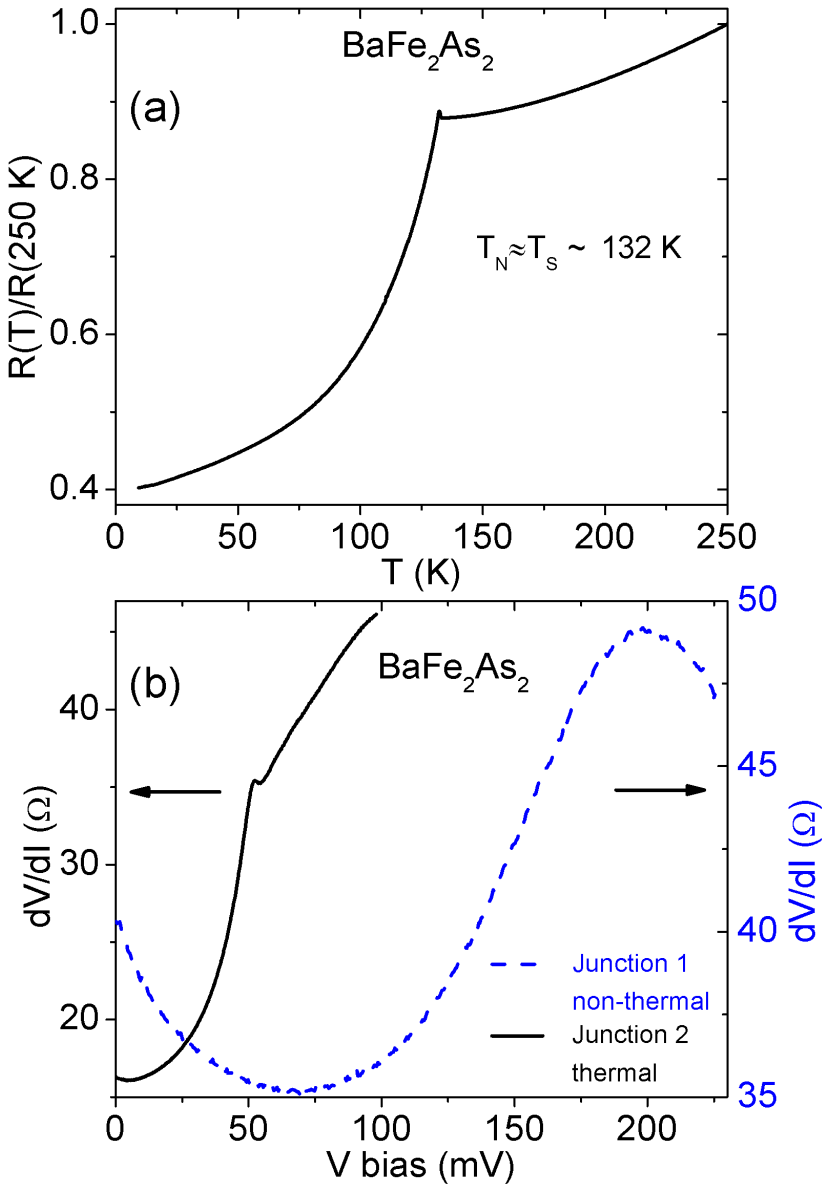

Figure 5.3: (a) Resistance vs. Temperature for $BaFe_2As_2$. The bulk resistance always rises with an increase in temperature. A gradient change occurs as the magnetostructural transition is crossed. (b) dV/dI for two junctions on $BaFe_2As_2$. Junction 2 is in the thermal limit and follows the functional form of the bulk resistivity (black solid curve, taken at 7.6 K). The junction resistance rises with increasing voltage and there is a kink at $\sim$ 52 mV corresponding to being heated across the magnetostructural transition. Junction 1 behaves very differently from bulk resistivity (blue dashed curve, taken at 2.0 K). The junction resistance decreases with an increasing voltage from 0 to $\sim$ 70 mV, and again for voltages larger than $\sim$ 198 mV. A lack of agreement between bulk resistivity and dV/dI indicates that the junction 1 is free of heating effects.

For thermal junctions, the zero bias conductance (ZBC, dI/dV at V=0) curve follows a similar functional form to the bulk resistivity. Figure 5.4 (a) shows ZBC curves for the junctions 1 and 2 from Figure 5.3.

For junction 1 (non-thermal), the curve has a turning point at $\sim$ 175 K, marking the onset temperature of the conductance enhancement. At low temperatures, ZBC starts to fall corresponding to the development of split conductance peaks in dI/dV. We have previously discussed the features of non-thermal PCS junctions on $BaFe_2As_2$ in Chapter 4.

For junction 2 (thermal), the ZBC is always decreasing with rising temperature, and there is a gradient change close to the magnetostructural transition, as is observed in the bulk resistivity. The ZBC curves of some joule heated junctions show a greater similarity with the bulk resistivity than others. This is probably determined by how thermal as opposed to non-thermal a junction is. In Figure 5.4 (b), we show ZBC curves for two more junctions: junction 3 (blue dashed curve) follows the bulk resistivity very closely and junction 4 (green curve) lies between the extremes displayed by the thermal and non-thermal limits. The vertical red dashed lines in Figure 5.4 (a), (b) point out the temperature at which the magnetostructural transition occurs.

Figure 5.5 plots dV/dI for junction 4 (green curve). dV/dI of the thermal junction 2 is included for comparison (black curve). As mentioned above, the conduction regime of junction 4 lies between those of junctions 1 and 2. For the non-thermal junction 1, there is a turning point at $\sim$ 70 mV. For junction 4, thermal smearing brings the turning point down to $\sim$ 28 mV. The thermal junction 2 does not have a turning point at all. The thermal junction 2 has a kink at $\sim$ 52 mV that corresponds to the junction being heated across the magnetostructural transition. Junction 4 has a broad shoulder with a gradient change instead. Junction 1 has a second turning point at $\sim$ 198

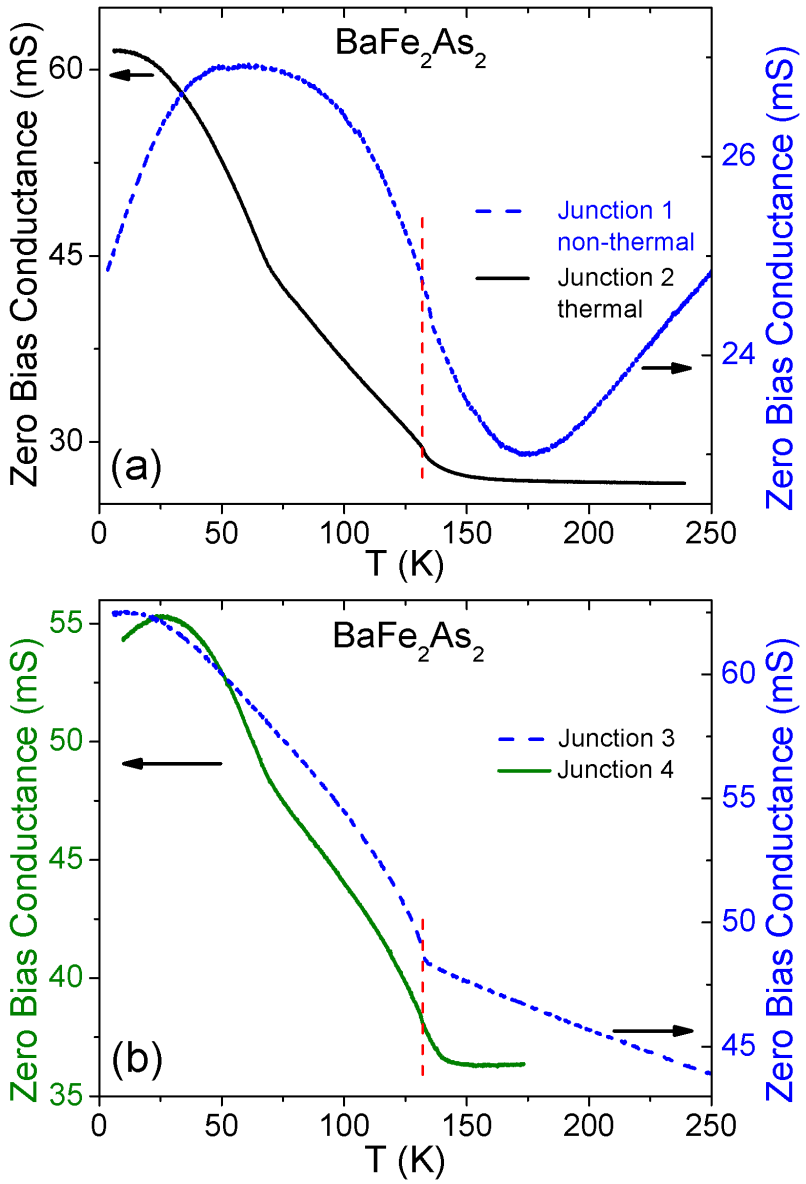

Figure 5.4: (a) The ZBC curve for junctions 1 and 2 from Figure 5.3 (b). Junction 2 (thermal, black solid curve) follows the trend of the bulk resistivity, while junction 1 (non-thermal, blue dashed curve) does not. (b) ZBC curves for two additional junctions. Junction 3 (blue dashed curve) follows the bulk resistivity very closely and junction 4 (green curve) lies between the extremes displayed by the thermal and non-thermal limits. The vertical red dashed lines in (a) and (b) mark the magnetostructural transition temperature.

mV, junction 4 has a similar feature at $\sim$ 137 mV. Overall, while junction 4 retains some spectroscopic information, it is also showing distinct signs of being impacted largely by thermal heating effects.

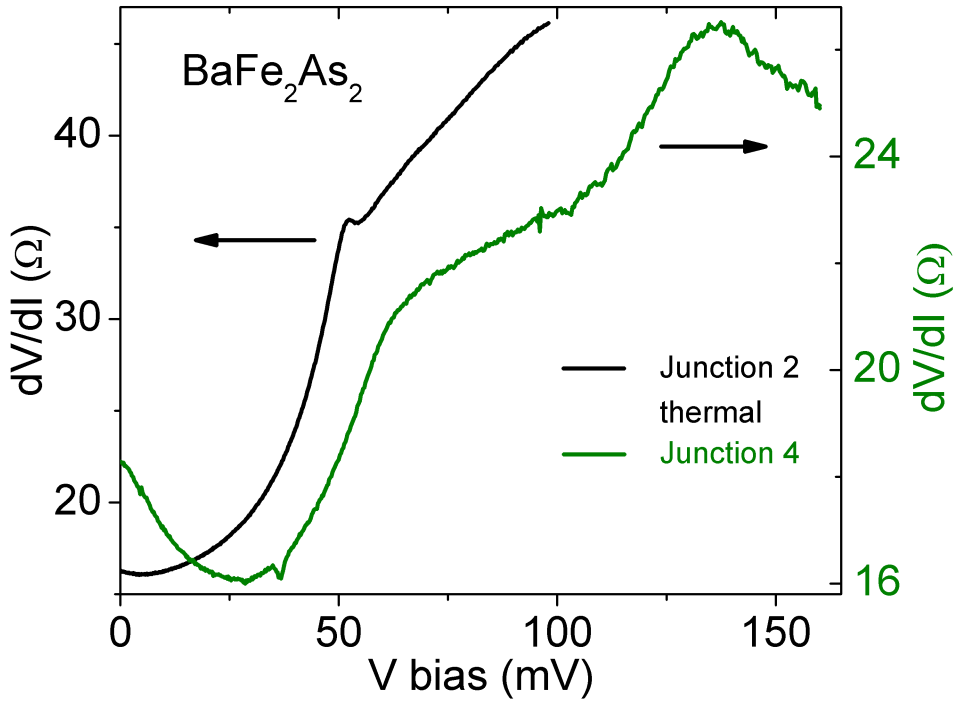

Figure 5.5: dV/dI for junction 4 (green curve). dV/dI of the thermal junction 2 is included for comparison (black curve). Junction 4 shows signs of thermal heating effects. Junction 2 has a kink at $\sim$ 52 mV, corresponding to being heated across T_S. This feature shows up as a broad shoulder with a gradient change for junction 4.

5.2.2 PCS junctions constructed by various techniques show similar spectra

Identical PCS spectra should be obtained from needle-anvil and soft PCS methods. Figure 5.6 presents spectra on $Fe_{1.13}Te$ obtained via these two techniques. Very similar curves are obtained.

For the insulating layer in soft PCS, we use either aluminum oxide or germanium, and obtain similar results. This shows that our soft point contact

junction setup is not interfering with the intrinsic properties of the material under study.

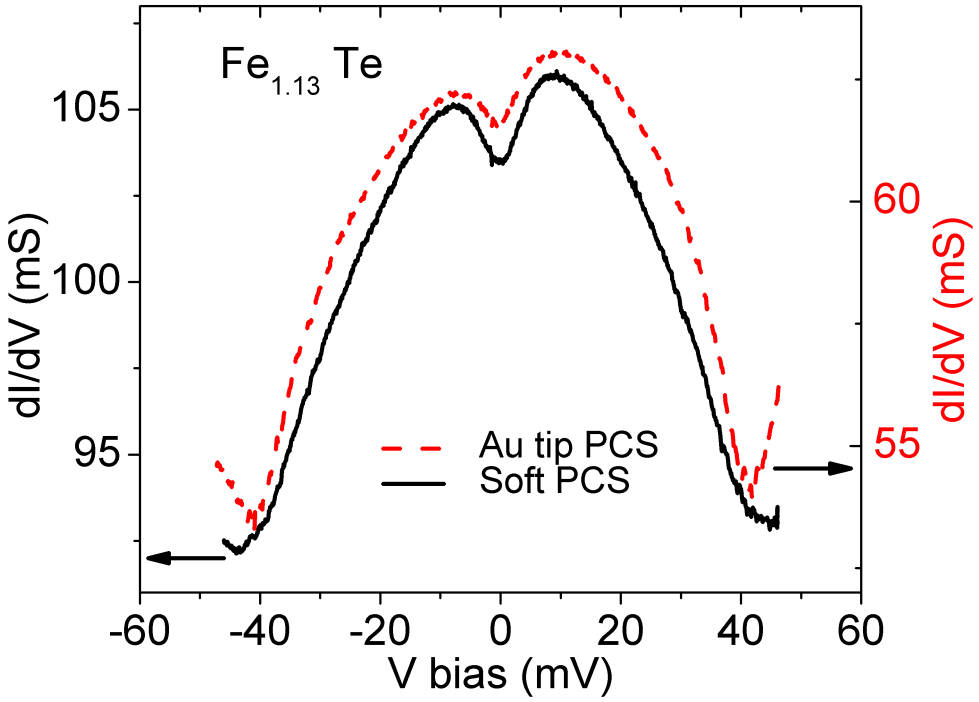

Figure 5.6: Needle-anvil PCS with a Au tip (red dashed curve, taken at 4.0 K) and soft PCS (black solid curve, taken at 6.84 K) on $Fe_{1.13}Te$ show very similar spectra.

5.2.3 Thermal limit PCS on magnetic compounds detects the magnetic transition

There is a tell-tale sign of heating effects for PCS on magnetic compounds, corresponding to their magnetic transition temperature. When the biasing voltage becomes large enough to increase the local temperature of the junction across the magnetic transition temperature, a distinct non-linearity shows up as a turning point in dV/dI [120, 121]. (For the thermal limit junction shown in Figure 5.3 (b), this turning point occurs at $\sim$ 52 mV). The turning point occurs at increasingly lower bias voltages as the ambient temperature is increased. Once the ambient temperature is equal to the

magnetic transition temperature, the peak in dV/dI occurs at 0 mV. By just looking at our low temperature data for $BaFe_2As_2$ in Figure 4.1 (a), it may be speculated that the maximum in dV/dI at $\sim$ 162 mV is the sample crossing the magnetic transition. However, had that been the case, this maximum would have disappeared for dV/dI curves taken at $T > T_N$. As Figure 5.7 (a) shows, the peak in dV/dI is present at T_N and has moved inwards to 94 mV. It eventually disappears at 177 K. Therefore, it cannot possibly correspond to the junction getting warm enough to cross the magnetic transition. We also plot the peak position as a function of temperature in Figure 5.7 (b).

5.2.4 Converting dI/dV(V, low T) into zero bias conductance dI/dV(0 mV, T) by using the Lorentz number

Another check for thermal PCS junctions is to compare the dI/dV(V, low T) curve with the zero bias conductance curve, dI/dV(0 mV, T). The local temperature in a thermal junction is related to the bias voltage by $T_{max}^2 = T_{bath}^2 + V^2/4L$ where L is the Lorentz number of the compound [119]. In such a scenario, there is a substantial overlap between ZBC and dI/dV, as shown for UPt_3 in [119]. For ballistic junctions, ZBC and dI/dV may superficially have the same shape but they will no longer have any overlap (for e.g. Fig. 1 in [122]). In Figure 5.8 (a) we compare these two quantities for the $BaFe_2As_2$ junction whose temperature evolution is shown in Figure 4.1 (a). The red dashed curve uses the value of L for $BaFe_2As_2$ reported in [123]; L = 2.44 x 10^{-8} $W\ \Omega\ K^{-2}$. Since the L reported in [123] is for low temperature and L may vary with temperature, we also compare dI/dV and ZBC for L = 2.1 x 10^{-7} $W\ \Omega\ K^{-2}$, that forces 170 mV to correspond to 175 K (blue dotted curve). There is still no quantitative agreement between dI/dV and ZBC since the maximum and minimum values for the two curves are quite

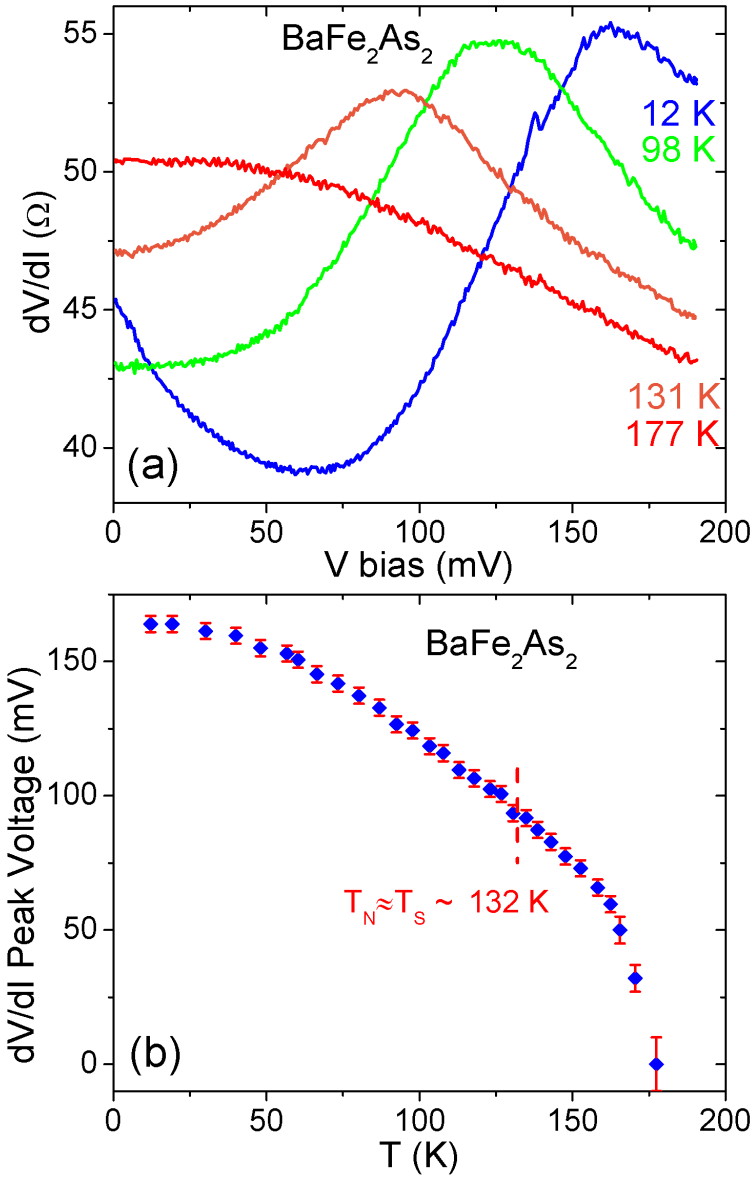

Figure 5.7: (a) As the temperature is increased, the peak in dV/dI moves to lower bias voltages. However, it does not disappear at $T_N \sim 132$ K, and survives until 177 K. (b) The bias voltage at which the peak in dV/dI occurs as a function of temperature. Had the peak been due to heating the junction across T_N, it would have disappeared at T_N, as shown for thermal limit PCS on magnetic materials [121].

different. The lack of any overlap for either value of L shows that our junction is not in the thermal limit.

In Figure 5.8 (b) we compare the dI/dV curve with the ZBC curve for junction 2 (from Figure 5.3 (b) and Figure 5.4 (a)). The kink at the magnetostructural transition occurs at the same conductance value in both curves, providing evidence for the thermal nature of the junction. Voltage has been converted into temperature using L = 3.5 x 10^{-8} $W\ \Omega\ K^{-2}$. The lack of a fit at lower bias voltages/lower temperatures implies that either L is varying with temperature or the junction is not completely in the thermal regime.

The striking similarity between the dI/dV and the ZBC curves for junctions not impacted by heating effects implies that the scattering processes responsible for our spectra behave in a similar manner under temperature and voltage. An existing example of this is PCS on Kondo systems, where the scattering has a log dependence on both temperature and voltage [97]. Figure 1 in [124] shows that for ballistic PCS on Kondo systems, dV/dI and R(T) have the same functional form.

5.2.5 Different bulk resistivity but similar dI/dV spectra for Fe-pnictides vs. Fe-chalcogenides

The Fe-pnictides and the Fe-chalcogenides show very different resistivity curves [Figures 4.5 (b), 4.6 (b), and 4.7 (b)] and may be classified as bad metals [16]. Upon cooling the $Fe_{1.13}Te$ from room temperature to T_S, the resistance is observed to increase, while for the $BaFe_2As_2$, the resistance is seen to decrease. Below T_S, the resistance decreases much more quickly with decreasing temperature for $Fe_{1.13}Te$ than for $BaFe_2As_2$. Despite differences in their $R(T)$, the two families show similarly shaped dI/dV spectra. This is further evidence that our junctions are not in the thermal regime and that

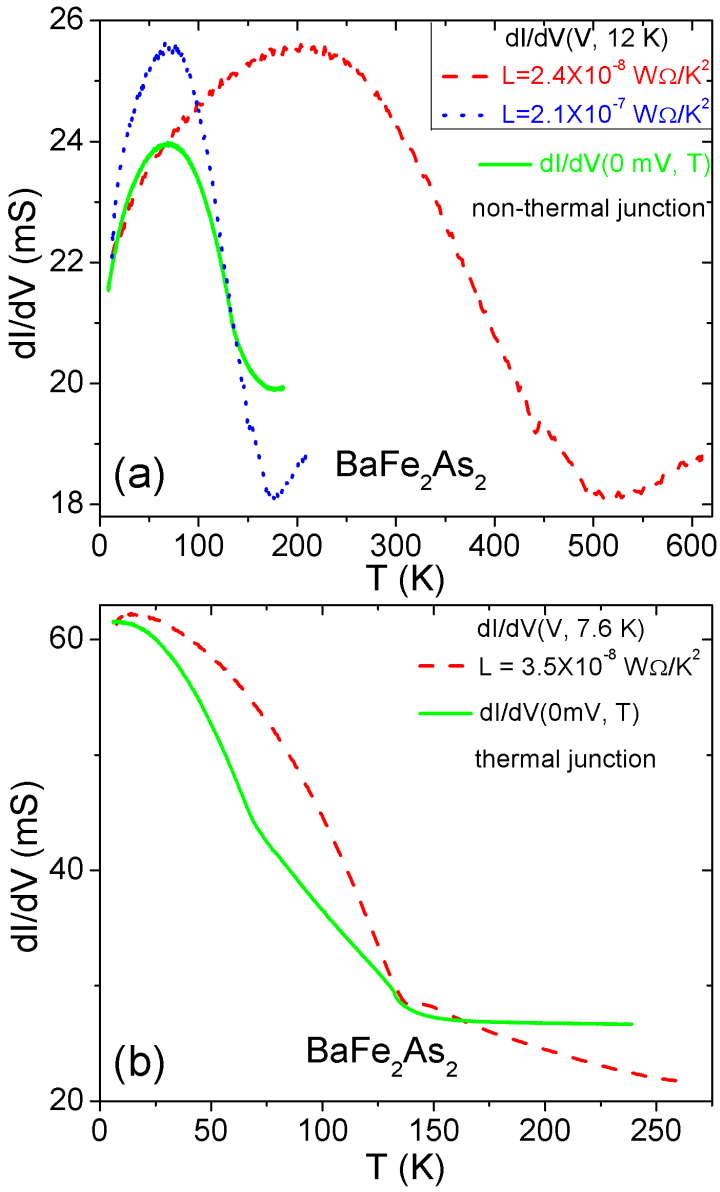

Figure 5.8: Comparing the ZBC and dI/dV curves for $BaFe_2As_2$. (a) The red dashed and blue dotted curves are the low temperature dI/dV curve plotted on a temperature scale using $T^2_{max} = T^2_{bath} + V^2/4L$. For red curve L = 2.44 x 10^{-8} $W\ \Omega\ K^{-2}$, for blue curve L = 2.1 x 10^{-7} $W\ \Omega\ K^{-2}$. A lack of agreement between the ZBC (solid green curve) and these extrapolated dI/dV curves shows that the junction is not in the thermal limit. (b) For a thermal limit junction on $BaFe_2As_2$, the kink in the dI/dV spectrum occurs at the same conductance value at which the ZBC crosses the magnetostructural transition, and the two curves may be made to overlap using L = 3.5 x 10^{-8} $W\ \Omega\ K^{-2}$. The lack of a fit at lower bias voltages/lower temperatures implies that either L is varying with temperature or the junction is not completely in the thermal regime.

the same scattering mechanisms are at work in both the Fe-chalcogenides and the Fe-pnictides.

To summarize, via soft PCS, we can construct junctions both highly impacted by thermal heating effects and junctions free of heating effects. All the data presented and discussed in the thesis has been taken on junctions free of heating. For superconducting samples, fits to BTK theory can separate the good spectra from the bad. For non-superconducting crystals, our diagnostics provide ample evidence that the junctions are not in the thermal limit: (a) No agreement of bulk resistivity with dV/dI (b) No indication that the low temperature curves cross the magnetic transition when biased to high voltages (c) No quantitative agreement between the dI/dV and the ZBC curves (d) dI/dV spectra of similar functional form obtained from the Fe-chalcogenides and Fe-pnictides, who have different temperature dependence of bulk resistivity. In addition, since Au tip and soft PCS junctions show similar spectra, our features are not an artifact of our junction fabrication technique.

CHAPTER 6

MAGNETIC FIELD AND STRESS EFFECTS

Previously we have shown that point contact spectroscopy in the normal state of $BaFe_2As_2$ detects evidence for orbital fluctuations. In this chapter we present data taken on crystals in the presence of (1) an external magnetic field and (2) compressive stress, both applied along the a-b plane. We discuss how these factors change the properties of the crystal and impact our dI/dV spectra.

6.1 Magnetic Field

Magnetic field applied along the a-b plane of $BaFe_2As_2$ results in the partial detwinning of the crystal [125]. Figure 6.1 shows the bulk resistivity of $BaFe_2As_2$ when a magnetic field of 9 T is applied along the a-b plane. The crystal was first cooled in zero field (blue curve) and then warmed with the 9 T applied field (red curve). At high temperatures, the magnetic field has no effect on the bulk resistivity. At $\sim$ 178 K, (well above the magnetostructural transition that occurs at $\sim$ 132 K), the resistivities start to diverge. The arrow in the figure is pointing this out. Detwinned $BaFe_2As_2$ shows a resistive anisotropy in the normal state [88] and the magnetic field is helping us in picking it up. The temperature at which the magnetic field starts impacting the bulk resistivity is the same temperature below which PCS picks up a conductance enhancement, as we discussed in Chapter 4.1.1.

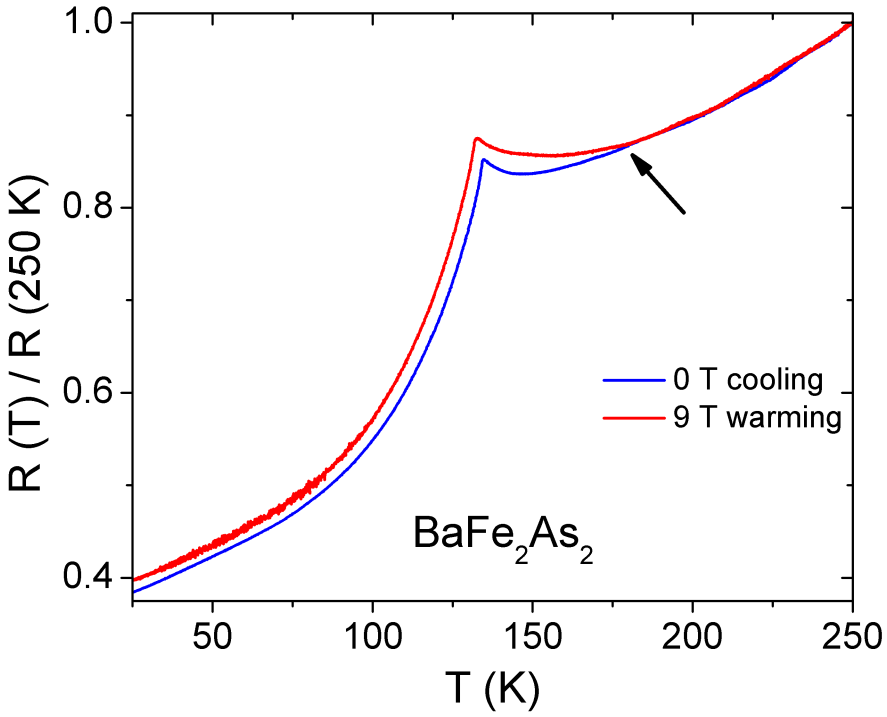

Figure 6.1: Bulk resistivity of $BaFe_2As_2$ when a magnetic field of 9 T is applied along the a-b plane (red curve). At $\sim$ 178 K, the resistivity in the presence of the field starts diverging from the resistivity measured without any applied field.

6.1.1 Magnetic Field Induced Asymmetry in dI/dV

In Figure 6.2 (a) we show how an external magnetic field changes the low temperature dI/dV spectra of $BaFe_2As_2$. The field is applied parallel to the a-b plane of the crystal. In Figure 6.2 (b), the direction of the applied field is reversed (anti-parallel, rotated by 180^0).

In the absence of applied field (blue curve), we see a dip at zero bias and conductance peaks at $\sim \pm$ 72 mV. The double peak feature is superimposed on a parabolic background. This curve is very similar to the dI/dV spectra on $BaFe_2As_2$ shown earlier in Figure 4.1 (a).

As the magnetic field is turned on, a strong asymmetry develops in the data [Figure 6.2 (a)]. dI/dV for positive voltage bias becomes much larger than the dI/dV for negative voltage bias. A larger magnetic field causes more asymmetry in the data.

Without applied field, the parabolic background starts dominating the spectra from $\sim \pm$166 mV. With field, for positive bias, this stays the same, but for negative bias, the upturn starts occurring at smaller and smaller voltages. At a field of 9 T (red curve), the upturn happens at $\sim$ -84 mV.

When the direction of the applied field is reversed, the induced asymmetry in the data is also reversed [Figure 6.2 (b)]. Now the dI/dV for negative voltage bias becomes larger than the dI/dV for positive voltage bias. Also, with increasing field, the upturn voltage for positive bias moves in while that for negative bias stays the same. In a sense, the spectra for parallel and anti-parallel magnetic fields are mirror images of each other.

dI/dV for V $>$ 165 mV behaves in a peculiar manner. In Figure 6.2 (b), from 0–-3 T, the dI/dV in this voltage range decreases slowly, before falling sharply at -4 T, and then shooting back up at -5 T. With further increase in

field, dI/dV keeps rising but much more slowly. In Figure 6.2 (a), the exact same behavior is observed for the voltage range V < -165 mV.

In Figure 6.3, we explore this phenomenon by sweeping the field and keeping the bias voltage fixed at 0 mV (blue solid curve), 200 mV (red dotted curve), and -200 mV (green dashed curve). The field is swept from -9 T to 9 T at a rate of 0.5 T per minute. At 0 mV, the parallel and anti-parallel field suppresses the dI/dV in an identical manner. At ±200 mV, a sharp drop and rise in the dI/dV is detected between 3 T and 5 T.

Figures 6.4 and 6.5 compare the temperature evolution of the dI/dV spectra with and without magnetic field for a different junction on $BaFe_2As_2$. For this junction, at low temperature [blue curve in Figure 6.4 (b)], a field of 1 T causes more asymmetry than a field of 3 T does for Figure 6.2 (a). However, qualitatively, the features are the same, with the applied field causing the dI/dV at positive bias voltage to become larger than the dI/dV at the negative bias voltage.

As the temperature is increased, the asymmetry caused by the magnetic field becomes smaller. After 112 K [green curve in Figure 6.5 (b)], the spectra at 0 T and 1 T are nearly identical.

6.1.2 Magnetic Field Induced Fluctuations in dI/dV

In the previous section we have shown that applied in-plane magnetic field causes an asymmetry to develop in the dI/dV spectra of $BaFe_2As_2$. However, for some of our junctions, such a behavior is not detected and instead the field causes the dI/dV signal to develop fluctuations around the 0 T value. We now present and discuss such spectra.

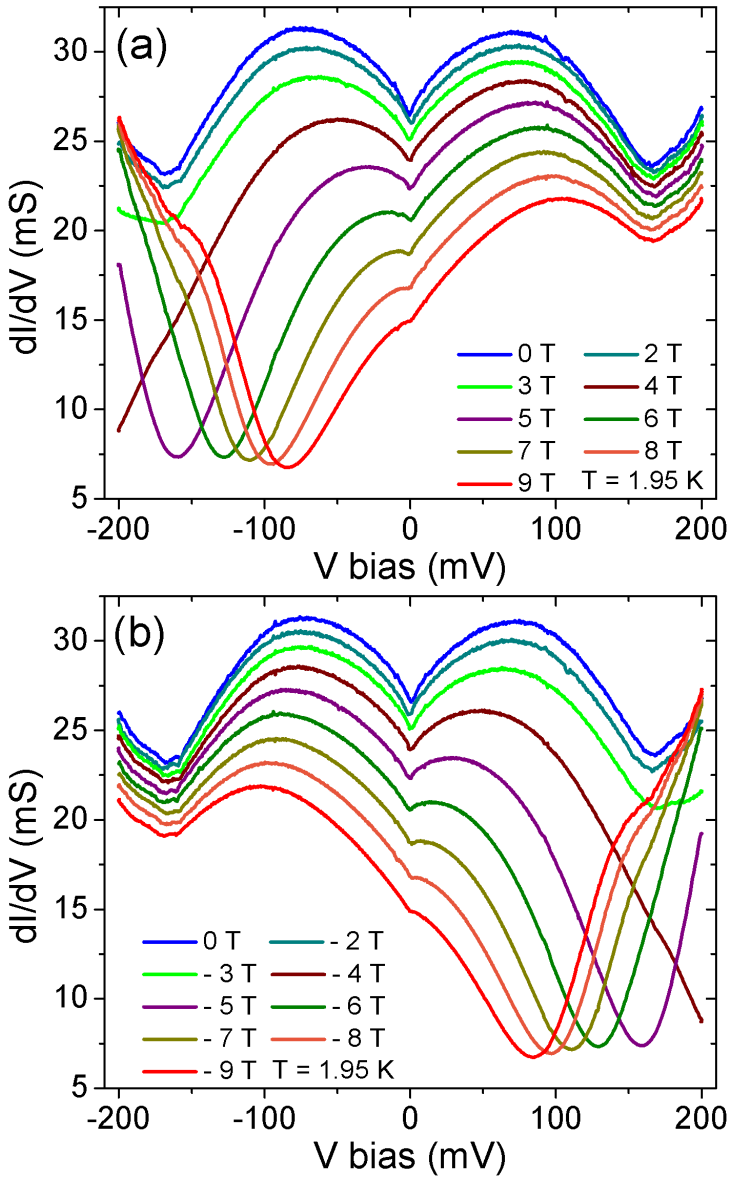

Figure 6.2: Low temperature dI/dV of $BaFe_2As_2$ when a magnetic field is applied (a) parallel and (b) anti-parallel to the a-b plane. The magnetic field causes a strong asymmetry to develop in the curves. The spectra for the parallel and anti-parallel fields are mirror images of each other.

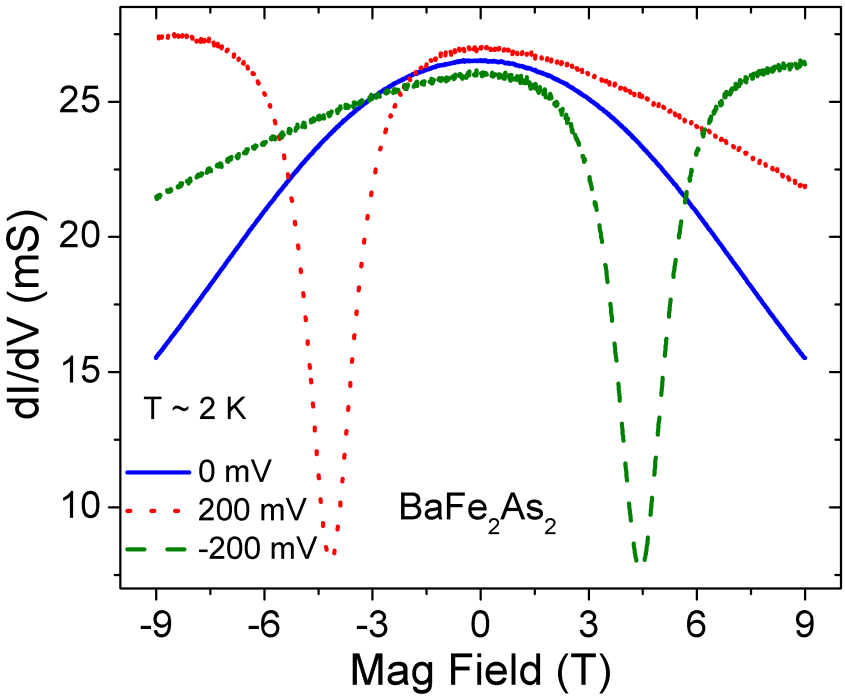

Figure 6.3: dI/dV of $BaFe_2As_2$ at fixed bias voltages of 0 mV, 200 mV, and -200 mV while sweeping the magnetic field from -9 T to 9 T. At 0 mV, the parallel and anti-parallel field suppresses the dI/dV in an identical manner. At $\pm$200 mV, a sharp drop and rise in the dI/dV is detected between 3 T and 5 T.

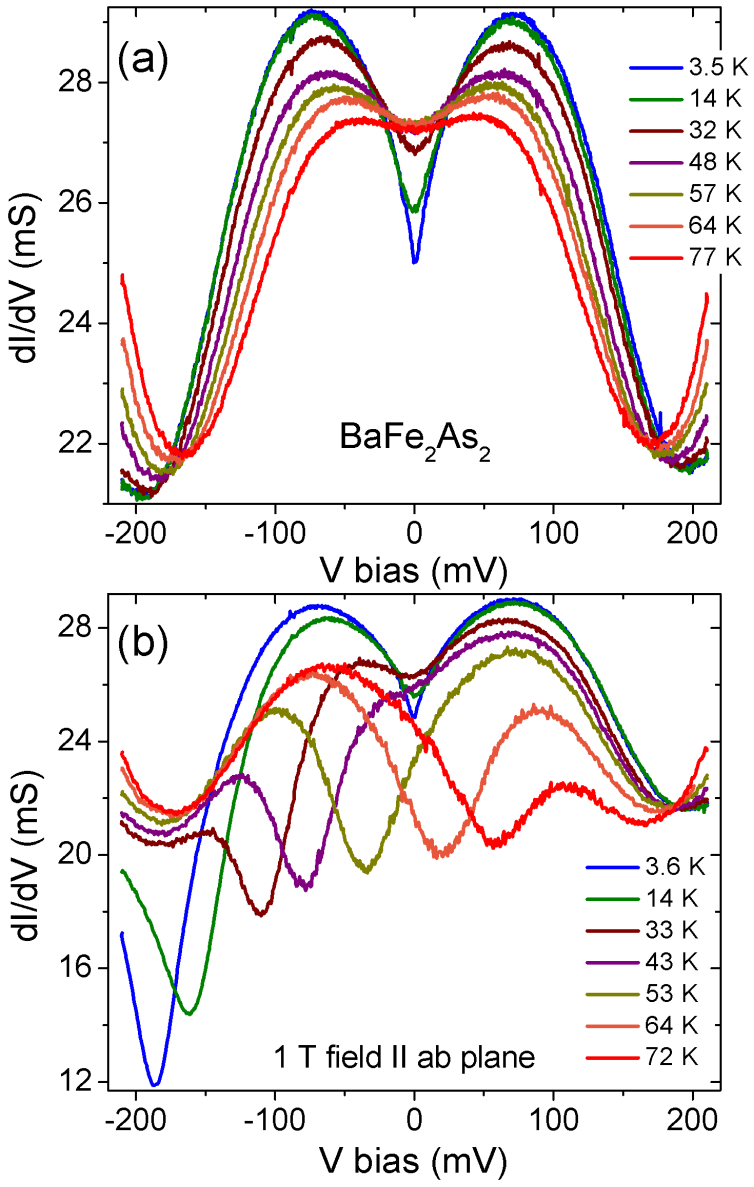

Figure 6.4: Temperature evolution of the dI/dV spectra for $BaFe_2As_2$ taken at (a) 0 T and (b) 1 T. As the temperature is increased, the asymmetry caused by the magnetic field becomes smaller.

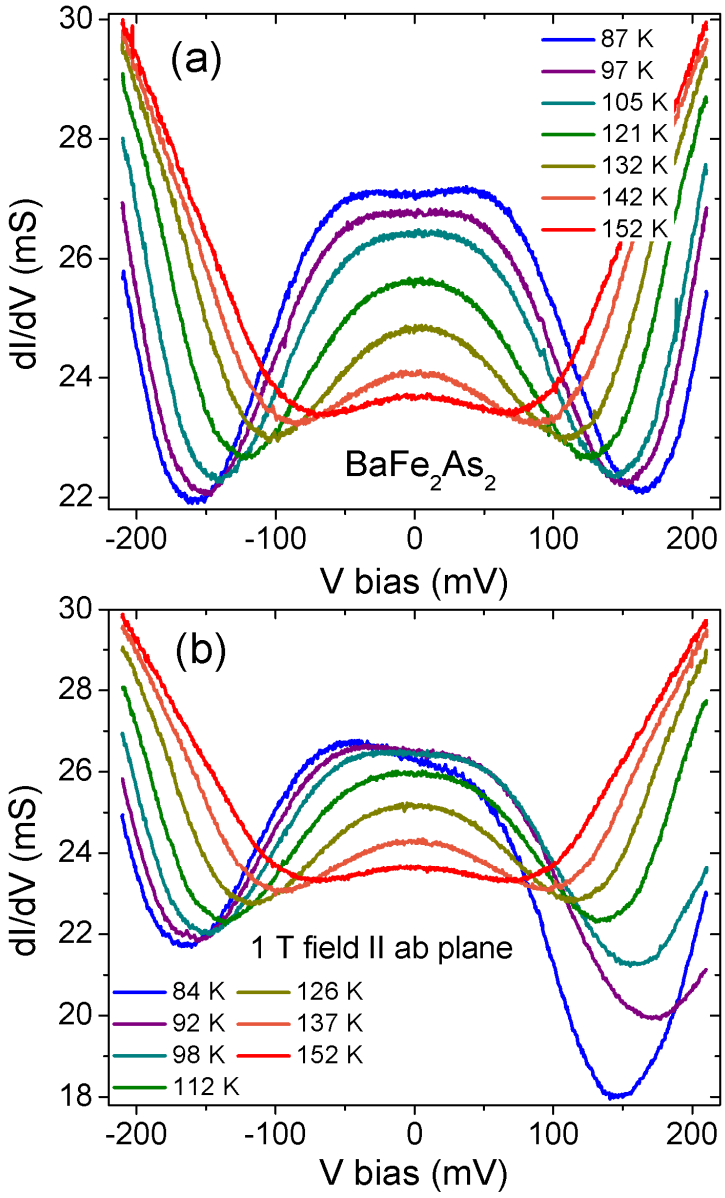

Figure 6.5: Continuing from Figure 6.4; the temperature evolution of the dI/dV spectra for $BaFe_2As_2$ taken at (a) 0 T and (b) 1 T. After 112 K (green curve in (b)), the magnetic field of 1 T causes a negligible effect on the curves.

Figure 6.6 (a) shows dI/dV at 5.0 K for a PCS junction on $BaFe_2As_2$ with applied fields of 0 T (black solid curve) and 9 T (red dashed curve). The two curves are nearly identical. The zero bias conductance (ZBC) curve of this junction is shown in Figure 6.6 (b). In the absence of the magnetic field, the ZBC (black curve) behaves as expected and shown previously in Figure 4.5 (b). However, once the field is switched on, the ZBC (red curve) becomes noisy and starts fluctuating around the dI/dV value at 0 T. The fluctuations increase in amplitude substantially at $\sim$ 175 K. The black arrow in the figure is pointing this out. 175 K is significantly larger than the magnetostructural transition temperature ($\sim$ 132 K) and is the same temperature below which PCS detects orbital fluctuations in $BaFe_2As_2$, as discussed in Chapter 4. From 175 K down to 50 K, the fluctuations in the ZBC stay strong, after which their amplitude starts to decrease. Below $\sim$ 25 K, the 9 T and 0 T ZBC curves are almost identical, which explains why the dI/dV curve taken at 5 K also shows no difference when a magnetic field is introduced.

Figure 6.7 shows dI/dV at 85 K for a different junction on $BaFe_2As_2$. The fluctuations in dI/dV induced by the 9 T magnetic field are clearly visible.

The data shown in Figure 6.8 is from a junction whose spectra shows some thermal smearing effects. We can deduce this by looking at the 0 T ZBC curve in Figure 6.8 (b) and comparing it with the thermal and non-thermal junctions previously discussed in Chapter 5.2.1. The main effect of the thermal broadening on this junction is that the low temperature conductance peaks are smeared and the corresponding dip at zero bias is shallower.

The ZBC in the presence of magnetic field starts showing fluctuations close to 175 K, the arrow in Figure 6.8 (b) is pointing this out. At low temperatures, the fluctuations are much weaker.

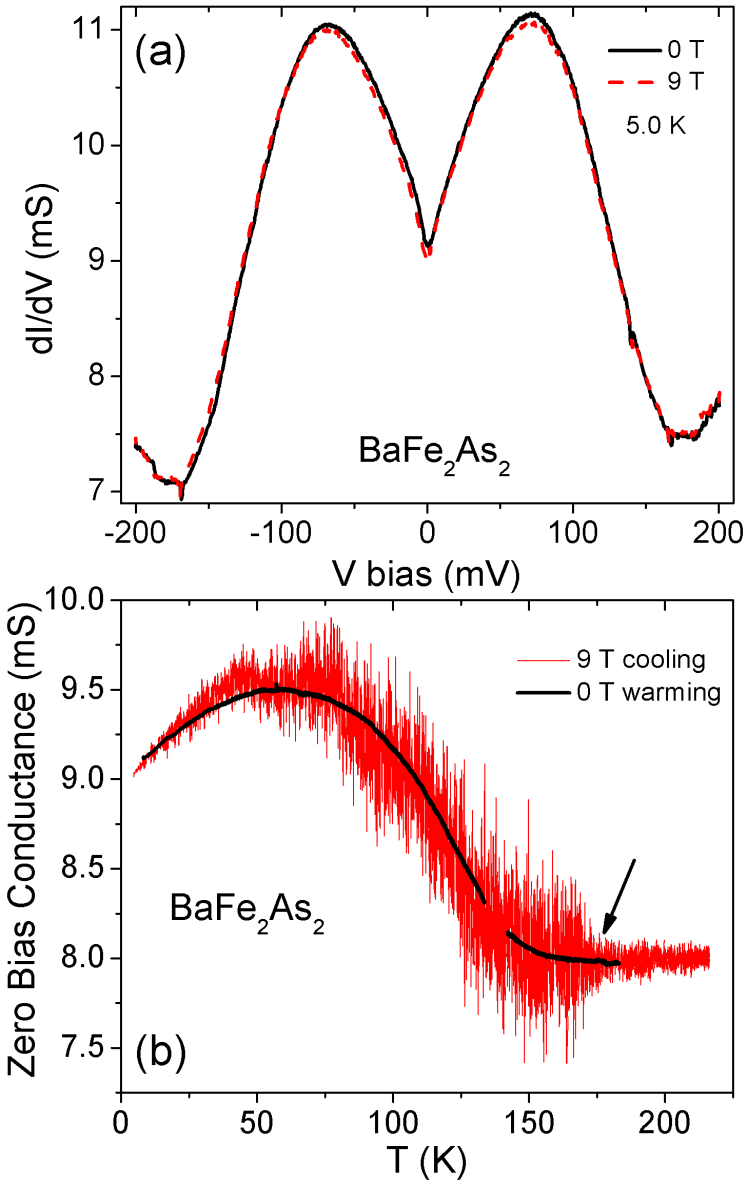

Figure 6.6: (a) dI/dV at 5.0 K for a PCS junction on $BaFe_2As_2$ with applied fields of 0 T (black solid curve) and 9 T (red dashed curve). The two curves are nearly identical. (b) Zero bias conductance for the same junction. Once the field is switched on, large fluctuations develop in the ZBC below $\sim$ 175 K. The arrow in the figure points this out. These fluctuations die out below $\sim$ 25 K, making the 0 T and 9 T curves similar.

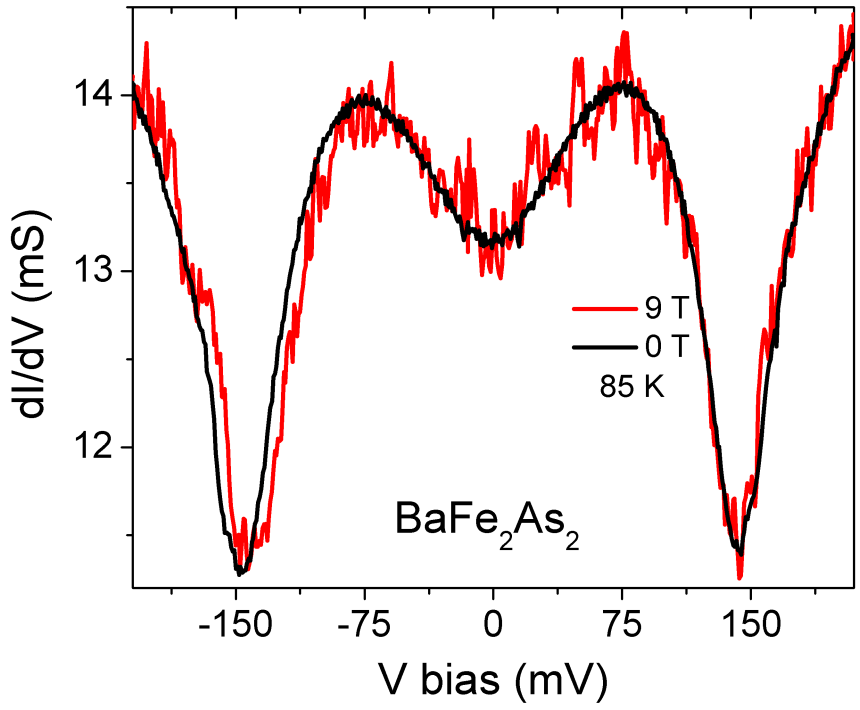

Figure 6.7: dI/dV at 85 K for a PCS junction on $BaFe_2As_2$. The 9 T magnetic field causes the conductance to fluctuate around the 0 T conductance value.

Figure 6.8 (a) shows that at 4.0 K, the magnetic field does not impact the dI/dV curve, but at 65 K, the magnetic field clearly causes the dI/dV curve to fluctuate around its 0 T value.

To summarize, an in-plane magnetic field impacts the conductance spectra on $BaFe_2As_2$ in one of two ways: (1) either it causes an asymmetry to develop between the dI/dV detected at the positive and negative bias voltage, (2) or it causes dI/dV to fluctuate around its 0 T value below $\sim$ 175 K. The fluctuations are not detected at liquid He temperatures, they seem to disappear around 25 K.

We are not clear as to why the magnetic field affects our spectra in such unique ways. The size of a single domain in $BaFe_2As_2$ is on the order of 10 μm [91, 125]. This means that our point contact junction comprises of multiple domains of different orientations. Once an in-plane magnetic field is applied, the twin boundaries move, changing the size and orientation of some of the domains. The antiferromagnetic ordering in $BaFe_2As_2$ is collinear, with antiferromagnetic spin order along the a axis and ferromagnetic spin order along the b axis. Thus the magnetic susceptibility is larger for a field pointing along the b axis as opposed to the field pointing along the a axis. The resulting difference in energy causes the twin boundaries to move. However, it is unlikely that the domain size or orientation influences the PCS spectra.

At the very least, the asymmetry induced by the magnetic field provides more evidence that we can construct point contact junctions that are free of heating artifacts. Junctions impacted by heating show similar spectra for positive and negative biases. Since joule heating is equal to V^2/R, the sign of the voltage bias does not matter.

Magnetic field effects on the PCS spectra merit more investigation. Two possible directions to follow are (1) rotating the field within the a-b plane, as

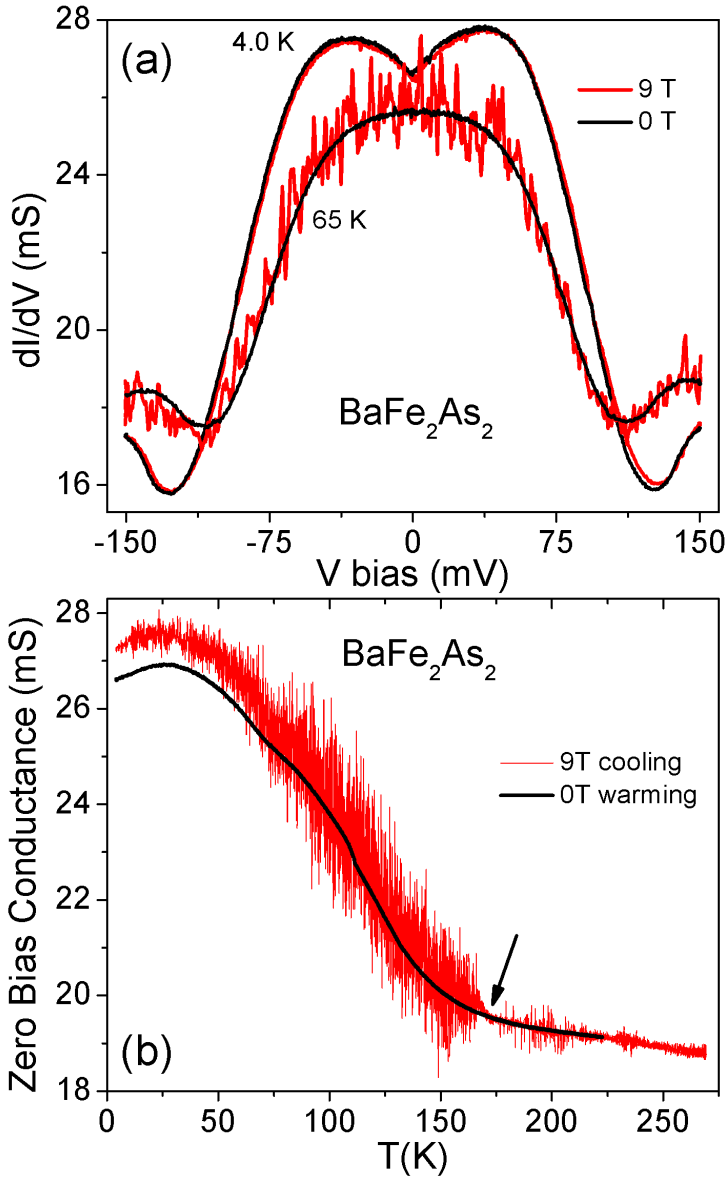

Figure 6.8: (a) At 4.0 K, the magnetic field does not impact the dI/dV curve, but at 68 K, the magnetic field clearly causes the dI/dV curve to fluctuate around its 0 T value. (b) ZBC for the same junction. The fluctuations set in close to 175 K, as pointed out by the arrow. At low temperatures, the fluctuations become weak.

well as rotating the field between the a-b plane and the c-axis (2) obtaining a frequency spectrum for the conductance fluctuations observed.

6.2 Compressive Stress

$BaFe_2As_2$ may be detwinned by cooling it through the tetragonal to orthorhombic structural transition temperature while a compressive stress is being applied. The shorter axis b gets aligned in the direction of the compressive stress, while the longer axis a is perpendicular to it. In most designs, the stress is applied by turning a screw that jams a flat surface into the a-b plane of the crystal [60].

On twinned $BaFe_2As_2$ crystals, ARPES detects orbital ordering below the structural transition temperature [104]. On detwinned crystals, the orbital ordering sets in well above the structural transition temperature. There is a large electronic nematic susceptibility in the crystals which is latching on to the applied stress. A small amount of stress is causing a large difference in the band structure.

For underdoped $Ba(Fe_{1-x}Co_x)_2As_2$, the structural transition precedes the magnetic transition. The derivative of the bulk resistivity shows peak-like features corresponding to the two transitions. Once stress is applied, the feature for the structural transition gets broadened out while that for the magnetic transition is unaffected [88]. The applied stress is already breaking the tetragonal symmetry in the normal state, and this rounds out the features corresponding to T_S.

On unstressed $Ba(Fe_{1-x}Co_x)_2As_2$ crystals, we have evidence that the conductance enhancement above the structural transition detected by PCS is caused by orbital fluctuations. Conducting the same experiment on stressed

crystals should be interesting. Stress is going to cause orbital ordering, rather than orbital fluctuations, to occur above the structural transition temperature.

Figure 6.9 (a) shows the dI/dV spectra on unstressed $Ba(Fe_{0.985}Co_{0.015})_2As_2$ while Figure 6.9 (b) is for when the crystal is under compressive stress. The unstressed spectra is very similar to what we has shown and discussed previously for $BaFe_2As_2$ [Figure 4.1 (a)]. $Ba(Fe_{0.985}Co_{0.015})_2As_2$ has the structural transition at $\sim$ 119 K and the magnetic transition at $\sim$ 117 K. PCS detects a conductance enhancement that survives well above these two transitions, and disappears close to 167 K.

The situation is remarkably different once stress is applied. The low temperature conductance peaks now occur at $\sim$ 12 mV as opposed to $\sim$ 60 mV seen for the unstressed crystal. The range of the conductance enhancement is $\sim \pm 70$ mV, compared to $\sim \pm 150$ mV in the absence of stress. Finally, the conductance enhancement does not survive into the normal state and disappears between 76 K and 92 K.

The PCS spectra on stressed $Ba(Fe_{0.985}Co_{0.015})_2As_2$ provides support to the hypothesis that the conductance enhancement detected by PCS in the normal state of the iron based superconductors is caused by orbital fluctuations.

At the moment, we cannot change the amount of stress applied in-situ. The crystal is locked in place with a plate pressing down on it at room temperature and then the probe is slowly cooled down. Consequently, the stressed and unstressed data are obtained from different junctions. The next experimental step is to design a setup that can change the stress level in-situ and on the same junction observe the change in dI/dV as the stress is increased/decreased.

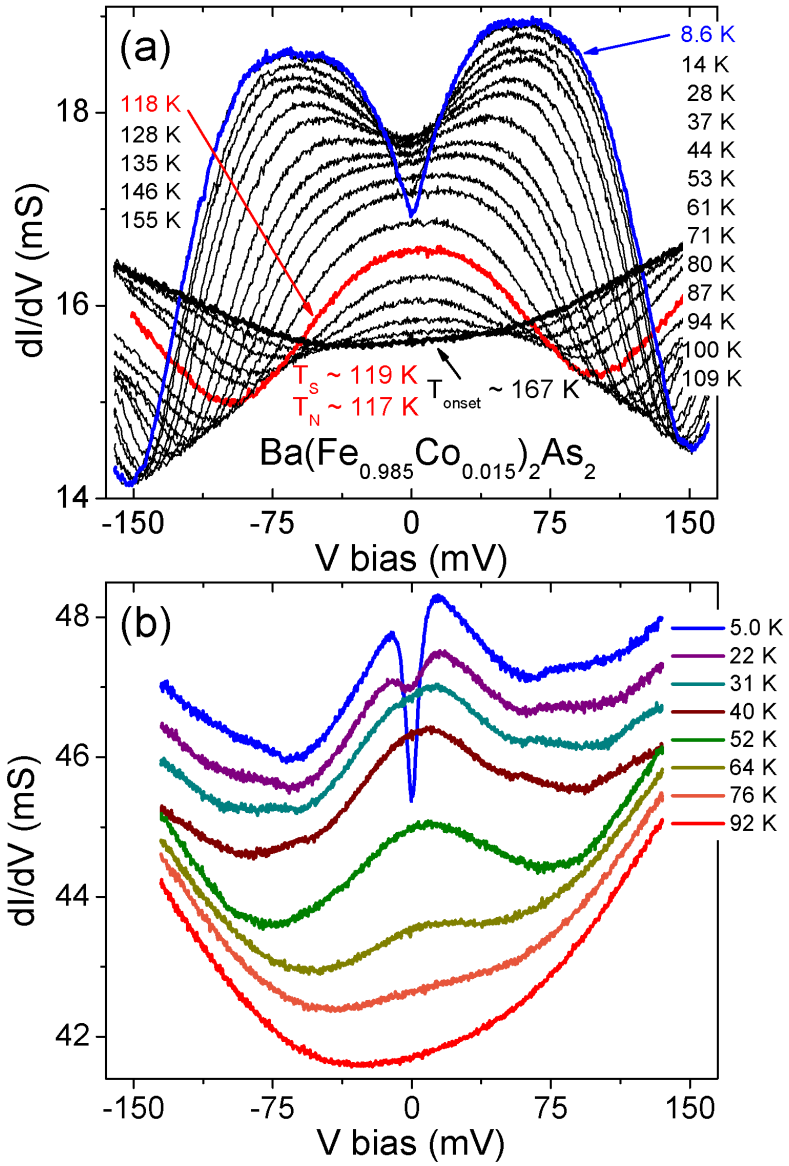

Figure 6.9: dI/dV on $Ba(Fe_{0.985}Co_{0.015})_2As_2$. (a) When the crystal is unstressed, a conductance enhancement is observed in the normal state. The spectra is very similar to what has been seen on $BaFe_2As_2$ [Figure 4.1 (a)]. (b) Once the crystal is placed under compressive stress, the conductance enhancement disappears well before the structural transition temperature. The low temperature conductance peaks also occur at smaller biases, and the voltage range of the conductance enhancement is also smaller.

CHAPTER 7

CONCLUSIONS AND FUTURE WORK RECOMMENDATIONS

This thesis presents our results on utilizing point contact spectroscopy to study the iron based superconductors in their normal and superconducting states.

Transport across a point contact junction on a superconductor is dominated by Andreev reflection, making dI/dV sensitive to the magnitude and symmetry of the superconducting order parameter.

We present Andreev reflection spectra for the 122 and 111 families of the iron based superconductors. The 122 crystals probed include electron doped $Ba(Fe_{1-x}Co_x)_2As_2$ $(x = 0.05, 0.055, 0.07, 0.08)$, hole doped $Ba_{0.8}K_{0.2}Fe_2As_2$, and isoelectronic doped $BaFe_2(As_{1-x}P_x)_2$ $(x = 0.24, 0.43)$. The 111 crystals studied are electron doped $NaFe_{1-x}Co_xAs$ $(x = 0.02, 0.06)$.

The Andreev spectra show clear features corresponding to multiple superconducting gaps. The dI/dV curves are fit to the independent two band BTK model to extract the magnitude of the gaps. Our fits assume isotropic s-wave order parameters. The data do not show any evidence for the existence of a node on the superconducting order parameter.

The excess current due to Andreev reflection is detected above the bulk T_c for underdoped $Ba(Fe_{1-x}Co_x)_2As_2$. We show that this may be caused by inhomogeneous doping effects in the crystals.

Independent band BTK models cannot differentiate between s_{++} and s_{+-} order parameter symmetry. Interfering band models predict different dI/dV

spectra for the two symmetries. However, these differences only become prominent as the junction moves from the transparent regime to the tunneling regime. Future work on these superconductors aims to construct point contact junctions with varying values of Z (the parameter used to describe the junction transparency).

In the second half on the thesis we show that point contact spectroscopy is sensitive to electron correlations in the normal state of the iron based superconductors.

dI/dV for certain iron based superconductors shows a conductance enhancement above the structural transition temperature. The energy dependence of the conductance enhancement follows a log function. The conductance enhancement is only observed at the temperatures and dopings where for detwinned crystals, an in-plane resistive anisotropy exists.

Theoretical work shows that orbital fluctuations above T_S provide extra contributions to the single particle density of states (DOS) at zero energy. The DOS follow a log dependence as the energy is increased. Orbital fluctuations cause a non-Fermi liquid to emerge and give rise to an in-plane resistive anisotropy in the tetragonal state.

Our spectra provides evidence that PCS is sensitive to orbital fluctuations in the iron based superconductors.

Point contact junctions may be impacted by thermal heating effects. The iron based superconductors are reactive in air and the junction area may be oxidized and not representative of the bulk crystal. We discuss in detail the diagnostics we carry out to ensure the quality of our junctions.

dI/dV under applied magnetic field and compressive stress provides a rich line of inquiry to pursue in future studies. Stress changes orbital fluctuations to orbital ordering and suppresses our conductance enhancement. Magnetic

field either induces an asymmetry in the spectra or causes the dI/dV to oscillate around its 0 T value. The relationship between orbital fluctuations and the dI/dV measured by PCS may be further clarified by utilizing these two external factors.

REFERENCES

[1] H. K. Onnes, *Proc. Kon. Akad. Wet. Amsterdam* **14**, 113 (1911).

[2] L. N. Cooper, *Phys. Rev.* **104**, 1189 (1956).

[3] W. Meissner and R. Ochsenfeld, *Naturwissenschaften* **21**, 787 (1933).

[4] J. K. Hulm and R. D. Blaugher, *Phys. Rev.* **123**, 1569 (1961).

[5] F. London and H. London, *Proc. Roy. Soc. (London)* **A149**, 71 (1935).

[6] J. Bardeen, L. N. Cooper, and J. R. Schrieffer, *Phys. Rev.* **108**, 1175 (1957).

[7] I. Giaever, *Phys. Rev. Lett.* **5**, 147 (1960).

[8] S. Doniach, *Physica B* **91**, 231 (1977).

[9] K. Andres, J. E. Graebner, and H. R. Ott, *Phys. Rev. Lett.* **35**, 1779 (1975).

[10] F. Steglich, J. Aarts, C. D. Bredl, W. Lieke, D. Meschede, W. Franz, and H. Schafer, *Phys. Rev. Lett.* **43**, 1892 (1979).

[11] J. G. Bednorz and K. A. Muller, *Z. Phys. B* **64**, 189 (1986).

[12] D. J. V. Harlingen, *Rev. Mod. Phys.* **67**, 515 (1995).

[13] D. J. Scalapino, *Phys. Rep.* **250**, 329 (1995).

[14] T. Timusk and B. Statt, *Rep. Prog. Phys.* **62**, 61 (1999).

[15] Y. Kamihara, T. Watanabe, M. Hirano, and H. Hosono, *J. Am. Chem. Soc.* **130**, 3296 (2008).

[16] D. C. Johnston, *Advances in Physics* **59**, 803 (2010).

[17] M. Rotter, M. Tegel, and D. Johrendt, *Phys. Rev. Lett.* **101**, 107006 (2008).

[18] A. F. Wang, X. G. Luo, Y. J. Yan, J. J. Ying, Z. J. Xiang, G. J. Ye, P. Cheng, Z. Y. Li, W. J. Hu, and X. H. Chen, *Phys. Rev. B* **85**, 224521 (2012).

[19] J. Wen, G. Xu, G. Gu, J. M. Tranquada, and R. J. Birgeneau, *Rep. Prog. Phys.* **74**, 124503 (2011).

[20] J. Paglione and R. L. Greene, *Nature Physics* **6**, 645 (2010).

[21] C. de la Cruz, Q. Huang, J. W. Lynn, J. Y. Li, W. Ratcliff, J. L. Zarestky, H. A. Mook, G. F. Chen, J. L. Juo, N. L. Wang, and P. C. Dai, *Nature* **453**, 899 (2008).

[22] M. Rotter, M. Tegel, D. Johrendt, I. Schellenberg, W. Hermes, and R. Pottgen, *Phys. Rev. B* **78**, 020503 (2008).

[23] C. Fang, H. Yao, W.-F. Tsai, J. P. Hu, and S. A. Kivelson, *Phys. Rev. B* **77**, 224509 (2008).

[24] R. M. Fernandes, E. Abrahams, and J. Schmalian, *Phys. Rev. Lett.* **107**, 217002 (2011).

[25] C.-C. Chen, J. Maciejko, A. P. Sorini, B. Moritz, R. R. P. Singh, and T. P. Devereaux, *Phys. Rev. B* **82**, 100504(R) (2010).

[26] W. Lv, J. Wu, and P. Phillips, *Phys. Rev. B* **80**, 224506 (2009).

[27] W. Lv, F. Kruger, and P. Phillips, *Phys. Rev. B* **82**, 045125 (2010).

[28] C.-C. Lee, W.-G. Yin, and W. Ku, *Phys. Rev. Lett.* **103**, 267001 (2009).

[29] W.-C. Lee, W. Lv, and H. Z. Arham, *Int. J. Mod. Phy. B* **27**, 1330014 (2013).

[30] Z.-A. Ren, W. Lu, J. Yang, W. Yi, X.-L. Shen, Z.-C. Li, G.-C. Che, X.-L. Dong, L.-L. Sun, F. Zhou, and Z.-X. Zhao, *Chin. Phys. Lett.* **25**, 2215 (2008).

[31] D. J. Singh, *Physica C* **469**, 418 (2009).

[32] D. J. Singh and M.-H. Du, *Phys. Rev. Lett.* **100**, 237003 (2008).

[33] D. N. Basov and A. V. Chubukov, *Nature Physics* **7**, 272 (2011).

[34] I. I. Mazin, *Nature* **464**, 183 (2010).

[35] W. L. McMillan and J. M. Rowell, *Phys. Rev. Lett.* **14**, 108 (1965).

[36] W. L. McMillan and J. M. Rowell, *Superconductivity, edited by R. D. Parks (Marcel Dekker, New York, 1969), Vol. 1* .

[37] W. A. Harrison, *Phys. Rev.* **123**, 85 (1961).

[38] I. K. Yanson, *J. Exp. Theor. Phys.* **39**, 506 (1974).

[39] A. V. Khotkevich and I. K. Yanson, *Atlas of Point Contact Spectra of Electron-Phonon Interactions In Metals, (Kluwer Academic, 1995)* .

[40] Y. G. Naidyuk and I. K. Yanson, *Point-Contact Spectroscopy, (New York: Springer 2005)* .

[41] A. F. Andreev, *Sov. Phys. JETP* **19**, 1228 (1964).

[42] W. K. Park, J. L. Sarrao, J. D. Thompson, and L. H. Greene, *Phys. Rev. Lett.* **100**, 177001 (2008).

[43] W. K. Park, P. H. Tobash, F. Ronning, E. D. Bauer, J. L. Sarrao, J. D. Thompson, and L. H. Greene, *Phys. Rev. Lett.* **108**, 246403 (2012).

[44] D. Daghero and R. S. Gonnelli, *Super. Sci. Tech.* **23**, 043001 (2010).

[45] G. Wexler, *Proc. Phys. Soc.* **89**, 927 (1966).

[46] G. E. Blonder, M. Tinkham, and T. M. Klapwijk, *Phys. Rev. B* **25**, 4515 (1982).

[47] A. Plecenik, M. Grajcar, S. Benacka, P. Seidel, and A. Pfuch, *Phys. Rev. B* **49**, 10016 (1994).

[48] R. C. Dynes, J. P. Garno, G. B. Hertel, and T. P. Orlando, *Phys. Rev. Lett.* **53**, 2437 (1984).

[49] Y. Tanaka and S. Kashiwaya, *Phys. Rev. Lett.* **74**, 3451 (1995).

[50] S. Wu and K. V. Samokhin, *Phys. Rev. B* **81**, 214506 (2010).

[51] A. Brinkman, A. A. Golubov, H. Rogalla, O. V. Dolgov, J. Kortus, Y. Kong, O. Jepsen, and O. K. Andersen, *Phys. Rev. B* **65**, 180517(R) (2002).

[52] R. S. Gonnelli, D. Daghero, G. A. Ummarino, V. A. Stepanov, J. Jun, S. M. Kazakov, and J. Karpinski, *Phys. Rev. Lett.* **89**, 247004 (2002).

[53] L. H. Greene, *Oral Presentation at ICMR Summer School on Novel Superconductors* (2009).

[54] W. K. Park and L. H. Greene, *J. Phys.: Cond. Matt.* **21**, 103203 (2009).

[55] X. Lu, *Point-contact Andreev reflection studies on superconductors, Ph.D. dissertation, University of Illinois at Urbana-Champaign* (2010).

[56] R. Holm, *1958 Electric Contacts Handbook (Berlin: Springer)* .

[57] D. Daghero, M. Tortello, G. A. Ummarino, and R. S. Gonnelli, *Rep. Prog. Phys.* **74**, 124509 (2011).

[58] P. Samuely, Z. Pribulova, P. Szabo, G. Pristas, S. L. Budko, and P. C. Canfield, *Physica C* **469**, 507 (2009).

[59] M. Tortello, D. Daghero, G. A. Ummarino, V. A. Stepanov, J. Jiang, J. D. Weiss, E. E. Hellstrom, and R. S. Gonnelli, *Phys. Rev. Lett.* **105**, 237002 (2010).

[60] I. R. Fisher, L. Degiorgi, and Z. X. Shen, *Rep. Prog. Phys.* **74**, 124506 (2011).

[61] H. Z. Arham, C. R. Hunt, J. Gillett, S. D. Das, S. E. Sebastian, D. Y. Chung, M. G. Kanatzidis, and L. H. Greene, *ArXiv:1307.1908* (2013).

[62] S. E. Sebastian, J. Gillett, N. Harrison, P. H. C. Lau, D. J. Singh, C. H. Mielke, and G. G. Lonzarich, *J. Phys.: Cond. Matt.* **20**, 422203 (2008).

[63] J. Gillett, S. D. Das, P. Syers, A. K. T. Ming, J. I. Espeso, C. M. Petrone, and S. E. Sebastian, *arXiv:1005.1330v1* .

[64] N. Ni, M. E. Tillman, J.-Q. Yan, A. Kracher, S. T. Hannahs, S. L. Budko, and P. C. Canfield, *Phys. Rev. B* **78**, 214515 (2008).

[65] H. Z. Arham, C. R. Hunt, W. K. Park, J. Gillett, S. D. Das, S. E. Sebastian, Z. J. Xu, J. S. Wen, Z. W. Lin, Q. Li, G. Gu, A. Thaler, S. Ran, S. L. Bud'ko, P. C. Canfield, D. Y. Chung, M. G. Kanatzidis, and L. H. Greene, *Phys. Rev. B* **85**, 214515 (2012).

[66] M. L. Teague, G. K. Drayna, G. P. Lockhart, P. Cheng, B. Shen, H.-H. Wen, and N.-C. Yeh, *Phys. Rev. Lett.* **106**, 087004 (2011).

[67] K. Terashima, Y. Sekiba, J. H. Bowen, K. Nakayama, T. Kawahara, T. Sato, P. Richard, Y.-M. Xu, L. J. Li, G. H. Cao, Z.-A. Xu, H. Ding, and T. Takahashi, *PNAS* **106**, 7330 (2009).

[68] D. Y. Chung et al., *unpublished* .

[69] S. Avci, O. Chmaissem, E. A. Goremychkin, S. Rosenkranz, J.-P. Castellan, D. Y. Chung, I. S. Todorov, J. A. Schlueter, H. Claus, M. G. Kanatzidis, A. Daoud-Aladine, D. Khalyavin, and R. Osborn, *Phys. Rev. B* **83**, 172503 (2011).

[70] H. Ding, P. Richard, K. Nakayama, K. Sugawara, T. Arakane, Y. Sekiba, A. Takayama, S. Souma, T. Sato, T. Takahashi, Z. Wang, X. Dai, Z. Fang, G. F. Chen, J. L. Luo, and N. L. Wang, *Europhys. Lett.* **83**, 47001 (2008).

[71] A. A. Golubov, A. Brinkman, Y. Tanaka, I. I. Mazin, and O. V. Dolgov, *Phys. Rev. Lett.* **103**, 077003 (2009).

[72] I. B. Sperstad, J. Linder, and A. Sudbo, *Phys. Rev. B* **80**, 144507 (2009).

[73] W. K. Park, C. R. Hunt, H. Z. Arham, Z. J. Xu, J. S. Wen, Z. W. Lin, Q. Li, G. D. Gu, and L. H. Greene, *arXiv:1005.0190* .

[74] G. Sheet, M. Mehta, D. A. Dikin, S. Lee, C. W. Bark, J. Jiang, J. D. Weiss, E. E. Hellstrom, M. S. Rzchowski, C. B. Eom, and V. Chandrasekhar, *Phys. Rev. Lett.* **105**, 167003 (2010).

[75] W.-C. Lee and P. W. Phillips, *Phys. Rev. B* **86**, 245113 (2012).

[76] S. Jiang, H. Xing, G. Xuan, C. Wang, Z. Ren, C. Feng, J. Dai, Z. Xu, and G. Cao, *J. Phys.: Condens. Matter* **21**, 382203 (2009).

[77] M. Yamashita, Y. Senshu, T. Shibauchi, S. Kasahara, K. Hashimoto, D. Watanabe, H. Ikeda, T. Terashima, I. Vekhter, A. B. Vorontsov, and Y. Matsuda, *Phys. Rev. B* **84**, 060507(R) (2011).

[78] K. Hashimoto, M. Yamashita, S. Kasahara, Y. Senshu, N. Nakata, S. Tonegawa, K. Ikada, A. Serafin, A. Carrington, T. Terashima, H. Ikeda, T. Shibauchi, , and Y. Matsuda, *Phys. Rev. B* **81**, 220501(R) (2010).

[79] Y. Nakai, T. Iye, S. Kitagawa, K. Ishida, S. Kasahara, T. Shibauchi, Y. Matsuda, and T. Terashima, *Phys. Rev. B* **81**, 020503(R) (2010).

[80] T. Shimojima, F. Sakaguchi, K. Ishizaka, Y. Ishida, T. Kiss, M. Okawa, T. Togashi, C.-T. Chen, S. Watanabe, M. Arita, K. Shimada, H. Namatame, M. Taniguchi, K. Ohgushi, S. Kasahara, T. Terashima, T. Shibauchi, Y. Matsuda, A. Chainani, and S. Shin, *Science* **332**, 564 (2011).

[81] Y. Zhang, Z. R. Ye, Q. Q. Ge, F. Chen, J. Jiang, M. Xu, B. P. Xie, and D. L. Feng, *Nature Physics* **8**, 371 (2012).

[82] J. G. Analytis, J.-H. Chu, R. D. McDonald, S. C. Riggs, and I. R. Fisher, *Phys. Rev. Lett.* **105**, 207004 (2010).

[83] H.-H. Kuo, J. G. Analytis, J.-H. Chu, R. M. Fernandes, J. Schmalian, and I. R. Fisher, *Phys. Rev. B* **86**, 134507 (2012).

[84] Z.-H. Liu, P. Richard, K. Nakayama, G.-F. Chen, S. Dong, J.-B. He, D.-M. Wang, T.-L. Xia, K. Umezawa, T. Kawahara, S. Souma, T. Sato, T. Takahashi, T. Qian, Y. Huang, N. Xu, Y. Shi, H. Ding, and S.-C. Wang, *Phys. Rev. B* **84**, 064519 (2011).

[85] X. Zhang, N. P. Butch, P. Syers, S. Ziemak, R. L. Greene, and J. Paglione, *Phys. Rev. X* **3**, 011011 (2013).

[86] H. Meekes, *Phys. Rev. B* **38**, 5924 (1988).

[87] R. Escudero and F. Morale, *Solid State Communications* **150**, 715 (2010).

[88] J.-H. Chu, J. G. Analytis, K. D. Greve, P. L. McMahon, Z. Islam, Y. Yamamoto, and I. R. Fisher, *Science* **329**, 824 (2010).

[89] L. W. Harriger, H. Q. Luo, M. S. Liu, C. Frost, J. P. Hu, M. R. Norman, and P. Dai, *Phys. Rev. B* **84**, 054544 (2011).

[90] S. Ran, S. L. Budko, D. K. Pratt, A. Kreyssig, M. G. Kim, M. J. Kramer, D. H. Ryan, W. N. Rowan-Weetaluktuk, Y. Furukawa, B. Roy, A. I. Goldman, and P. C. Canfield, *Phys. Rev. B* **83**, 144517 (2011).

[91] M. A. Tanatar, A. Kreyssig, S. Nandi, N. Ni, S. L. Budko, P. C. Canfield, A. I. Goldman, and R. Prozorov, *Phys. Rev. B* **79**, 180508(R) (2009).

[92] M. A. Tanatar, E. C. Blomberg, A. Kreyssig, M. G. Kim, N. Ni, A. Thaler, S. L. Budko, P. C. Canfield, A. I. Goldman, I. I. Mazin, and R. Prozorov, *Phys. Rev. B* **81**, 184508 (2010).

[93] E. C. Blomberg, M. A. Tanatar, A. Kreyssig, N. Ni, A. Thaler, R. Hu, S. L. Budko, P. C. Canfield, A. I. Goldman, and R. Prozorov, *Phys. Rev. B* **83**, 134505 (2011).

[94] J. J. Ying, X. F. Wang, T. Wu, Z. J. Xiang, R. H. Liu, Y. J. Yan, A. F. Wang, M. Zhang, G. J. Ye, P. Cheng, J. P. Hu, and X. H. Chen, *Phys. Rev. Lett.* **107**, 067001 (2011).

[95] J. Jiang, C. He, Y. Zhang, M. Xu, Q. Q. Ge, Z. R. Ye, F. Chen, B. P. Xie, and D. L. Feng, *ArXiv:1210.0397* (2012).

[96] W.-C. Lee, *unpublished* .

[97] A. G. M. Jansen, A. P. van Gelder, and P. Wyder, *J. Phys. C: Solid State Physics* **13**, 6073 (1980).

[98] L. Chauviere, Y. Gallais, M. Cazayous, M. A. Measson, A. Sacuto, D. Colson, and A. Forget, *Phys. Rev. B* **84**, 104508 (2011).

[99] S. Sugai, Y. Mizuno, R. Watanabe, T. Kawaguchi, K. Takenaka, H. Ikuta, Y. Takayanagi, N. Hayamizu, and Y. Sone, *JPSJ* **81**, 024718 (2012).

[100] M. Nakajima, S. Ishida, K. Kihou, Y. Tomioka, T. Ito, Y. Yoshida, C. H. Lee, H. Kito, A. Iyo, H. Eisaki, K. M. Kojima, and S. Uchida, *Phys. Rev. B* **81**, 104528 (2010).

[101] W. Z. Hu, J. Dong, G. Li, Z. Li, P. Zheng, G. F. Chen, J. L. Luo, and N. L. Wang, *Phys. Rev. Lett.* **101**, 257005 (2008).

[102] P. Richard, K. Nakayama, T. Sato, M. Neupane, Y.-M. Xu, J. H. Bowen, G. F. Chen, J. L. Luo, N. L. Wang, X. Dai, Z. Fang, H. Ding, and T. Takahashi, *Phys. Rev. Lett.* **104**, 137001 (2010).

[103] M. A. Tanatar, N. Ni, A. Thaler, S. L. Budko, P. C. Canfield, and R. Prozorov, *Phys. Rev. B* **82**, 134528 (2010).

[104] M. Yi, D. Lu, J.-H. Chu, J. G. Analytis, A. P. Sorini, A. F. Kemper, B. Moritz, S.-K. Mo, R. G. Moore, M. Hashimoto, W.-S. Lee, Z. Hussain, T. P. Devereaux, I. R. Fisher, and Z.-X. Shen, *PNAS* **108**, 6878 (2011).

[105] A. Dusza, A. Lucarelli, F. Pfuner, J.-H. Chu, I. R. Fisher, and L. Degiorgi, *EPL* **93**, 37002 (2011).

[106] H. Park, K. Haule, and G. Kotliar, *Phys. Rev. Lett.* **107**, 137007 (2011).

[107] S. Kasahara, H. J. Shi, K. Hashimoto, S. Tonegawa, Y. Mizukami, T. Shibauchi, K. Sugimoto, T. Fukuda, T. Terashima, A. H. Nevidomskyy, and Y. Matsuda, *Nature* **486**, 382 (2012).

[108] C.-L. Song, Y.-L. Wang, P. Cheng, Y.-P. Jiang, W. Li, T. Zhang, Z. Li, K. He, L. Wang, J.-F. Jia, H.-H. Hung, C. Wu, X. Ma, X. Chen, and Q.-K. Xue, *Science* **332**, 1410 (2011).

[109] H.-H. Hung, C.-L. Song, X. Chen, X. Ma, Q.-K. Xue, and C. Wu, *Phys. Rev. B* **85**, 104510 (2012).

[110] J. W. W. Lv and and P. Phillips, *Phys. Rev. B* **80**, 224506 (2009).

[111] M. J. Lawler, D. G. Barci, V. Fernndez, E. Fradkin, and L. Oxman, *Phys. Rev. B* **73**, 085101 (2006).

[112] H.-H. Kuo, J. G. Analytis, J.-H. Chu, R. M. Fernandes, J. Schmalian, and I. R. Fisher, *Phys. Rev. B* **86**, 134507 (2012).

[113] I. Todorov, D. Y. Chung, H. Claus, C. D. Malliakas, A. P. Douvalis, T. Bakas, J. He, V. P. Dravid, and M. G. Kanatzidis, *Chem. Mater.* **22**, 3916 (2010).

[114] X. Zhou, P. Cai, A. Wang, W. Ruan, C. Ye, X. Chen, Y. You, Z.-Y. Weng, and Y. Wang, *Phys. Rev. Lett.* **109**, 037002 (2012).

[115] B. L. Altshuler, A. G. Aronov, and P. A. Lee, *Phys. Rev. Lett.* **44**, 1288 (1980).

[116] M. E. Gershenzon, V. N. Gubankov, and M. I. Fale, *Sov. Phys. JETP* **63**, 1287 (1986).

[117] A. F. Wang, X. G. L. J. J. Ying and, Y. J. Yan, D. Y. Liu, Z. J. Xiang, P. Cheng, G. J. Ye, L. J. Zou, Z. Sun, and X. H. Chen, *ArXiv:1207.3852v1* (2012).

[118] C.-L. Song, Y. Yin, M. Zech, T. Williams, M. M. Yee, G.-F. Chen, J.-L. Luo, N.-L. Wang, E. W. Hudson, and J. E. Hoffman, *Phys. Rev. B* **87**, 214519 (2013).

[119] A. M. Duif, A. G. M. Jansen, and P. Wyder, *J. Phys.: Condens. Matter.* **1**, 3157 (1989).

[120] B. Verkin, I. Yanson, I. Kulik, O. Shklyarevski, A. Lysykh, and Y. Naydyuk, *Solid State Communications* **30**, 215 (1979).

[121] T. Y. Chen, C. L. Chien, M. Manno, L. Wang, and C. Leighton, *Phys. Rev. B* **81**, 020301(R) (2010).

[122] A. G. M. Jansen, A. M. Duif, A. A. Lysykh, and P. Wyder, *Narrow Band Phenomena-Influence of Electrons with both Band and Localised Character (NATO Advanced Study Workshop) ed. J. C. Fuggle, G. Sawatzky and J. W. Allen (New York: Plenum)* (1988).

[123] N. Kurita, F. Ronning, C. F. Miclea, E. D. Bauer, J. D. Thompson, A. S. Sefat, M. A. McGuire, B. C. Sales, D. Mandrus, and R. Movshovich, *Phys. Rev. B* **79**, 214439 (2009).

[124] V. V. Fisun, I. K. Yanson, J. M. van Ruitenbeek, and J. A. Mydosh, *Low Temp. Phys.* **28**, 123 (2002).

[125] J.-H. Chu, J. G. Analytis, D. Press, K. D. Greve, T. D. Ladd, Y. Yamamoto, and I. R. Fisher, *Phys. Rev. B* **81**, 214502 (2010).